Fatigue Life Evaluation and Prediction of Inconel 718 Manufactured by Selective Laser Melting

by

K. Heyson

to obtain the degree of Master of Science of Materials Science and Engineering
at the Delft University of Technology,
to be defended publicly on Monday November 30, 2013 at 9:00 AM.

Student number:	4905512	
Project duration:	February 10, 2020 – November 30, 2020	
Thesis committee:	Dr. V. Popovich,	TU Delft, supervisor
	Dr. Y. Gonzalez-Garcia,	TU Delft
	J. L. Galán Argumendo	TU Delft
	Dr. H. Gower	Shell Global Solutions BV.
	Dr. M. Wilms	Shell Global Solutions BV.

This thesis is confidential and cannot be made public until November 30, 2022.

TU Delft

Abstract

The prevalence of additive manufacturing (AM), or 3D printing, has grown in recent decades as a method of manufacturing complex geometries, prototype parts, or high tuned microstructures. One method of additive manufacturing is selective laser melting (SLM), a powder bed fusion technique which utilizes a laser to melt a metal alloy powder layer by layer to form the final geometry. Inconel 718 is a nickel-based superalloy commonly used in high temperature applications due to its superior mechanical and corrosion resistance properties. Owing to a difficult in machining, additive manufacturing has become particularly advantageous method for the production of Inconel 718. The SLM process is associated with a greater degree of process defects as compared to a traditional production method, in particular a poor surface condition, porosity and an anisotropic microstructure. These surface defects pose an issue in response to cyclic loading, as they serve as stress concentrators and can become crack initiation sites. As a result, post-processing treatments are typically required to improve the quality and mechanical properties. This master work focused on two primary aims. First, the characterization of SLM Inconel 718 processed with different layer thicknesses, build directions and post-processing surface treatments and second, the development of a prediction model for fatigue life based on process defects.

Smaller layer thickness was found to result in lower surface roughness, which in turn resulting in fatigue performance as compared to larger thicknesses. Differences in surface quality and properties were identified on samples built at an incline. The plane opposite the build direction (the 'downskin' side) exhibited higher surface roughness and increased near surface hardness. Mechanical polishing of the surface led to a significant improvement in fatigue performance associated with dramatic reduction in surface roughness and near-surface voiding. Electropolishing as a post-processing treatment did not have a significant impact on surface quality or on fatigue performance. Surface defects were identified as the location of fatigue crack initiation. Removal of these defects by post-processing would therefore provide the greatest improvement in the fatigue performance of SLM Inconel 718. The Murakami-Endo method of fatigue life prediction showed promising results in predicting fatigue life of a sample population based on defects, with good agreement to experimental data.

K. Heyson
Delft, November 2020

Acknowledgements

This thesis was carried out with support from Shell Global Solutions BV. I would like to thank Marc Wilms for his support and assistance in putting the project together, in particular his effort to overcome the logistical challenges at the onset. I would also like to thank Heather Gower for her technical insight and thoughtful questions.

I would like to thank my supervisor Vera Popovich for her guidance and assistance throughout the project duration.

I would like to thank Drs. Richard Huizenga and Dhr. Ruud Hendrikx for their assistance and their expertise with X-ray analysis. I would also like to thank Ton Riemslag and Elise Reinton for their assistance with mechanical testing and insightful discussions.

Lastly, I would like to thank my parents, family and friends near and far for their constant encouragement and support.

K. Heyson
Delft, October 2020

Contents

List of Figures

List of Tables

Nomenclature

$2N_f$	Reversals to failure
ΔK_{th}	Threshold stress intensity factor range
v	Scan velocity [mm/s]
$\sqrt{area}$	Square root of the defect area projected onto the plane perpendicular to the applied stress
AM	Additive Manufacturing
$ANOVA$	Analysis of variance
CAD	Computer Aided Design
CT	Computed tomography
FEA	Finite element analysis
h	Hatch distance [mm]
HAZ	Heat affected zone
HCF	High cycle failure
HIP	Hot Isostatic Pressing
HSA	Homogenization and solution aging
P	Laser power [W]
PBF	Powder Bed Fusion
R	Stress ratio
R_a	Arithmatical mean height [μm]
SA	Solution aging
SEM	Scanning electron microscopy
SIF	Stress intensity factor
SLM	Selective Laser Melting
$SMART$	Separating morphing and adaptive re-meshing technology
STC	Subsequent thermal cycling
t	Layer thickness [mm]
VED	Volumetric energy density [J/mm^3]

1 Introduction

1.1. Background

The use of additive manufacturing (AM), also known as 3D printing, for metal alloy components has increased in the past few decades in a variety of industries. The process is commonly applied to prototyping or small scale production, but has also gained ground in the manufacturing of components with complex geometries or finely tuned microstructures. One such additive manufacturing method is selective laser melting (SLM), a powder bed fusion technique in which a laser melts a metal alloy powder layer by layer to build a component from a CAD model. The process comes with associated drawbacks, in particular a poor surface condition characterized by roughness, nodules, or sub-surface voiding that typically requires some sort of post-processing surface treatment. Porosity or larger voids are also a common occurrence in AM components and typically tuning of AM process parameters by trial and error is necessary to create a low defect microstructure with mechanical performance comparable to that of traditionally manufacturing. In comparison to a traditional wrought microstructure, AM components are typified by anisotropy in microstructure and mechanical properties, which may also require post-processing to correct.

The selective laser melting process results in a variable microstructure dependent on process parameters, as well as wide variance in mechanical properties based on that microstructure and on process-induced defects. This property variation presents an challenge for engineers in the design of components able to withstand certain loading conditions. Research in the field of additive manufacturing has consequently focused on minimizing any variation or defect in the microstructure, both through adjustment of process parameters and by post-processing heat or surface treatments. Defects that commonly result from SLM processing, in particular surface roughness and voiding, are a particular problem for cyclic loading conditions. This poor surface condition creates geometrical stress concentrators at which fatigue cracks may more easily initiation and then propagate, leading to failure. The effect of stress concentrators and defects has long been studied in the field of fracture mechanics. Models and predictive methods previously used to study traditionally processed material can be applied to AM components to better understand the effect of the process defects on mechanical performance.

Inconel 718 is a nickel-based superalloy, commonly used in high temperature applications due to superior performance at extreme conditions. It is often used in oil and gas applications due to great mechanical and corrosion resistance properties. Inconel 718 is heavily alloyed and is therefore liable to form undesirable intermetallic phases in certain processing conditions. Considering this and the susceptibility of SLM components to a reduction in fatigue life, the microstructure and resulting mechanical performance must be evaluated before a simple exchange can be made of a traditional processing technique with SLM.

1.2. Thesis Motivation

There is a lack of mechanical test data in the literature, both due to the newness of the technique and the variation in results due to adjustment of process parameters. Because of the dependence of mechanical properties on defects, it is most desirous to develop a model relating mechanical properties with the defect population resulting from a certain process. A full testing program for the fatigue behavior of a certain process can often be costly and time consuming. If a correlation could be made between the surface condition of an SLM processed component and especially if the surface condition could be characterized by non-destructive means, then fatigue performance of a component could be easily and cheaply predicted.

This master work aims comprises two primary research aims. The first is characterization of the microstructure, surface condition and process-related defects resulting from altering process parameters and post-processing treatment. The second is to develop a predictive model relating defects in Inconel 718 produced by SLM to the resulting fatigue life. The research objectives of the work are as follows:

1. To investigate the effect of SLM layer thickness and build direction on surface roughness, microstructure and process defects.
2. To investigate which post-processing treatments result in the greatest improvement of fatigue life, as well as reduction of surface roughness and near-surface porosity
3. To develop a fatigue life predictive model related to defect size, defect location and material properties

This report is divided into 6 chapters. Chapter 2 provides a background of the essential concepts involved, including an overview of additive manufacturing, selective laser melting processing, Inconel 718 alloy, and fatigue behavior and testing. Chapter 3 outlines the materials and the experimental methods used during the study. The results of the characterization experiments are presented in Chapter 4, as well as a discussion of observations and conclusions related to the research objectives. In Chapter 5 the fatigue testing results of the different sample groups are presented and discussed. This chapter also details the method of creating the predictive study related to fatigue life. The results of the initial prediction are presented including the accuracy of the fit to experimental results, followed by methods used to improve the certainty and accuracy using statistical methods and further experimentation. Finally, Chapter 6 summarizes the work of the thesis and presents conclusions, as well as recommendations for further work.

2

Literature Review

2.1. Additive Manufacturing

The processing technique of additive manufacturing was developed in the 1980s primarily as a prototyping technique but has since entered into commercial use in the past 20 years [4]. Additive manufacturing is a broad term referring to a process of building up a component by layers, as opposed to traditional subtractive manufacturing in which a component is milled out of a block of material. The first step is the generation of a 3-D model of the component using computer aided design (CAD) software. The model is then sliced into layers which are programmed into the AM printing machine [27]. The additive manufacturing process serves not only as an alternative to traditional manufacturing techniques, but also as a method by which to enhance certain properties. The competitive advantages of additive manufacturing include increased freedom in design geometries, ability to produce individual or custom parts, and material flexibility [28]. The use of additive manufacturing also greater reduces the processing time required for custom components or prototypes; although in general processing time is increased for mass production parts. From a financial perspective, additive manufacturing is an attractive option for firms as it reduces material waste and provides a much less costly method to produce small batches of parts, as opposed to designing a producing a mold or creating expensive tooling [27, 29].

There are multiple commercially available methods of metal additive manufacturing. An AM system is typically distinguished by the energy source, such as a laser or an electron beam, and the feed stock. Systems may also be categorized by build volume. There are three general categories of metal additive manufacturing: powder bed, powder feed, and wire feed systems [1]. Powder bed fusion (PBF) techniques such as selective laser melting are commonly used in the industrial space. Additive manufacturing is commonly used for rapid prototyping, tooling, customized components and complex designs. The aerospace industry makes use of the ability to create complex geometries to make lightweight and more fuel-efficient turbines and fuel nozzles. In the medical industry, the customization allows for the creation of individually designed biomedical implants, as well as the creation of porous implants that better mimic bone [27].

2.1.1. Selective Laser Melting

Principles

Selective laser melting (SLM) is a powder bed fusion technique developed in Germany in the 1990s. The advantage of SLM compared to existing techniques was the ability to produce dense metallic components that did not require heat treatment post-processing [27]. The first commercial SLM machine was developed in 1999 for use with iron-based powders [30]. SLM has since gained widespread commercial use due to its versatility and capability to produce geometrically complex components with mechanical properties comparable to or greater than those of bulk materials [28]. SLM uses a laser as the energy source and fine metal powder as the substrate. Figure 2.1 shows a simplistic depiction of the process. The metal powder is kept in the powder delivery system container at the side of the stage. A roller moves a small amount of the powder over to the stage in an even layer. The laser scans the surface of the powder according to the inputted CAD model. The metal melts at the points scanned by

the laser and fuse to the substrate beneath them. The stage is then lowered by a layer thickness, new powder is raked over and the process is repeated until the three-dimensional component is finished [1]. The component can then be removed from the bed and the excess powder retained and reused. The thickness of each layer varies in the range of approximately 40-80 micrometers, depending on the machine and the selected process parameters [30]. Thinner layers naturally lead to longer process times, but provide higher feature resolution. The entire process takes place in a chamber with an inert atmosphere, such as argon. The removal of oxygen from the atmosphere during the process is key to prevent oxidation of the layers as they are produced, which would lead to defects or poor bonding of the layers.

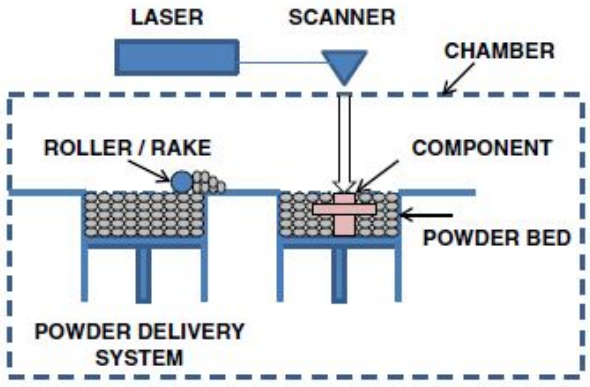

Figure 2.1: Simplified diagram of SLM process [1]

A key advantage of a powder bed process, as opposed to powder feed or wire feed systems, is the ability to create complex features with high resolution and dimensional accuracy [1]. One negative is the amount of post-processing that is often necessary, in order to remove support structures and achieve an acceptable surface quality [27]. Additive manufacturing by SLM is not a simple replacement for traditional methods. The SLM process has the potential to introduce a variety of defects, particularly on the surface of the component, which may require further treatments to address. The SLM process also has the potential to generate unwanted residual stresses or porosity, induce distortion, or result in dimensional inaccuracy - all of which could negatively impact the mechanical or chemical properties of the component [31].

2.1.2. Process Parameters

The settings applied during the SLM process have a significant influence on the resulting product and its chemical and mechanical performance. Figure 2.2 lists some of these common process variables. Inappropriate process parameter selection can lead to the formation of defects previously mentioned, such as porosity, internal stress or surface roughness - all of which can negatively impact the performance of the component. The combination of process parameters essentially determines the thermal cycle experienced by the material and therefore the resulting microstructure, which then greatly influences mechanical and chemical properties. The process parameters required to produce a dense and low defect component vary depending on the alloy powder mix, as the resulting thermal cycle is very dependent on the interaction between the laser and the metal. A successful process requires the powder to fully heat and melt, which is heavily determined by the heat capacity and mass of the metal powder [3].

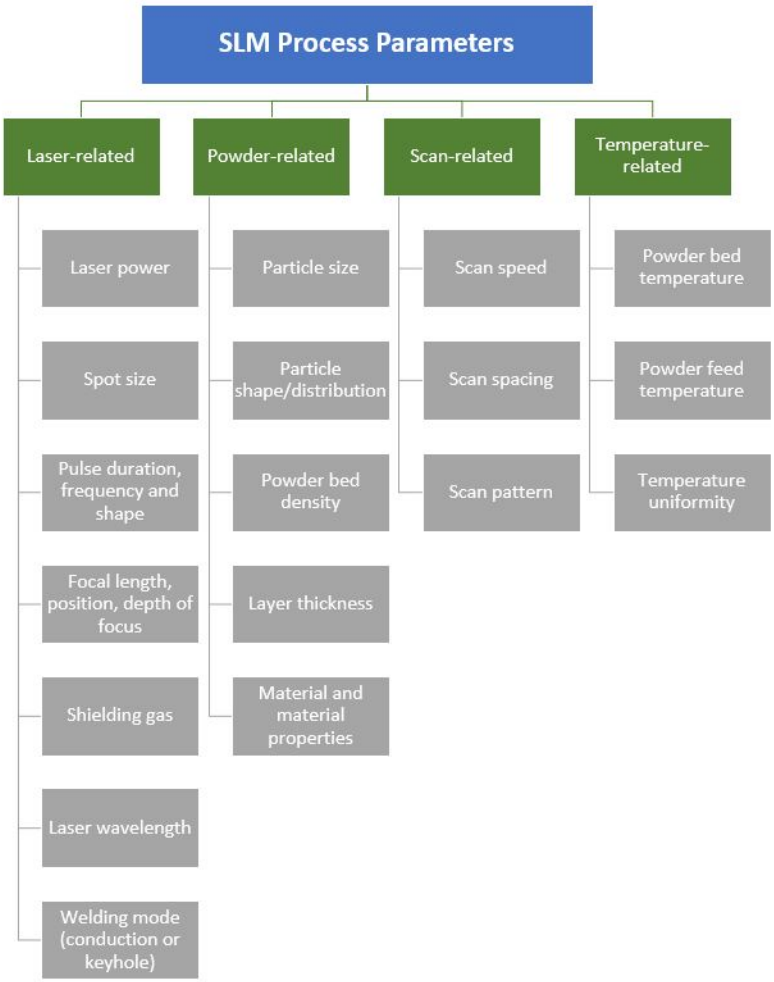

Figure 2.2: Categorization of SLM process parameters (adapted from [2])

Laser Related

The key laser related process parameter is the laser power, which is expressed in Watts. The laser power used for Inconel 718 production in the literature is in the range of 100-200W. The power of the incident laser on the powder surface in part determines the energy density available at the surface to melt the powder. A laser power which is too low could result in unmelted powder particles and incomplete fusion of the layers. Too high laser power can lead to spattering of the molten metal. The beam size is simply the diameter of the incident laser beam on the powder bed and is typically expressed in mm. Increasing the beam diameter increases the size and depth of the melt pool, provided that energy density remains the same [32].

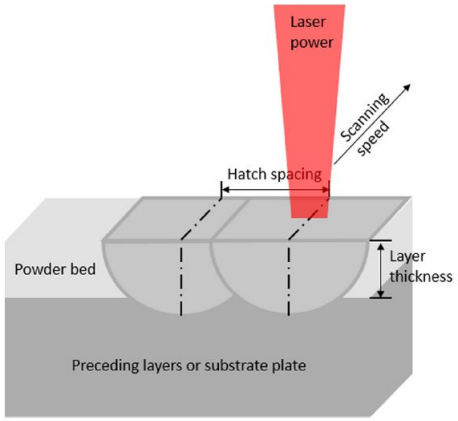

Figure 2.3: Diagram of SLM process parameters [3]

Scan-related

The scan velocity is another term for scan rate or speed and refers to the rate at which the laser passes across the surface. It is expressed in mm/s. For Inconel 718 the scan velocity ranges widely from as low as 80 mm/s to 1200 mm/s. Lowering the scan rate leads to a greater amount of energy from the laser transferred to the powder surface. This could result in heating or remelting of the previously created solid layers underneath the new melt pool, which has consequences in terms of microstructure and boundaries between the layers. A decreased scan velocity also naturally increases the process time and decreases the throughput of the production process. For this reason, it is advantageous for manufacturers to select a fast scan velocity that is slow enough to produce a dense and low defect product.

Other scan-related process parameters include the scan spacing, commonly called the hatch spacing. This is the distance between subsequent lines of the scan as the laser rasters across the powder bed surface. This parameter can be seen in Figure 2.3. Yadriotsov et al. proposed a general rule for the generation of a smooth surface for all metal alloys: maintaining the hatch difference at a value not more than the average width of the track [33].

The scanning strategy, or scan pattern, also plays a significant role in the temperature gradient and resulting microstructure of the SLM layer. In an analysis of the effect of scan patterns on microstructure, Kruth et al. found that certain scan patterns can minimize thermal deformations, as well as limit balling [4]. Figure 2.4 shows the various scan patterns studied. Sector-wise scanning (scanning in not solely x- or y-direction) resulted in the least amount of deformation due to thermal gradients.

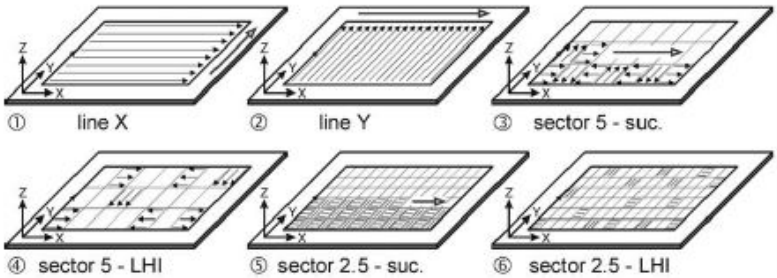

Figure 2.4: Scan pattern examples [4]

Powder-related

The properties of the powder itself are of high importance to the resulting SLM product, as they determine the interaction with the laser. Properties of the powder include the size, shape and distribution of metal particles. Figure 2.5 shows an example of the size distribution of Inconel 718 powder, as well as the powder particle microstructure before SLM processing. These properties are typically determined by the manufacturer of the alloy powder.

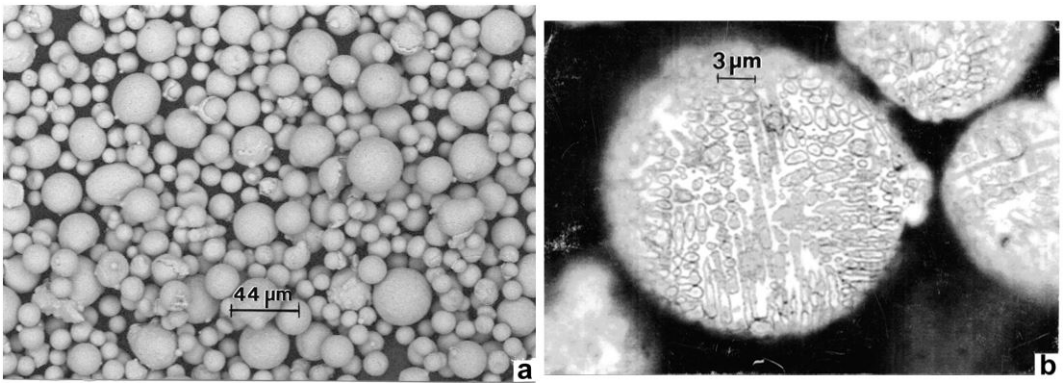

Figure 2.5: SEM image of Inconel 718 precurser powder for SLM (top) and optical micrograph of polished and etched particle cross section with microdendritic microstructure (bottom) [5]

Layer thickness refers to the thickness of the powder layer leveled onto the powder bed by the powder delivery system. The layer thickness of Inconel 718 in the literature ranges from 30-75 µm. The layer thickness influences the energy transferred to the powder per unit volume. Layers too thick, combined with insufficient laser power, could result in unmelted powder between the layers. This could cause voiding or delamination.

Temperature-related

The temperature of the powder bed, the temperature of the powder in the feeder tank and the uniformity of the temperature distribution in both can all play a role in the resulting component microstructure, properties and quality. The resulting properties of the AM component are heavily dependent on the temperature gradient of the melt pool. This gradient is altered by changes in the temperature of the powder or chamber before the laser hits it. These aspects and their effects on resulting properties as pertaining to AM specifically have not been widely studied and temperature related parameters will also not be a focus of this report.

Energy Density

In discussions of the relation of process parameters to measures of build quality such as porosity or surface roughness, it is common to refer to the volumetric energy density (VED), measured in J/mm^3. This value represents the average energy applied during the process per volume of material and is calculated using the laser power (P) in Watts, scan velocity (v) in mm/s, hatch distance (h) in mm and layer thickness (t) in mm [34].

$$E = P/vth \tag{2.1}$$

The volumetric energy density is not a perfect representation of the per volume amount of energy transferred to the material, as the effective volume energy would be reduced by absorptive and reflective properties of the powder itself. The equation also does not account for factors such as the energy transferred by the sintering of subsequent layers, the hatch style, the beam size, gas flow direction, or the laser offset [34, 35].

Prashanth et al. studied the effectiveness of varying solely the energy density to determine optimal parameters for minimizing process defects in $Al_{12}Si$ SLM material. This was done by producing samples with identical energy density but varying combinations of laser power and scan velocity. The resulting samples displayed unequal tensile properties and rather a dependence of properties on laser power. Laser power was therefore reasoned to be the most influential process parameter on SLM properties, while energy density remains useful as a rough estimate of energy transferred to the powder bed for use in comparative purposes [35].

2.1.3. Process Induced Defects

Surface Roughness

A relatively high surface roughness is expected of SLM manufactured metallic components. Surface roughness values can vary substantially depending on the process parameters selected and have been reported in the range of 9 to 20 µm [36]. Reasons for high surface roughness include the discontinuous nature of the process, partially melted powder particles formed at the laser and powder bed interface, spattering of molten metal from the melt pool, or the SLM melt pattern.

Roughness can vary greatly depending on process parameters. Koutiri et al. found lower scan velocities to result in increased surface roughness (R_a)in SLM Inconel 625 for certain beam diameters [6]. At 400W laser power and 160 mm beam diameter, a scan speed of 2 m/s resulted in an S_a of 15.2 µm, while a speed of 1 m/s resulted in S_a of 21 µm. Roughness also depends on the geometry of the additive manufactured component. Large building angles result in a significant increase in surface roughness, due to a stair-step effect caused by the layering process, as illustrated in Figure 2.7. A roughness variation can even exist between the top and the bottom of the angled surface of only 10 degrees, owing to temperature variation. As one of the key advantages of additive manufacturing is the ability to generate complex geometries, it is desirous to reduce this stair-step effect to achieve acceptable surface quality. The effect has been found to increase with increasing building angle and decrease with decreasing layer thickness [12]. Figure 2.6 demonstrates the effect of laser power and roughness. The authors conclude that a higher laser power results in a decrease in surface roughness; however, this is not necessarily the case for extreme building angles. At 35°the lowest roughness is found in the middle of the range (140W). This dependence on laser power was attributed to an increased layer re-melting and smoothing effect associated with higher laser power, while very high laser power results in a larger melt pool and greater incidence of powder particle sticking to the overhang.

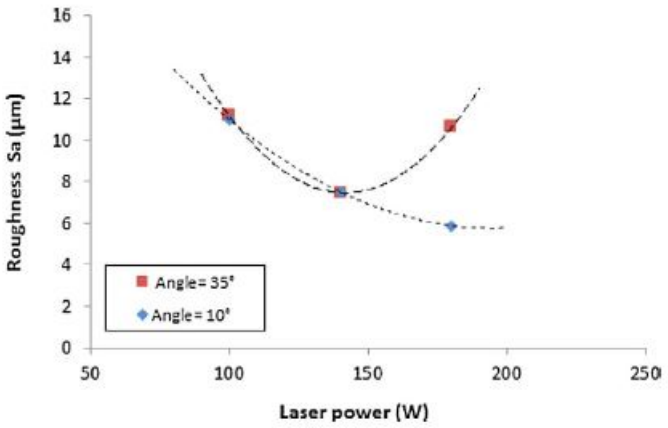

Figure 2.6: Relationship between laser power and upper surface roughness for two different building angles, at a constant scan speed of 0.5 m/s [6]

Process parameter optimization is often focused on the improvement of surface quality and therefore the reduction of surface roughness. A rough surface can have significant detrimental effects on fatigue life, as the surface imperfections result in concentrations of stress which can initiate fatigue cracks. Surface roughness also has a negative impact on corrosion resistance due to the potential for pitting. Depending on the application, post-processing treatments are often applied in order to achieve the required surface condition.

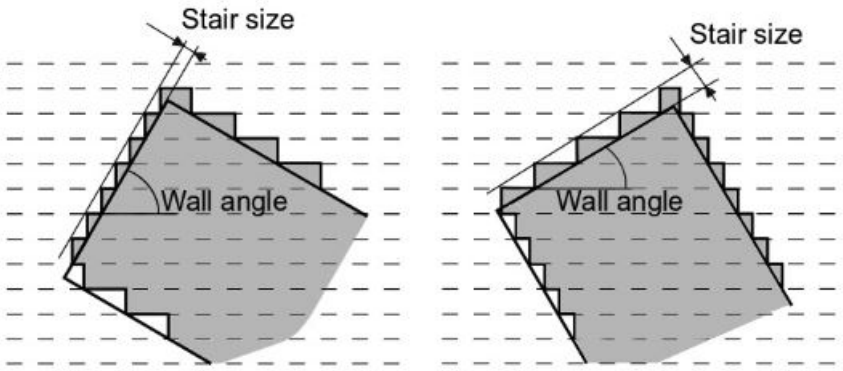

Figure 2.7: Representation of surface roughness differences based on build angle [7]

Porosity

Similarly to surface roughness, porosity poses a particular issue with SLM components which experience cyclical loading. Pores, particularly those located on the surface or sub-surface of the component, may serve as crack initiation sites for fatigue cracks or provide an easier pathway for fatigue cracks to propagate. Porosity also has an impact on the chemical performance of the product. A porous microstructure means more surface area and exposure to corrosion. Pores at the surface of a metal can prevent the flow of solution and create a localized aggressive environment, leading to pitting or increased corrosion.

There are several potential sources of porosity in an SLM metal. One is the entrapment of gas, typically hydrogen, in the melt pool. This creates small pores that are spherical in shape [37]. A second form of porosity is from the incomplete melting of powder characterized by comparatively large, irregularly shaped pores or voids. This voiding often leads to binding defects between the layers and may be caused by balling. Figure 2.8 shows these types of voids occurring in SLM 316.

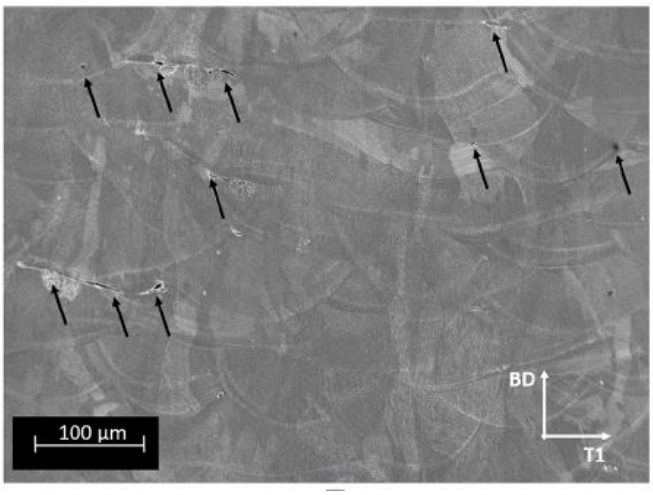

Figure 2.8: Voiding at layer boundaries of SLM 316L (BD = build direction) [8]

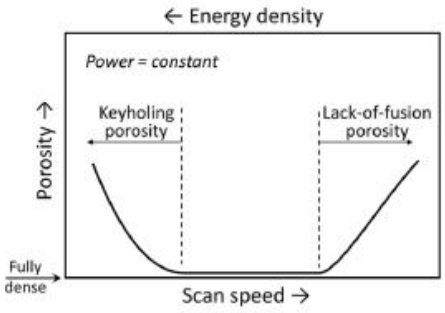

Figure 2.9: Porosity trends with respect to scan speed and energy density [9]

Porosity in the resulting structure can be tuned by adjusting the process parameters. Sun et al. found a relation between scan velocity and volume percent porosity at a laser power of 150W [31]. In general, porosity increased with greater scan velocity. It is thought that a higher scan velocity results in an energy density too low to remelt the previous layer and an increase in solidification rate , leading to incomplete fusion between layers. This relationship is illustrated in Figure 2.9. Sun et al. found a minimum porosity by volume of 1.7% to occur at a scan velocity of 150 mm/s.

Balling

At certain process conditions, molten material generated by the laser can fail to wet with the surrounding material and, because of surface tension, form a ball of metal on the surface [31]. Varying degrees of balling can be seen in Figure 2.10. The balling phenomena is a contributor to porosity in SLM components. Scanning electron microscopy (SEM) investigations of porosity in SLM components found many pores to be the result of voids between discontinuous metal balls. Balling is also known to potentially increase surface roughness [10] and therefore create the need for post-processing treatments, increasing processing complexity and expense as well as potentially inducing dimensional inaccuracies.

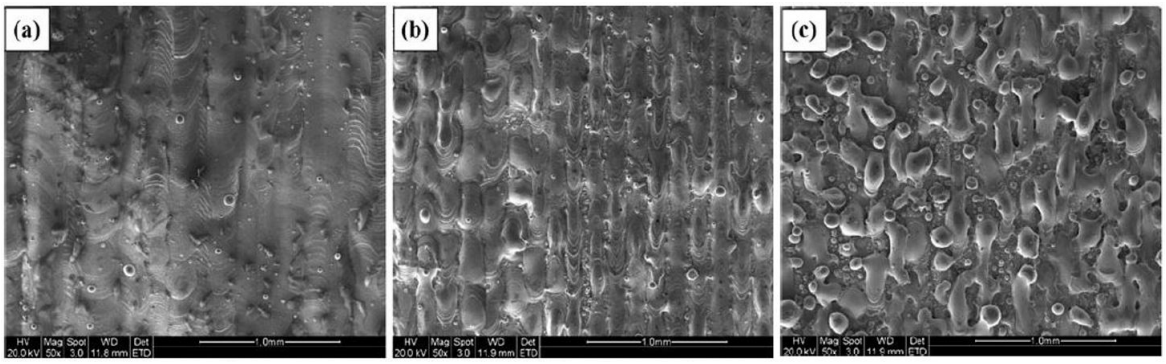

Figure 2.10: SEM images showing balling behavior of SLM 316L at different scan speeds: (a) 50 mm/s, (b) 400 mm/s, (c) 600 mm/s [10]

Balling has been attributed to decreasing laser power in studies in which energy density has been kept constant but laser power varied [35]. Li et al. found a combination of low scan velocity and high laser power (high VED) led to the best wetting and therefore the greatest reduction in balling in stainless steel [10]. The dependency of balling on scan speed is demonstrated in Figure 2.10, with balling increasing in severity at the high scan speeds of 600 mm/s.

Residual Stresses

The high temperature gradient created during the additive manufacturing process results in residual stresses in the metallic component. These stress particularly occur between the base plate and the component, due to the temperature difference. Residual stresses are undesired and should be controlled during the process or eliminated in the post-process, as they have the potential to lead to crack formation upon solidification or in use.

Although high levels of residual stress may be created by the initial laser melt, these stresses may be somewhat relieved as additional layers of metal are built up on top. This is due to a process called subsequent thermal cycling (STC), in which an already solidified layer receives some heat from the energy inputted in the new melt. This new thermal input may serve as an annealing step, in which some stresses are relieved and grain growth may occur. However, the shrinkage of additional layers during solidification may induce tensile stresses in the layers below [11]. These phenomena, combined with the extreme temperature gradient induced by the SLM process, create a complex stress state in the metal.

Figure 2.11 shows the typical temperature gradient in an SLM component in terms of distance from the surface. T_m and T_p represent the melting and plastic temperatures of the metal. Zone I represents

the melted zone of the metal, II the heat affected zone (HAZ) and III the non-affected zone. During heating, zone I is above the plastic temperature and has no residual stress. Zone II is between the ambient temperature (t_n) and below T_p, causing the material to expand. This expansion is restricted by zone III, which does not expand, therefore inducing tensile stresses in zone III and compressive stresses in zone II. Upon cooling, the temperature in zone I falls below T_p and the material is in an incomplete plastic state, leading to tensile residual stress in zone I and increased compressive stress in zone II. As the temperature in zone I continues to drop, the tensile stress increases and the compressive stress in II also increases, extending into zone III [11]. The overall effect of all the layers is that residual tensile stress remains at the top of an SLM part and compressive stress at the bottom of the SLM part.

It is possible to reduce, but not eliminate, the residual stress in an SLM component through tuning of process parameters. Lowering the heat input, which can be achieved by lowering laser power and/or increasing scan speed, as well as reducing the line length has been found to result in smaller residual stresses [11]. It has been found that the ends of the SLM component contain the peak amount of residual stress, which can lead to warpage or cracking. To avoid this, strong support structures need to be implemented in the CAD model and built up during manufacturing [11]. The geometry of the component being built will also impact the resulting residual stresses, as different locations will experience differing temperature gradients and subsequent thermal cycles.

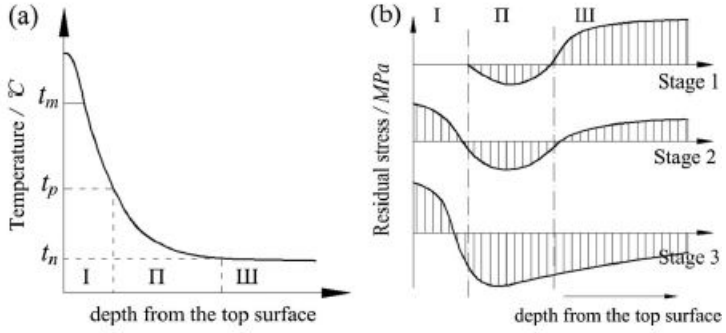

Figure 2.11: (a) Temperature and (b) residual stress distribution in an SLM part [11]

2.1.4. Post-Processing Heat Treatments

Stress Relief Heat Treatment

As described above, the selective laser melting process results in a highly stressed microstructure. For this reason, a post-processing heat treatment is typically performed following production to reduce residual stress in the component, which can lead to warping. It is analogous to an annealing treatment performed after welding. Bringing the component to an elevated temperature allows for faster diffusion of the atoms.

Laser Remelting

Laser remelting is the process of passing the laser over the solidified metal layer to melt it a second time. This can be done for each layer before new powder is added or at the end of the build to the outer surfaces only (laser surface re-melting). As with the other post-processing techniques, laser remelting is performed to improve the surface quality of the SLM component, as well as to reduce residual porosity. The process has also been found to reduce residual stress in the final layer by 55%, when using 150% of the energy used in forming [12].

Yasa et al. studied the reduction in surface roughness of 316L stainless steel produced by SLM following laser remelting at the surface. The average roughness (R_a) decreased to 1.5 µm from 12 µm. This improvement in surface conditions can be seen in the cross-section in Figure 2.12, as well as the reduction in porosity in the remelted layer. The authors achieved a porosity of 0.036%, compared to 0.77% in the as-built condition, by performing laser remelting on every layer [12].

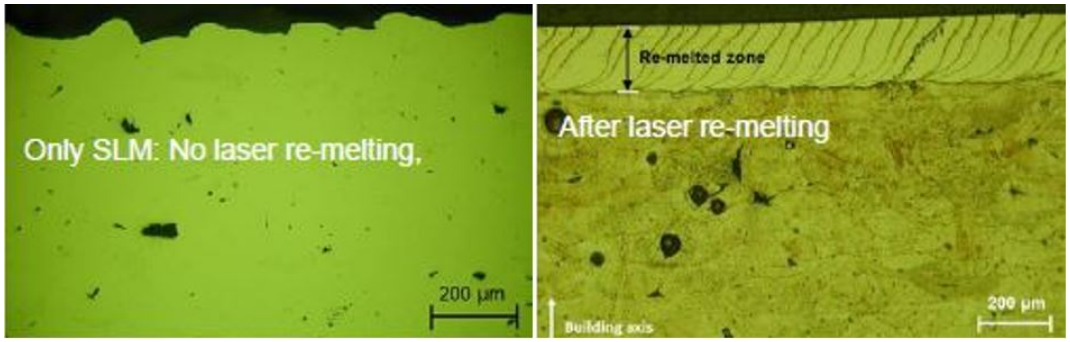

Figure 2.12: Surface porosity and roughness reduction at the surface following one pass of laser remelting [12]

Laser remelting is a promising technique for the improvement of the fatigue life of components manufactured by SLM. The improvement on surface quality, reduction of surface porosity and reduction of surface residual stress all serve to inhibit crack initiation. Drawbacks of laser remelting include added processing time, which naturally will greatly increase processing cost, and in the case of surface remelting, the difficulty or impossibility of processing surfaces of complex geometries.

Hot Isostatic Pressing

Hot isostatic pressing (HIP) is often performed as a post-processing treatment on additive manufactured components, with the goal of reducing porosity and reduce anisotropy in the microstructure. The process is performed in a furnace at high pressure (100-200 MPa) and at high temperatures in an inert atmosphere. The gas exerts hydrostatic pressure uniformly on the component leading to densification [38]. The temperature used is typically 80% of the solidus temperature [39]. HIP has no effect on the surface condition, therefore HIP performed on SLM components for fatigue applications is typically followed up by machining or polishing.

2.1.5. Post-Processing Surface Treatment

Machining

Machining is a post-processing treatment aimed at improving the surface condition of the component. Machining decreases the surface roughness and removes other surface imperfections that may serve as crack initiation sites. Machining serves a secondary purpose of introducing compressive stresses on the surface. This both increases the microhardness of the service and aids in improving the fatigue life of the component due to crack closure effects.

Shot-peening

The technique of shot-peening has been widely used in traditional manufacturing to increase the surface strength of the component. It is a form of cold working in which steel or ceramic shot is fired at the surface, slightly deforming the surface and introducing compressive stresses at the surface. In both conventional and additive manufactured components, shot-peening is performed to improve the fatigue life of the part and reduce the risk for stress corrosion cracking. The procedure also serves reduce or remove surface imperfections that may be stress concentrators. This also leads to an improvement of fatigue life. A disadvantage of shot-peening is that it may increase the overall surface roughness. Although large features may be smoothed down, the process creates a dimpled surface that may be rougher than that of the as-produced alloy [40].

Shot-peening creates a surface hardening profile from the surface, due to the increase in dislocation density due to the deformation. Uzan et al found this hardening effect to be present 50 µm into the interior of $AlSi_{10}Mg$ manufactured by SLM [40].

Chemical Etching

The complex geometries that are possible through additive manufacturing process lead to difficulties in post-processing. Highly intricate or porous structures exhibit the same issues with surface roughness and stress concentrators, but cannot be easily machined. In these cases, chemical etching can be used to improve the surface condition. The resulting change in surface condition can be seen in Figure 2.13, where partially melted powders at the surface are clearly seen to be removed by the chemical etching process. The process does result in some mass loss, which needs to be accounted for in the design stage.

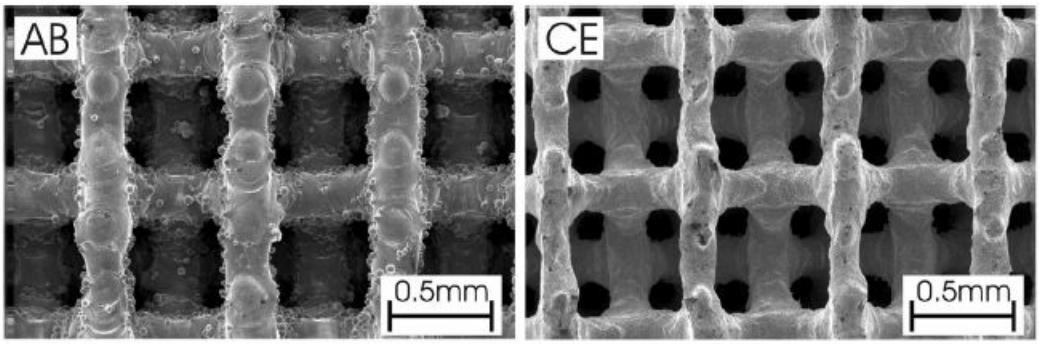

Figure 2.13: Surface condition of porous SLM Ti6Al4V as-built and following chemical etching [13]

Chemical etching is commonly performed in combination with HIP to achieve high densification as well as an improved surface condition. Van Hooreweder et al. evaluated the effect of HIP and chemical etching on the fatigue behavior of porous Ti_6Al_4V. Fatigue testing was performed at a load ratio of R=0.1 and frequency of 15 Hz. The samples which experienced a combination of chemical etching and HIP resulted a significant improvement in fatigue life as compared to as-built, stress relief heat treated and HIP only samples. This effect was most pronounced in the high cycle regime [13].

Electropolishing

Electropolishing is an electrochemical method of controlled dissolution of material from the surface in an electrolyte. Various solutions can be used as the electrolyte; including acids, solvents or ionic liquids. The procedure involves the creation of an electrochemical cell with the SLM alloy as the anode. The amount of material dissolved from the surface of the alloy is proportional to the current put through the cell, according to Faraday's law. The resulting surface quality is affected by the source potential voltage, electropolish duration, current density, electrolyte concentration, etc [41]. As with chemical etching, electropolishing can be successful with surface improvement of complex geometries.

2.2. Inconel 718

Inconel is the term for a family of austenite nickel-chromium alloys, which are refered to as 'superalloys' due to their ability to maintain mechanical strength at elevated temperatures ranging from 450 to 700 °C. Inconel 718 is one alloy in that family containing high amounts of niobium and molybdenum. The alloy is designed for high corrosion and oxidation resistance, strength, creep resistance and excellent weldability, as well as superior performance at high and cryogenic temperature [14]. Due to these qualities, Inconel 718 is an alloy of choice for applications which require resistance to high temperature and extreme mechanical loads, such as aircraft turbines, nuclear reactor vessels, pumps and many more. It is also typically chosen for applications in which resistance to creep is of high importance.

The high hardness of 718 has a negative impact on its machinability and therefore poses an processing issue. Partially for this reason, as well as the other advantages of additive manufacturing enumerated in Section 2.1.1, additive manufacturing has emerged as preferable method for the production of components from 718.

2.2.1. Microstructure

Alloy Composition

Table 2.1 displays the chemical composition of Inconel 718. The base elements are Fe, Ni and Cr with a number of alloying elements designed for the precipitation of strengthening phases.

Table 2.1: Chemical composition of Inconel 718 [14]

Element	C	Cr	Ni	Mo	Mn	Si	P	S	Al	Co
wt %	0.08 max	17.0 - 21.0	50.0 - 55.0	2.8 - 3.3	0.35 max	0.35 max	0.015 max	0.015 max	0.2 - 0.8	1.0 max
	Nb	Ti	Cu	B	Fe					
	4.75 - 5.5	0.65 - 1.15	0.3 max	0.006 max	Balance					

Phases

The microstructure of Inconel 718 is primarily composed of an fcc γ phase matrix with coherent γ' (Ni_3Nb) and γ" ($Ni_3(Al,Ti)$) strengthening phases.

A series of heat treatments is typically performed on both SLM and wrought Inconel 718 to improve strength and other mechanical properties, which are highly dependent on resulting phase formation. Some secondary phases are desirable for strength, while others have detrimental effects and the formation of them is suppressed. Nb tends to segregate and form NbC carbides, Laves phases, or δphases (Ni_3Nb with a needle-like morphology). The Laves phase is a brittle intermetallic with $MgZn_2$ lattice type rich in Si, Nb, and Mo. Laves generally has the form $(Ni,Fe,Cr)_2(Nb,Mo,Ti)$ and the formation of it leads to a reduction in ductility and in fatigue and creep resistance [42]. NbC formation is also detrimental as a stress concentrator and by potentially weakening grain boundaries. The formation of all three of these phases also removes critical Nb, Mo, or Ti from the matrix and therefore reduces the strengthening benefit provided by γ' and γ". Figure 2.14 shows the variety of phases and their relative size and location, typically.

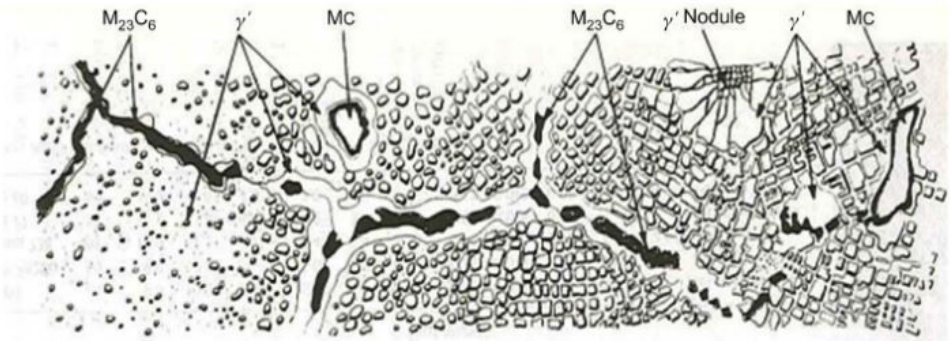

Figure 2.14: Microstructure of superalloys [14]

2.2.2. Processing

Conventional Manufacturing

Traditional processing of Inconel 718 involves a casting process, in which the alloy is made molten through vacuum induction melting or other similar process. In general Inconel 718 processing is performed preferably under vacuum or in an inert environment to minimize oxidation. The molten material is then cast into bars. The resulting cast microstructure is characterized by dendrites formed during solidification, which involves alloying element segregation [15].

Inconel 718 can also be cast into more complex geometries, which is done by remelting the cast bar and pouring into a mold. The resulting microstructure (grain size, morphology, phase structure) is determined by the melt pool during casting, including the temperature gradient at the solid liquid interface and the cooling rate. After casting, post processing solution aging (SA) or homogenization and solution aging (HSA) heat treatments are typically performed, which further impact the resulting microstructure and mechanical properties.

SLM Inconel 718

SLM produces a distinct microstructure that is unlike that of casting and more akin that of a weld. During the production, the SLM part is exposed to severe temperature gradients and large undercooling, which drive non-equilibrium solidification [8]. During casting, the molten material experiences a slow cooling rate of 0.5 K/s, as opposed to the 10^3 to 10^8 K/s rates possible during SLM manufacturing [29]. Individual melt pools can be seen in a cross-section, as shown in Figure 2.15. Within the melt pool the grains formed are columnar and mostly parallel to the build direction. This grain structure within the melt pool is also referred to as dendritic and, at a smaller scale, cellular in nature. The columnar or dendritic grains are mostly aligned with the build direction, but the alignment changes based on position in the melt pool due to convection flow [43]. These columnar grains can be seen in multiple orientations in Figure 2.16. Many of the grains within one melt pool share a boundary with the melt pool, which suggests that grains nucleate heterogeneously at the boundary and grow epitaxially in the direction of the highest temperature gradient [8].

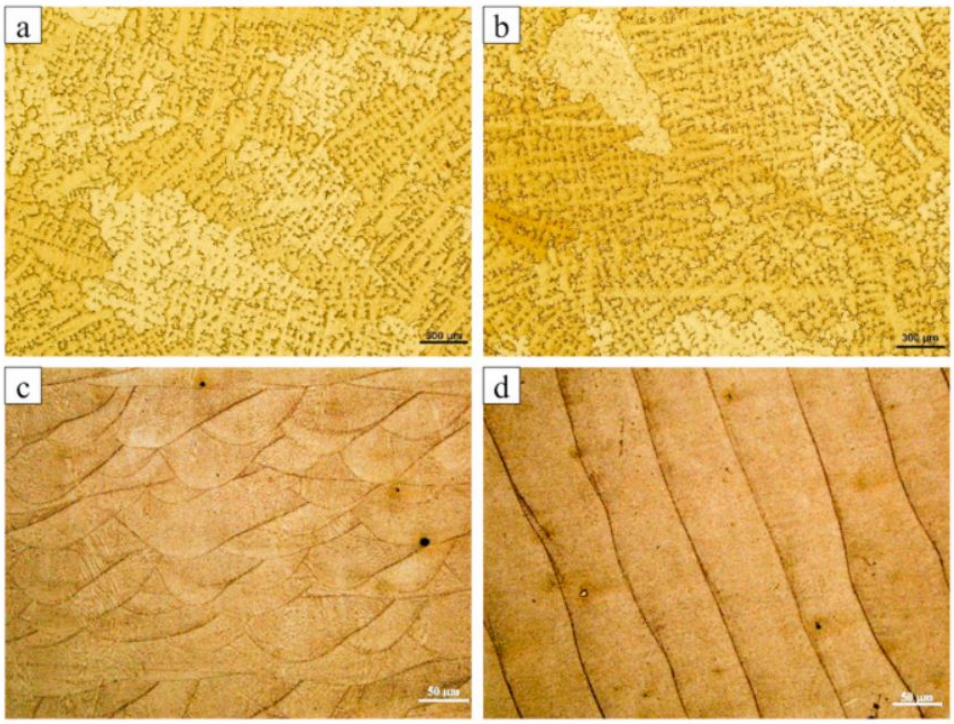

Figure 2.15: Optical micrographs showing microstructure of cast Inconel 718 in (a) transverse and (b) vertical directions and of SLM processed 718 (c) parallel and (d) normal to build direction [15]

The microstructure is naturally heavily dependent on process parameters selected. Very fast scan speeds of 1000 mm/s have been found to create irregularly shaped melt pools, as well as generating a greater amount of defects at the layer interface. Spherical nano-inclusions and high dislocation density have been observed at the melt pool boundaries and have been found to vary with scanning speeds. These inclusions are believed to be the result of alloying element segregation during solidification of the supercooled liquid [43].

The layering process of SLM has implications for the microstructure of the solidified layers being built upon. The additional heat supplied by the formation of a new layer causes partial remelting. The remelted material, once solidified, maintains the same crystallographic orientation as the neighboring grains [8]. These repeated thermal cycles are have the effect of increasing alloying element diffusion. Rapid solidification of the melt pool on its own results in elemental partitioning to the melt pool boundaries and additional thermal cycling can lead to bands of alloying elements are the layer boundaries [1]. This has the potential to weaken the material mechanically.

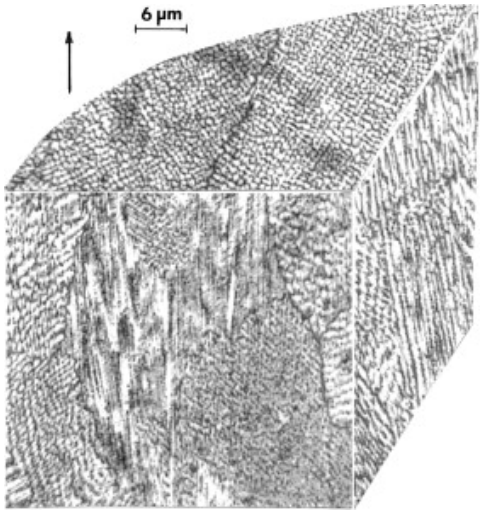

Figure 2.16: 3D optical micrograph showing fine cellular structure and columnar grains, with arrow representing the build direction [5]

Heat Treatment

In either processing route, heat treatment is applied to achieve the desired properties. As a precipitation hardened alloy, 718 requires specific heat treatment routes to induce the optimum formation of precipitates. The typical post-processing involves two steps. First, a solution treatment in the range of 980 °C to 1200 °C, followed by an ageing treatment at 650 °C to 900 °C for several hours [44]. The goal of the solution treatment is to dissolve the hardening elements into solution, while the ageing treatment serves to precipitate γ' and γ" phases for hardening [23].

2.2.3. Properties

Mechanical Properties

Differences in microstructure between AM and cast alloys naturally produce differences in mechanical properties. Anisotropy in properties is characteristic in AM components, with the Z-direction generally exhibiting the weakest properties [1]. Both anisotropy and mechanical properties can be improved with the addition of post processing treatments. Many properties greatly depend on the surface condition of the component, which is dependent on the SLM process and selected process parameters and can also be improved with post processing treatment. Differences in mechanical properties between AM and cast alloys are most pronounced in response to cyclic loading. In fact, the static mechanical properties of AM and cast samples are comparable or potentially identical [45].

Amato et al. studied the effect of different heat treatments (HIP, annealing) on the mechanical properties of SLM Inconel 718. This data, along with other mechanical data from literature, is compared in Table 2.2. Hardness increases following annealing and HIP, due to the formation of strengthening phases. Hardness is greater in SLM processed material compared to wrought annealed, most likely due to the finer grain size characteristic of SLM manufacturing. The tensile and yield strength of HIP + annealed SLM is comparable to wrought annealed material. The variance in strengths underscores the effect of heat treatment and subsequent microstructure on properties. In comparing the as-built hardness to solution annealed and aged material, it is clear that these treatments significantly improve the hardness of the alloy. Properties also depend heavily on the parameters - different annealing or aging times and temperatures result in significant differences in properties.

Table 2.2: Mechanical property comparison of wrought and SLM Inconel 718, with various heat treatments

Processing Method	YS (MPa)	UTS (MPa)	Elongation (%)	Hardness (HV)
SLM (as-fabricated, N atmosphere) [5]	830	1120	25	380-390
SLM/HIP/Annealed [5]	850-890	1140 -1200	28	
SLM/HIP/Annealed/Aged [44]	1084-1136	1334-1392	17.5-25	461-492
SLM/HIP/Annealed/Aged [46]	590-723	954-1117	13-20	
Wrought (annealed) [5]	830	1100	31	
Wrought (aged) [5]	1400	1600		373-472 [47]

2.3. Fatigue

The primary focus of this master work concerns the dynamic response of Inconel 718 produced by selective laser melting. The following section provides background on fatigue behavior generally, as well as behaviors or risks specific to additively manufactured metal alloys.

2.3.1. Mechanism

Metal fatigue can be defined as the failure of a material under a repeated or varying load, at a stress level which would not lead to failure in a static application. Failures due to fatigue are common, but particularly problematic as the failure occurs at loads lower than the yield or ultimate tensile stress of the material [48]. Fatigue occurs in three stages - crack initiation, crack propagation and final fracture. During crack initiation a defect or another stress concentrator creates localized plastic deformation in response to the applied load. This deformation leads to the formation of a crack. Additional loading cycles may cause this crack to propagate and eventually lead to final failure of the component [49]. Many factors are involved in crack initiation and propagation stages and control of these factors is critical in the prevention of fatigue failure. It is possible that a crack may form but never propagate.

Crack Initiation and Growth

All metallic structures contain internal or external defects introduced during production or use. These small defects reduce the area over which the external load acts, thereby increasing the stress locally at that defect. The increased stress intensity ahead of this defect depends on its geometry. If this stress locally becomes high enough, a crack will form and potentially grow. The crack initiation period includes the initial crack nucleation and the growth of a short crack - 'short' usually defined as a few grains long. This is referred to as a Stage I crack [48]. In the case of a sharp crack or other similar defect, the stress locally at the head of the crack tip may exceed the yield strength of the material and begin to deform plastically. The volume of material ahead of the crack tip is referred to as the plastic zone and it has a large influence on crack behavior. The presence of a plastic zone is the reason that metals can contain cracks and not fail, unlike a more brittle material.

The presence of a crack in a metallic component, whether present from production or initiated during service, does not necessarily result in the complete failure of the component. There exists a maximum permissible crack size, depending on the material and the loading conditions, above which the failure will occur. A small crack may grow to this permissible crack size and for this reason it is essential for engineers to understand the crack growth behavior.

When the short crack grows longer than a few grains of the material is becomes a Stage II crack. At this length the microstructure of the metal has less of an influence on the crack growth behavior, as the plastic zone at the crack tip includes several grains. The larger plastic zone can also induce crack closure effects, which reduce the crack tip stress intensity and retard crack growth. At this stage the crack generally propagates in a direction normal to the principle tensile stress plane [48, 49].

2.3.2. Characterization Methods

There are multiple methods by which the fatigue performance of a material can be evaluated and recorded. These methods may focus on the the crack initiation or crack growth behavior.

Stress-life Testing

In a stress-life approach, also called S-N, the cyclical applied stress is considered the primary parameter governing fatigue failure. This approach is used only in the case of high-cycle fatigue (HCF), meaning a high number of cycles to failure and little to no plastic deformation. Fatigue testing is performed by subjecting the specimen to cyclical loads at a certain stress amplitude until failure occurs. The number of cycles to failure is recorded as the dependent variable. Testing is repeated at a range of stress amplitudes and the cycles to failure recorded for each. This data is then plotted in log-log scale or semi-log scale with stress amplitude on the y-axis and cycles to failure on the x-axis. The resulting curve is referred to as an S-N or Woehler curve [49]. The generation of an S-N curve yields several pieces of useful information. On a log-log scale, the curve can be divided into two sections. The first, at lower cycles to failure, has a negative slope and is referred to as the finite life region. For some materials, the curve becomes horizontal at a certain stress level. This is the infinite life region and this stress level is the fatigue limit, meaning that below that stress level the component will theoretically not fail at any number of cycles. This is demonstrated in Figure 2.17(a). Some materials, such as aluminum, do not have an endurance limit. Their curve does not flatten but rather continues to decrease with increased cycling.

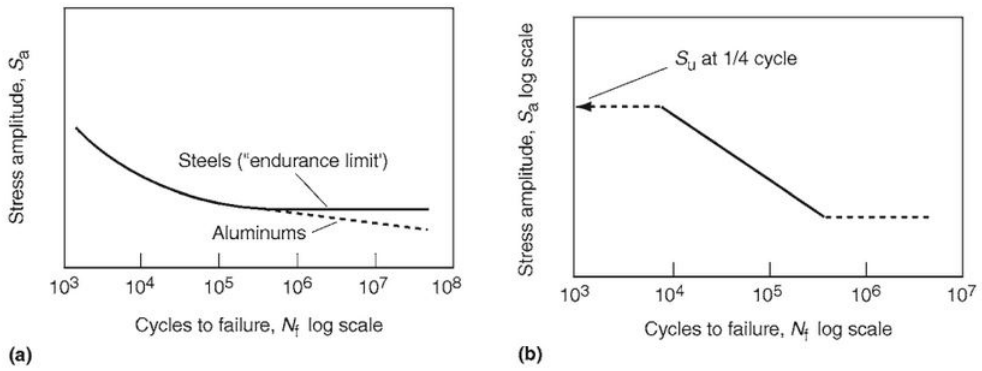

Figure 2.17: Woehler curves (a) stress vs log cycles to failure (b) log stress vs log cycles to failure [16]

To generate these plots, life cycle fatigue tests are performed at a range of applied maximum stresses. The corresponding cycles to failure are recorded and the results are plotted on an S-N plot, with the number of cycles to failure on the x-axis and the stress amplitude of the repeated load on the y-axis. The fatigue life can be evaluated using rectangular or cylindrical specimens in a three-point bending set-up. The specimen is constrained at two points with a certain span between them and a cyclic load is applied at a central point. It is important to record the applied stress ratio (R), which is defined as the ratio of the minimum stress to the maximum stress. The data points plotted on the log-log scale Woehler curve (Figure 2.17(b)) are often fitted using Basquin's relationship:

$$\sigma_a = A(2N_f)^b \tag{2.2}$$

$2N_f$ is the number of reversals to failure, σ_a is the true stress amplitude, A is the fatigue strength coefficient and b is the fatigue strength exponent. A and b are material fatigue properties. By comparison of these values, comparisons can be made between different materials or the same material produced differently in terms of their fatigue behavior.

2.3.3. Susceptibility of SLM Components to Fatigue Failure

As discussed previously, the manufacture of metallic components by selective laser melting creates a microstructure distinct from that created by traditional methods. This microstructure, surface condition and defects introduced in the process all contribute to a potentially poor mechanical performance in comparison to traditional processes. In particular for cyclic loading conditions, any defects that can act as stress concentrators are particularly dangerous for their potential to serve as crack initiation sites [17]. Of the two stages of fatigue failure - crack initiation and propagation - SLM process-induced defects have the greatest impact on crack initiation. Riemer et al. determined that crack growth behavior during high cycle fatigue was not influenced by defects such porosity or residual stress [17]. Fatigue crack growth is instead most heavily influenced by the microstructure. The columnar grains oriented along the build direction result in strong anisotropy in crack growth behavior.

Effect of Microstructure

As previously discussed, processing and post-processing of SLM Inconel 718 have a direct influence on the resulting microstructure, including phases and grain size. Schirra et al. reports that Laves phases may serve as crack initiation points for fatigue failure. This effect however was found to be negligible with smaller grain sizes [50]. It can then be expected that Laves phases will not have a significant effect on the fatigue behavior of as-processed SLM Inconel 718, but may on heat treated or HIPed material. Laves phases have another detrimental effect of fatigue - a large proportion of Laves phases may create a path for the crack to propagate through this brittle phase. Schirra et al. found that fatigue cracks propagated through the Laves phases.

Effect of Surface Roughness

High surface roughness of SLM components is well documented and one of the primary reasons to perform post-processing. Partially melted particles or large asperities concentrate the stress and create the potential for crack initiation. This negative impact of a rough, as-produced SLM surface can be eliminated with polishing. Spierings et al. found polished SLM material to exhibit a comparable fatigue limit as compared to a machined cast material. The fatigue limit of those samples was found to be significantly higher than the as-build SLM samples [45].

Effect of Porosity

Pores at the surface or sub-surface serve at points of stress concentration, which can lead to the initiation of cracks. These cracks, once formed, can propagate along pores as the energy barrier for crack propagation is lower [48].

Effect of Residual Stress

Residual stress in a component can result from variety of processes and, depending on the type and location of the stress, may be a benefit or a detriment to fatigue performance. Compressive stresses may induce crack closure and slow the growth of fatigue cracks, while tensile residual stress may have the opposite effect. It is currently not well understood how superimposed residual stresses affect crack growth in SLM metals [17].

Residual stress as a result of SLM processing does not appear to have any appreciable effect on crack growth behavior. Riemer et al. monitored fatigue crack growth of CT specimens using the potential drop technique and found no difference in crack growth curves between the as-built SLM 316L sample and one that was heat treated at 650°C [17].

Effect of Orientation

The layer by layer production of an SLM component creates anisotropy in the mechanical properties of the component and in the microstructure. The metal solidifies in columnar grains, creating a greater linear density of grain boundaries in the x- and y- directions than in the z- direction (build direction). Measured crack growth resistance was found to be lower in the build direction. A crack growing in a direction normal to the build direction is arrested more easily [17]. This difference is illustrated in Figure 2.18, which shows the increase in barriers to crack growth for a crack normal to the build direction. Porosity between the layers caused by lack of fusion also contributes to reduced fatigue strength in the Z-direction (build direction), compared to the X- and Y-directions [51]. Hot isostatic pressing (HIP) has been found to greatly reduce or eliminate this anisotropy in the microstructure through recrystallization and growth. As a result, the difference in fatigue crack propagation is eliminated. This is illustrated in Figure 2.18.

The surface condition is likewise dependent on the build orientation. In a simple vertical build, the surface roughness of the sides is 2-3 times as high as the top surface [1]. The effects of surface condition as described previously will therefore also depend on the build orientation.

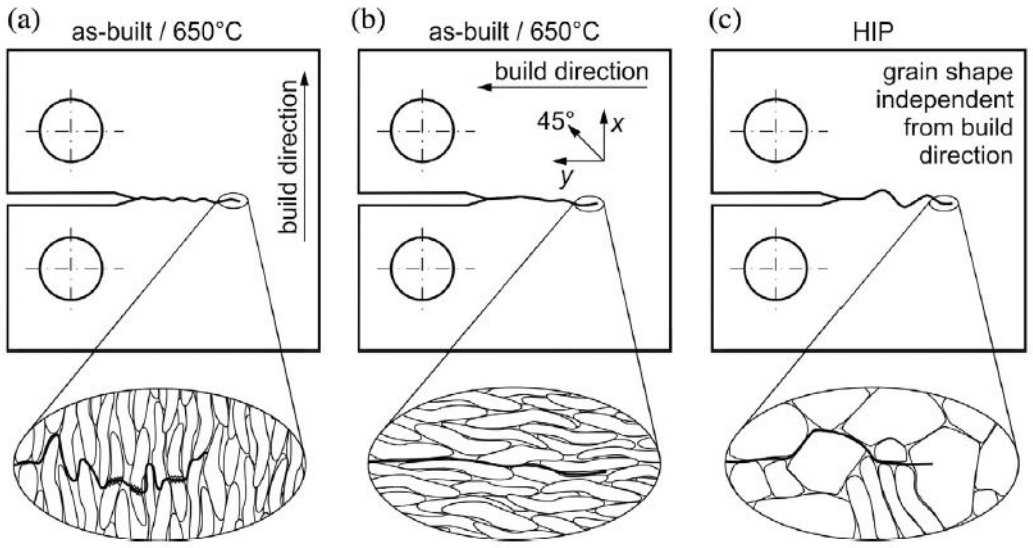

Figure 2.18: Illustration of the effect of orientation on fatigue crack growth for a crack (a) normal to the build direction, (b) parallel to the build direction and, (c) on an isotropic microstructure following hot isostatic pressing [17]

2.4. Modelling Approaches for Fatigue Behavior Prediction

In the development of additive manufacturing processing it is desirable to develop theoretical simulations to model the processing-microstructure-properties relationships. With these models, process development can occur without the time and expense of experimental iterations. Modeling of an AM process for metallic components poses several challenges, as it is necessary to understand the thermal history, residual stress distribution, and microstructural evolution in order to accurately predict the resulting mechanical properties. A summary of common modelling techniques can be found in Table 2.3. There are established computational methods for the modeling of microstructure evolution and thermal history which can be applied to the SLM process. This master work will focus in particular on the prediction of fatigue performance of SLM Inconel 718 based on initial microstructure, defects or surface condition.

Table 2.3: Summary of fatigue predictive models

Model	Output	Advantages	Limitations
Finite Element Analysis	Predicted S-N curve	Accurately predicts effect of small surface and internal defects	Typically requires experimental data as inputs
Fracture Mechanics	Kitagawa-Takahasi contour plots, predicted S-N curves	Accurate prediction of fatigue life based on defect distribution	Experiment based (requires extensive testing data), based on an initial defect size, does not predict crack initiation life
Continuum Mechanics	Fatigue life	Includes initiation, effects of AM processing	Does not factor in microstructure, anisotropy

2.4.1. Defect Sensitive Fatigue Prediction

Kitagawa-Takahasi Type Diagrams

Due to the sensitivity of fatigue performance to defects and notch effects, many researchers seek to model fatigue behavior based on defects present in the material. Le et al. utilized two different fracture mechanics approaches to model a link between pore size and fatigue life of SLM processed Ti_6Al_4V alloy [18]. Pore size was determined from SLM samples in multiple build directions, as high anisotropy in pore shape was observed. Fatigue testing was performed on cylindrical samples in three different orientation at constant stress amplitude, R of 0.1 and 20 Hz frequency. Pore size distribution was measured at the crack initiation sites on the fracture surfaces and this distribution was found to better correlate to fatigue behavior. Based on this information, the authors sought to create a model to predict fatigue life based on pore size. They used a fracture mechanics approach based on a the theory by Caton, who assumed that small crack growth rate is a function of the stress amplitude, macroscopic maximum strain and the yield strength of the material. Using the experimental information about defect size and equations proposed by Caton, a relationship between pore size and final fatigue life was developed:

$$S_{\text{max}}(corrected) = \sigma_{\text{max}}(\sqrt{area})^{1/2s}/(150)^{1/2s} \tag{2.3}$$

In this case s is a correction factor of about 1.67. The previously collected fatigue data was 'corrected' using this relationship so that maximum stress amplitude was normalized to one reference pore size, allowing the fatigue life data to be directly compared. This greatly reduced scatter in the S-N plot.

Kitagawa-Takahasi diagrams were generated from this corrected data. These diagrams are a method used to depict the relationship between defect size and fatigue strength. They are commonly used to determine the allowable stress range for infinite life, given a defect geometry and stress range. The results can be found in Figure 2.19, comparing the calculated values from the experimental. Pore size is on the x-axis, normalized maximum stress on the y-axis, and fatigue life is represented as colored iso-value curves on a log scale. The predicted results show fairly good agreement with the experimental results.

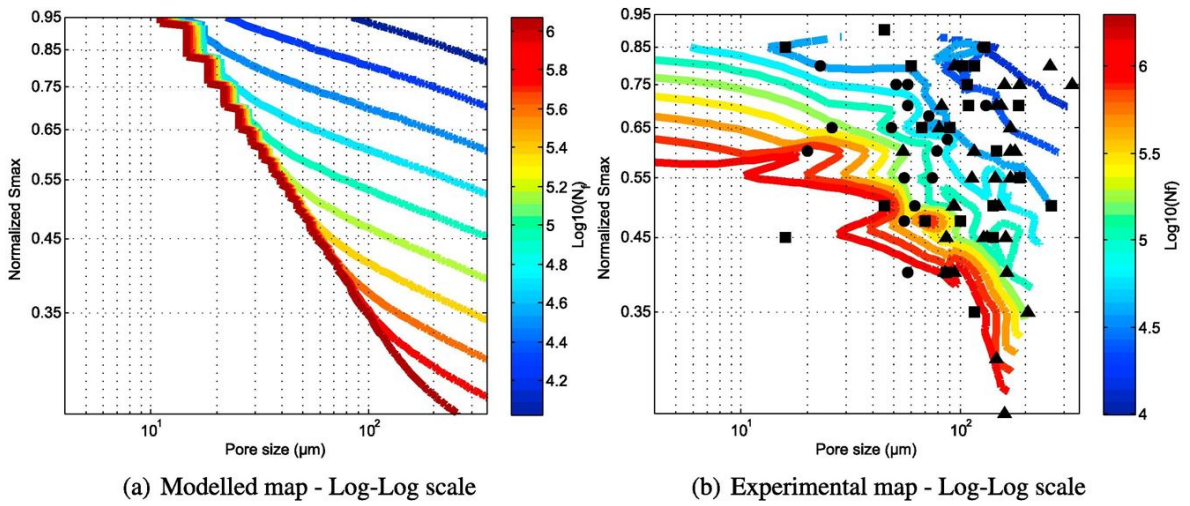

(a) Modelled map - Log-Log scale (b) Experimental map - Log-Log scale

Figure 2.19: Generalized Kitagawa-Takahashi diagram with iso-values curves, created with the Caton approach [18]

The Kitagawa-Takahashi diagrams are limited in that they can only predict fatigue life based on a defect size and therefore they can not be used to predict fatigue behavior of defect free samples. SLM metallic structures are highly unlikely to lack defects in the microstructure and therefore this approach has gained popularity in fatigue life prediction of AM components.

Ngnekou et al. studied the impact of defect size on fatigue resistance of SLM $AlSi_{10}Mg$ [52]. They characterized the microstructure of the alloy in terms of melt-pools, crystallography, dendrite structure and precipitates. S-N curves were generated for two different build orientations of rotating bending fatigue samples with R = -1. They also generated Kitagawa-type diagrams, using the same pore size assessment used by Le et al. (Murakami parameter). The resulting curve demonstrated a dependence of fatigue life on defect size, but not defect type. The Kitagawa diagram also demonstrated the existence of a critical defect size, beyond which fatigue limit is only dictated by the size and is not influenced by the microstructure.

Fatigue-life prediction utilizing the Kitagawa-Takahashi diagram and/or Murakami methods have been successfully verified with experimental results. A major limitation however, is the necessity of extensive experimental test data with which to build the diagram. In the case of AM materials, availability of test data in the literature is limited [53].

Finite Element Methods

Finite element analysis (FEA) methods are widely used to model mechanical behavior. Gupta et al. utilized ANSYS separating morphing and adaptive re-meshing technology (SMART) fracture software to create a crack growth simulation for AM Ti_6Al_4V [19]. Experimental data on long crack growth was modified to be more applicable for short crack growth, by correcting closure effects. Using the software, they were able to generate stress vs number of cycles prediction curves that could then be evaluated against experimental results. The methodology used by the authors is outlined in Figure 2.20. First crack growth data from literature was inputted into the SMART simulation and crack propagation rates for various crack sizes were generated. From these crack propagation curves, the correction factor U for small cracks was obtained using polynomial regression. Using this fit, the number of cycles to fracture N was calculated using the equation in Figure 2.20.

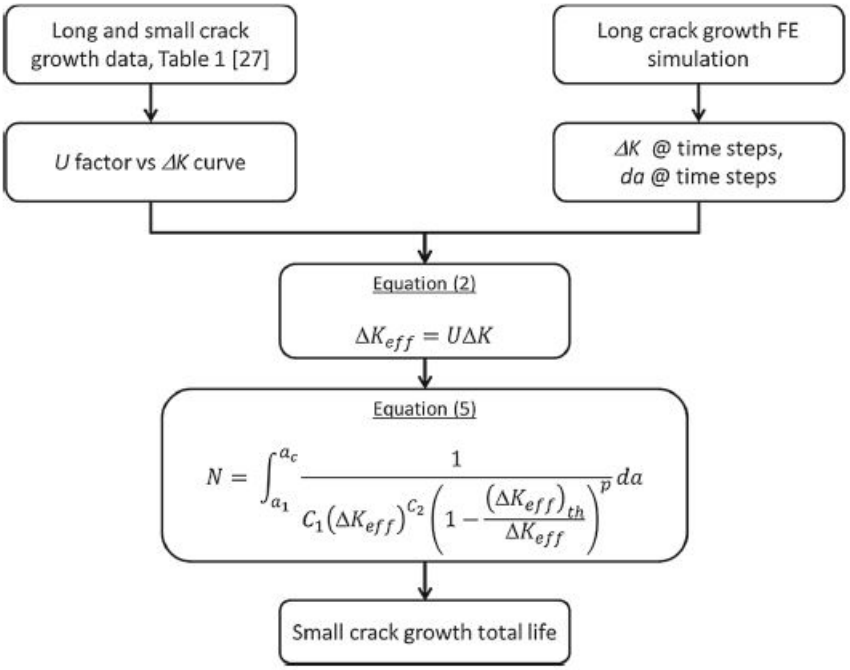

Figure 2.20: Overview of methodology used by Gupta et al. to model small crack growth [19]

Figure 2.21 shows an example stress vs cycles to failure prediction output from SMART. This case models cycles to failure for various initial defect sizes. This prediction was then compared with experimental data from literature and showed relatively good fit. Initial defect sizes in the literature data were obtained by fractography of the surface following final failure.

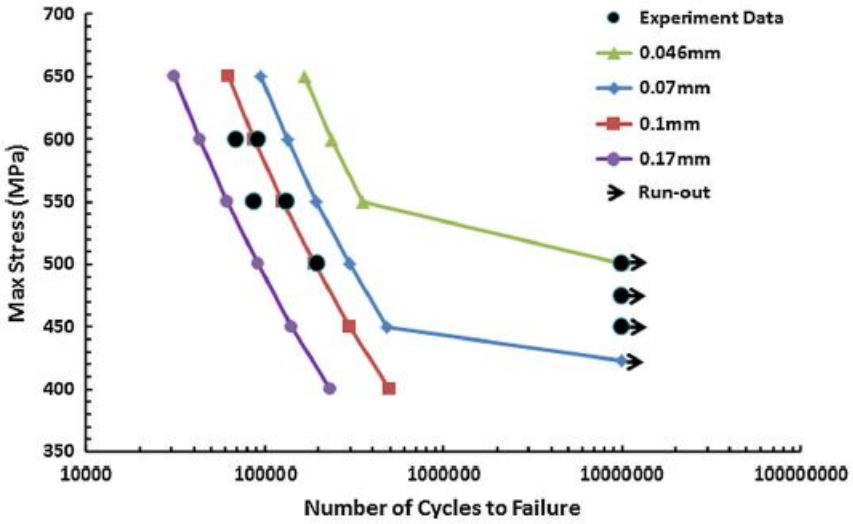

Figure 2.21: Crack growth prediction by SMART vs. experimental results [19]

Grohs also utilized FEA methods to predict fatigue life of SLM titanium and steel alloys [20]. He used Ansys Workbench strain life analysis to generate S-N curves of a rough surface, simulating the surface as a series of notched stress concentrators represented as a sine wave. This meshing example is seen in Figure 2.22. Using this notch geometry as a input, the fatigue life was calculated using the software. The results are shown in Figure 2.23 for different period lengths and an inputted surface roughness of 26.7 µm.

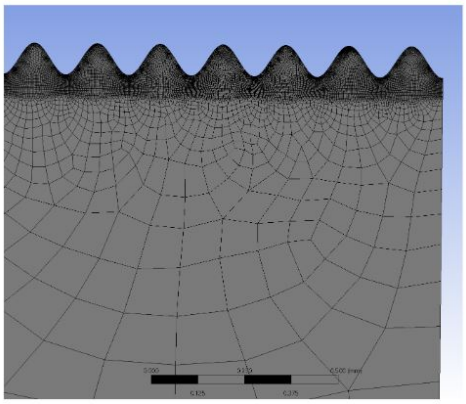

Figure 2.22: Detail of sine wave meshing [20]

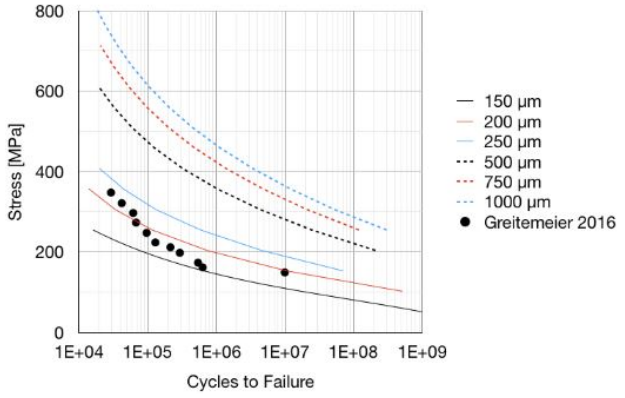

Figure 2.23: Prediction of fatigue life using sine wave notches of differing periods overlaid with experimental results [20]

A parametric study was run using the software to refine the strain life parameters and the results showed good fit with experimental data. This indicates that fatigue life of an SLM component can be predicted solely based on surface roughness.

Continuum Damage Mechanics Approach

Continuum damage mechanics (CDM) is a method of fatigue life prediction that considers crack initiation and growth as a continuous process, rather than considering each stage separately as in fracture mechanics. Research applying this method to AM materials is currently limited.

Zhan et al. used CDM to predict fatigue life of SLM 316L [54]. First, elastoplastic constitutive equations of fatigue damage were derived, including damage incurred during the AM process by integrating the volumetric energy density into the equations. This was done by first establishing a reference volumetric energy density (VED) which resulted in the minimum porosity. The ratio of VED used in the production to reference VED incorporated into the equations served to represent the level of damage incurred during processing. The output of these calculations is the number of cycles to failure. It was concluded that fatigue life increased as the VED ratio increased, as would be expected if actual VED was closer to the 'reference' VED. As the VED ratio decreased, the damage evolution rate increased.These studies fail to take defect size and distribution into account and are therefore their practical applications are limited, as defects have been found to have major impact on the fatigue life of SLM components.

2.5. Conclusions

- Inconel 718 manufactured by selective laser melting results in a microstructure and in mechanical properties distinct from that of a traditionally wrought component. Without post-processing treatment the microstructure is fine grained, anisotropic and more likely to contain processing defects. These defects include porosity, residual stress, surface roughness and inter-layer voiding.
- Poor surface quality (high roughness, presence of notches) has a significant impact on the fatigue life of SLM Inconel 718. The reduction of porosity, in particular lack of fusion porosity, and surface defects through processing or post-processing techniques is therefore the most effective method in improving fatigue performance.
- Factors such as small non-metallic inclusions or residual stress less significant in the fatigue performance of an SLM component, which is instead controlled by the presence of larger surface defects and pores.
- Process defects can be reduced through the tuning of process parameters, most notably laser scan speed and laser power.
- Machining/polishing and hot isostatic pressing have been shown to successfully reduce surface roughness and porosity, respectively, to levels acceptable for cyclic loading. Laser remelting of each layer or of the surface can also significantly improve surface quality and fatigue performance.
- Modelling of the fatigue life behavior of an SLM manufactured component is complex, but can be predicted using information about defect size and location or with assumptions of surface roughness geometry.

2.6. Research Approach and Objectives

It is clear from the literature that performance of material during cyclic loading is highly dependent on the surface condition and process defects. Both of these factors are controlled by the SLM process parameters and to this end it is important to understand the effect of process parameter alteration on the result. Post-processing treatment would clearly also have an effect on the resulting surface and microstructure. In the investigation of these factors for this master work, the following research objectives are identified:

1. Characterize how differing SLM layer thicknesses and build direction affects microstructure, defects and surface condition.
2. Characterize how two different post-processing surface treatments (electropolishing and mechanical polishing) affect the surface condition, near-surface porosity, and resulting fatigue performance.
3. Develop a predictive model for the fatigue limit of SLM Inconel 718 based on defect size and location.

3

Materials and Methods

3.1. Material

The samples obtained for this master work were fabricated by selective laser melting in an argon atmosphere from a pre-alloyed powder. They were produced externally prior to the beginning of the thesis and the SLM process parameters are proprietary - and therefore unknown. The sample population consists of cylindrical fatigue samples (Figure 3.4) fabricated with two different SLM powder layer thicknesses - 80 µm and 40 µm - and in two different build directions - vertical and inclined. The inclined samples were produced at an angle of 63 ° from the horizontal (Figure 3.1). There were also three different surface conditions - as-built, electropolished, and mechanically polished. The resulting twelve different sample groups are summarized in Table 3.1, including the way in which the groups will be denoted in subsequent chapters.

Figure 3.1: Inconel 718 samples after SLM processing and before post-process heat and surface treatment

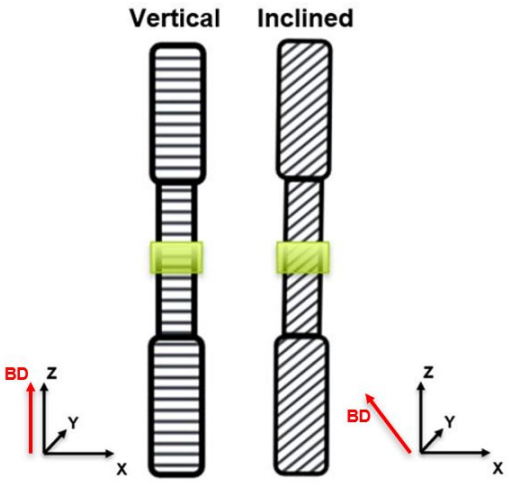

Figure 3.2: Location of section taken for hardness and microscopy and labeling of planes

Sample axes and planes were labeled as in Figure 3.2. The Z direction is always along the length of the sample, which corresponds to the build direction in the case of the vertically built samples and to 63 degrees from the build direction in the case of inclined samples.

Table 3.1: Sample summary

Layer Thickness	Surface Condition	Build Orientation	# of Samples	Key
80 µm	As-Built	Vertical	5	80/AB/V
		Inclined	4	80/AB/I
	Electropolished	Vertical	5	80/EP/V
		Inclined	4	80/EP/I
	Mechanically Polished	Vertical	5	80/P/V
		Inclined	6	80/P/I
40 µm	As-Built	Vertical	3	40/AB/V
		Inclined	2	40/AB/I
	Electropolished	Vertical	6	40/EP/V
		Inclined	5	40/EP/I
	Mechanically Polished	Vertical	2	40/P/V
		Inclined	2	40/P/I

All specimens were subjected to post-processing heat treatment consisting of hot isostatic pressing (HIP), solution annealing, followed by age hardening. The exact temperatures and duration of the heat treatment are proprietary and not available. However, a standard heat treatment of SLM Inconel 718 in the literature consists of HIP at 1200 °C and 120 MPa for 3 hours. The subsequent solution treatment is performed at 980 °C for a duration of 1 hour, followed by a water quench. Age hardening is a two step process, with the first aging performed at 720 °C for 8 hours and the second immediately after at 620 °C for 8 hours. The material is then air cooled until it reaches room temperature.

The difference in appearance of the three different post-processing techniques can be seen in Figure 3.3. The black surface of as-built sample is attributed to high temperature reaction during the heat treatments.

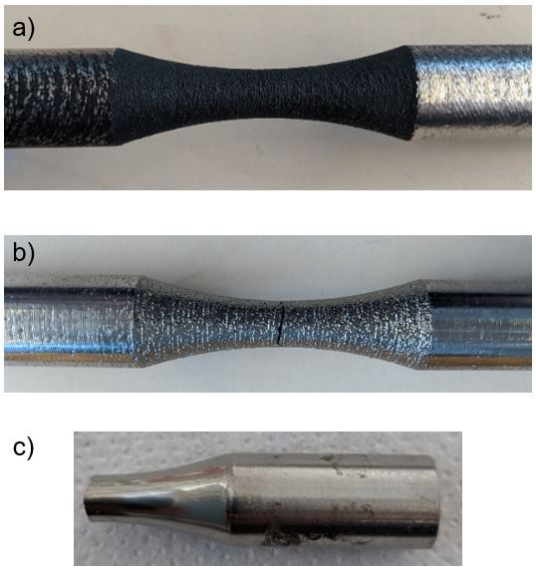

Figure 3.3: a) As-built, b) electropolished and c) mechanically polished fatigue specimens (after testing)

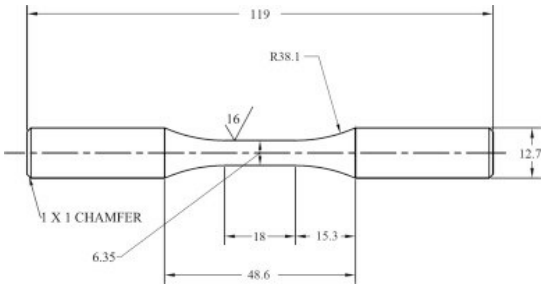

Figure 3.4: Dimensions in mm of rotating bending fatigue samples [21]

In the case of inclined samples, the 'upskin' side refers to the 180 ° plane facing the build direction. The 'downskin' side is the opposite. The two post-processing surface treatments result in removal of material from surface, particularly in the case of mechanical polishing. Table 3.2 summarizes the material reduction at the surface in the gauge section. This was determined through measurement of each sample at the smallest cross-section, calculating an average, and then determining the difference in average after each post-processing treatment.

Table 3.2: Material loss from the surface from post-processing surface treatment, measured in the gauge section

	As-built	Electropolished	Mechanical polish
Avg. diameter (mm)	6.31 ± 0.0091	6.29 ± 0.11	4.80 ± 0.017
Avg. material lost (µm)	-	12.2	755

Powder Analysis

A sample of the feedstock powder for the SLM process was obtained and analyzed using SEM microscopy. The average grain size was previously found to be 30 µm. A representative image of the morphology and size distribution of particles is shown in Figure 3.5. The powder particles are largely spherical, with a distribution of sizes ranging from approximately 5 to 50 µm in diameter.

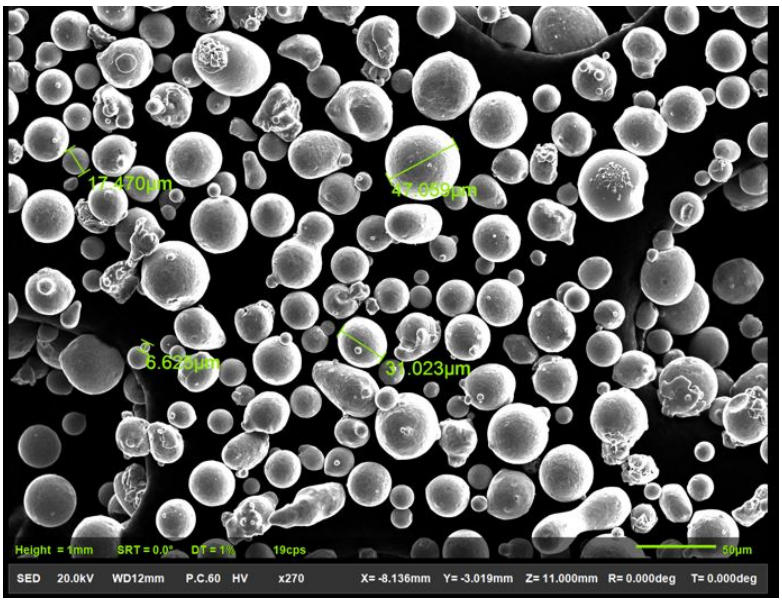

Figure 3.5: SE image of Inconel 718 feedstock powder used for sample fabrication

3.2. Microstructural Characterization

Composition

Alloy composition was determined by XRF measurement of a representative sample. It was assumed that composition was equal across all sample groups. The measurement was performed using a Panalytical Axios Max WD-XRF spectrometer. Table 3.3 shows the measured composition. Note that this technique does not detect light elements such as carbon or nitrogen.

Table 3.3: XRF composition of Inconel 718 material

	Ni	Cr	Fe	Nb	Mo	Ti	Si	Al	Cu	Mg
Conc. (wt%)	53.43	18.734	17.646	4.927	3.174	1.021	0.545	0.434	0.066	0.024
Absolute error (wt%)	0.2	0.1	0.1	0.06	0.05	0.03	0.02	0.02	0.008	0.005

Sample Preparation

A slice of material was taken from the gauge section of a representative specimen of each sample group. The slices were sectioned to expose the plane parallel to the length of the sample. In the case of incline build samples, care was taken to include both upskin and downskin sides. The XY and XZ planes (see Figure 3.2) of the mounted samples were ground and polished to 1 µm prior to optical microscopy, porosity and hardness measurements.

Microscopy

Samples were ground and polished to 1 µm in both the XY and XZ directions. Following polishing, samples were etched with Kalling's reagent. Optical microscopy was performed using a Keyence VHX-5000. SEM microscopy was performed using a JEOL JSM-IT100 in secondary and backscattered electron imaging modes. SEM-EDS analysis was performed in backscattered electron mode at 20 keV accelerating voltage.

Hardness

Vickers hardness was measured according to ASTM B933, using a Struers Durascan 70 microhardness tester. All measurements were performed at a load level of 1 kgf (HV1). Measurements of bulk hardness were performed in the center of the polished, unetched samples in both XY and XZ directions. At least five measurements were performed for each sample group and orientation and the results averaged. For the purposes of fatigue life prediction, hardness was measured at the near surface of the polished samples in the XY plane, as crack initiation occurred at the surface or near-surface. Again, at least five measurements were performed and the results averaged. In the case of incline-built samples, near-surface hardness was measured both at the upskin and downskin side.

Density

Density was measured using the Archimedes method according to ASTM B311. Only samples of the polished surface condition were measured, to reduce effects of a rough surface, which could trap air bubbles and affect the results. 5 samples of at least 1 gram were measured and the results averaged. A wrought Inconel 718 sample was measured in the same way and the results averaged to serve as the reference density. Relative density (as a percentage) was determined by dividing the obtained density by a reference density.

Surface Roughness

Due to equipment limitation, roughness could initially not be measured via laser interferometry and was instead determined by light interferometry using a Keyence VHX-5000. A 3D surface was generated using image stacking from a level area of the gauge section. From the 3D surface, line profiles of the surface were extracted. The line profiles were along the Z direction to ensure a level surface, as the software was not capable of form removal. Line roughness could then be calculated from the .csv line profile data according to the following equation, also visualized in Figure 3.6:

$$Ra = 1/l_r \int_0^{l_r} | z(x)dx | \tag{3.1}$$

A MATLAB program (see Appendix B) was developed to convert the line data into line roughness Ra according to equation 3.1. For each sample group - and upskin vs. downskin sides for inclined samples - the roughness of at least 10 profiles was calculated the results averaged.

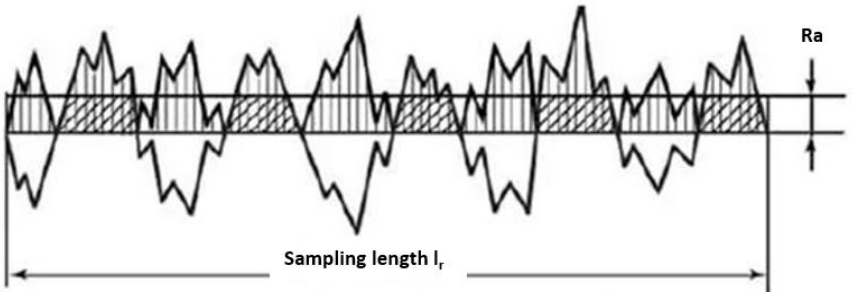

Figure 3.6: Representation of Ra calculation from surface line profile [22]

This method is limited by the resolution, which is lower than that of a laser interferometer. The 3D surface profile generated by the microscope in Figure 3.7 seems to demonstrate the ability of the technique to pick up general peaks and valleys due to the weld pools, dictated by the scan pattern. It does not however, recognize the height of the partially melted particles, which would have a significant impact on roughness.

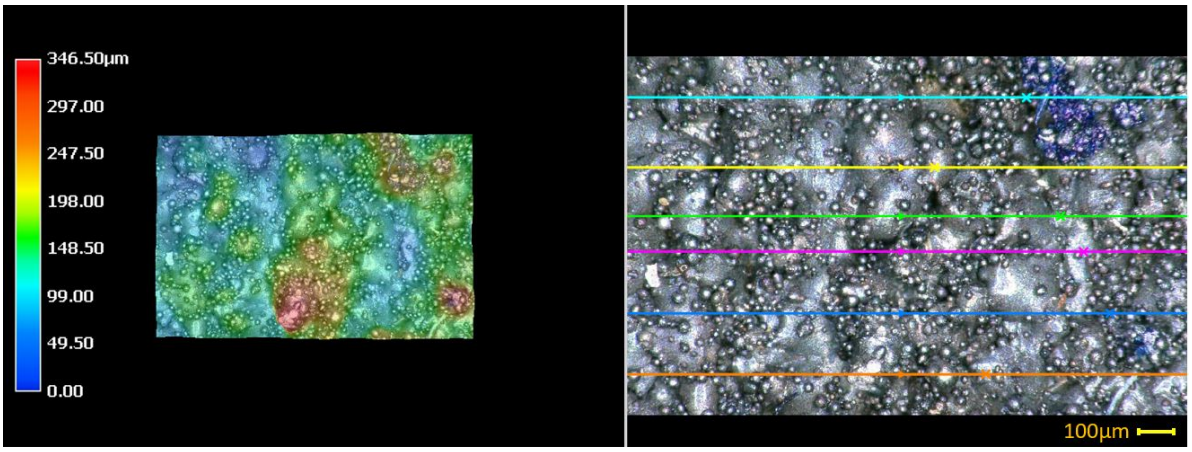

Figure 3.7: 3D surface profile (left) and lines for roughness measurement (right)

Surface roughness (R_a) was then measured using a Brucker NPFlex non-contact profilometer at 20x magnification. This instrument allowed for roughness measurement of an area and not of a single line. The output is a 3D topography of the surface (from which 2D profiles may be extracted) and various roughness metrics beyond R_a. The advantages of this measurement technique include higher resolution, ability to identify and measure crevices and ability to stitch sections together to measure a greater area. Figure 3.8 shows the output of roughness measurement.

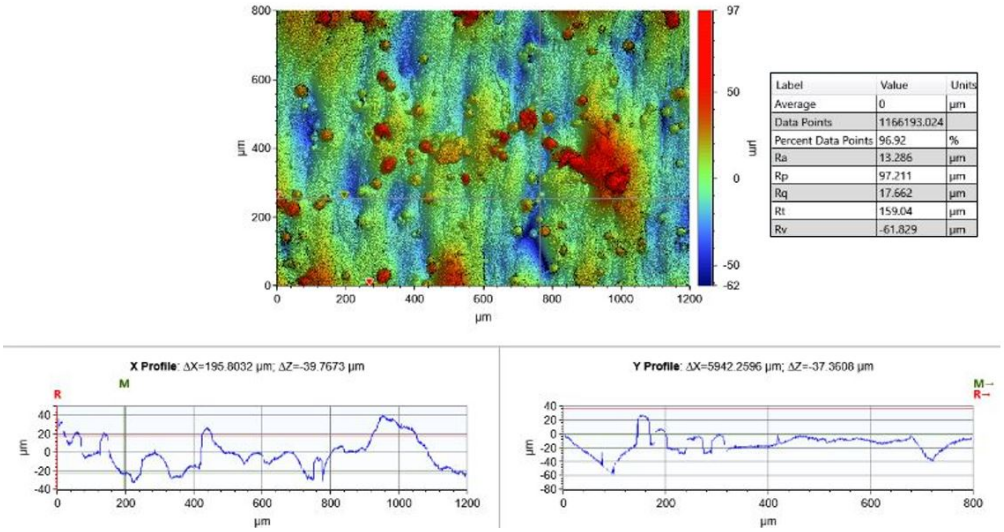

Figure 3.8: 3D surface profile, X and Y profiles, and roughness data analysis from the Brucker NPFlex

X-ray Diffraction

X-ray diffraction analysis was performed on the feedstock powder and on printed samples for the purpose of phase identification. The printed sample group analyzed was the 40 µm, electropolished, inclined group. The electropolished group was selected as this was the focus of the fatigue prediction work. From an initial microstructural investigation, it was determined that phase composition between the sample groups was not perceivably different and therefore one of the samples could be assumed to be representative. The analysis was performed using a Bruker D8 Advance diffractometer with Bragg-Bretano geometry and a Lynxeye position sensitive detector. Cu Kα radiation was used.

Micro-CT

Select samples were analyzed using a Phoenix Nanotom S micro-CT (computed tomography). The output was a 3D depiction of the sample in the gauge section, with darkened areas indicating porosity. The software was not equipped to automatically measure defect size or distribution, so this was done manually. Slices were selected in the XY plane in which the defect appeared to be largest. An example of a XY plane slice with visible surface defects is found in Figure 3.9. Images of these slices were imported into the open-access ImageJ processing program and the defect area measured by hand, using the scale bar as a measurement reference (Figure 3.10). As such, the process is open to human error.

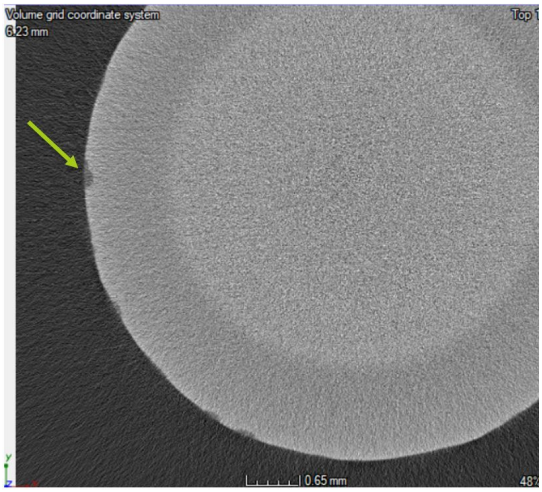

Figure 3.9: XY plane of CT sample showing surface defects

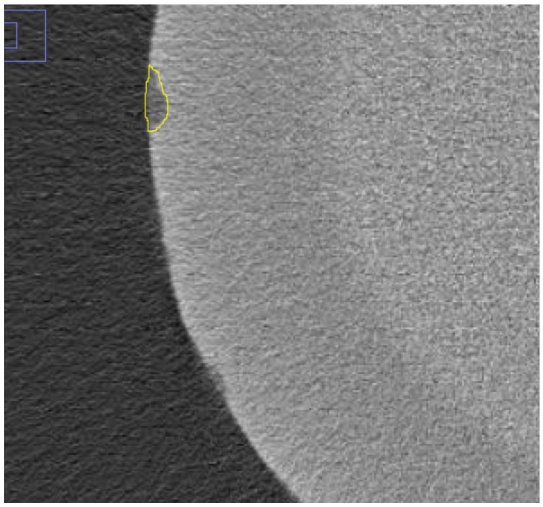

Figure 3.10: Surface defect measurement

Statistical Analysis

Box and whiskers plots were used to represent characterization measurement data for the purpose of visual comparison between different sample groups. One such plot is shown in Figure 3.11. The 'box' is constructed by determining the median and the interquartile range (IQR) of the data set. 50% of the data lies within the range of the IQR, or between the lower quartile value and the upper quartile value. The line in the box represents the median of the data set. The 'whiskers' are the thin lines projecting from either side of the box and they typically represent the range of the data. In some cases outliers are identified. An outlier is defined as any data point further away than 1.5*IQR from the upper or lower quartile values. This data point is represented by an asterisk and not included in the range. Box and whisker plots allow for quick visual comparison of two populations. They provide information such as the overall spread of the data or the skew towards one extreme [55].

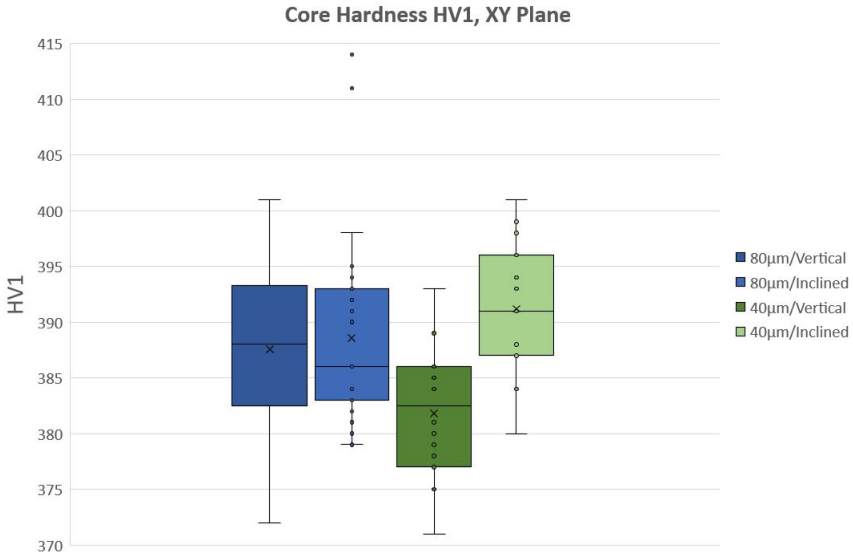

Figure 3.11: Example box and whisker plot of hardness

Fischer least significant difference (LSD) tests were used to determine if observed differences between two populations were statistically significant. This involved first performing an analysis of variance (ANOVA) on the data. This method analyzes several different groups of data and returns whether or not a result is significant. If it is significant, then the null hypothesis is rejected, meaning that one or more of the evaluated groups is significantly different from the others. It does not however show which group or groups are different. The Fischer least significant difference test is then used to compare individual groups. This is done by calculating the least significant difference for a set of two groups, using the following formula:

$$LSD_{\mathrm{A,B}} = t_{0.05/2}\sqrt{MSW(1/n_A + 1/n_B)} \tag{3.2}$$

In the above, $t_{0.05/2}$ is the critical t value found via a t-distribution table, MSW is the mean square within, taken from the ANOVA result, and n is the number of data points in each group [56]. This LSD result is then compared to the absolute value of the difference in means between the two groups from the ANOVA result. If the LSD is less than the difference in means, then the null hypothesis is rejected with 95% certainty and the two groups are statistically distinct. If LSD is greater than the difference in means, the null hypothesis is accepted.

3.3. Fatigue Testing and Analysis

3.3.1. Rotating Bending Fatigue

Fatigue testing was performed at an external testing laboratory prior to the beginning of this project. The testing followed ASTM E468-18, with a loading ratio of R = -1 with a frequency of 100 Hz. Testing was continued until failure or until 10 million cycles, at which point the sample was labeled a run-out.

3.3.2. Fractography

The fracture surface of failed fatigue specimens was examined with both optical and SEM microscopy. Prior to examination, the samples were cleaned ultrasonically for 5 minutes in isopropyl alcohol.

Determination of Crack Initiation Point

The crack initiation point, as well as the size and morphology of the initiating defect were identified and measured. In the case of multiple initiation points, common with samples of poor surface quality, care was taken to identify the primary initiation point. The initiation point was identified through typical fractography methods. The point can be identified by observing river patterns radiating from one location. In the case of multiple initiation points, the location which was the center of the largest radial area was taken as the primary point. This is illustrated in Figure 3.12.

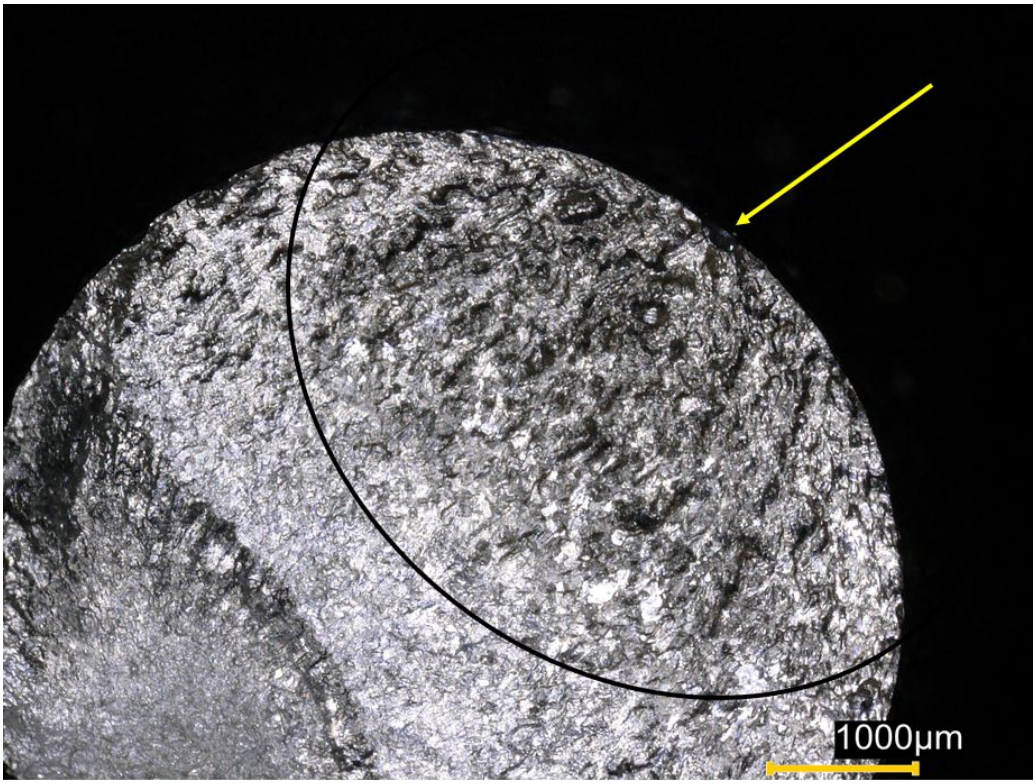

Figure 3.12: Fatigue crack initiation point identification

In many cases the initiation point was not so easily determined. The fracture surfaces of specimens with poor surface quality often contained multiple initiation points or cracks which initiated along a length of surface.

Defect Size Determination

Once the initiation point was identified, the area of the defect was measured using the $\sqrt{area}$ method proposed by Murakami. This method measures the effective area of the defect in the plane which is perpendicular to the loading direction, which in this case was the length of the sample. For defects of complex geometries the area is measured in such a way that it encompasses the defect. If a defect is near the surface or projects into the sample, the area from the defect to the surface is also included in the measurement. In the case that a crack originates at multiple locations along the edge, as is a common occurrence with samples of poor edge quality, then the area is measured as shown in Figure 3.13. The $\sqrt{area}$ is approximated to be $\sqrt{10}$ times c, the depth of the defect.

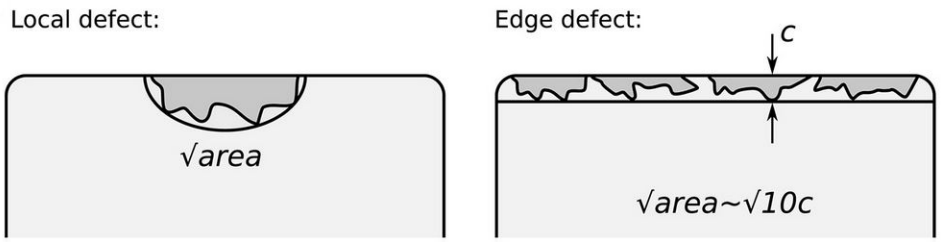

Figure 3.13: $\sqrt{Area}$ measurement of surface and edge defects [23]

3.3.3. Fatigue Limit Prediction Approach

The prediction of fatigue limit was historically difficult for engineers due to the strong dependence of fatigue performance on defects. Murakami proposed a prediction model for the fatigue limit of a material containing small defects. Such defects, particularly surface defects, are known to be common in additive manufactured materials and known to be initiation points for fatigue failure. This predictive approach was therefore considered likely to be successful with this material and has been done with success in literature. The end goal of the prediction is an estimate of the fatigue limit. This begins with determination of the threshold condition for non-propagating cracks ΔK_{th}. When this condition is known, it can be applied to a material containing small defects, such as an SLM manufactured sample, to determine the fatigue limit. In this case, the formula for stress intensity factor (SIF) can be modified for a large defect in place of a crack length.

$$\Delta K = 0.65 * \Delta\sigma * \sqrt{\pi * \sqrt{area}} \tag{3.3}$$

ΔK has units of MPa$\sqrt{m}$, area of $\sqrt{m}$, and $\Delta\sigma$ of MPa. The relationship between ΔK_{th} and crack size a has been well established, with ΔK_{th} increasing with increasing crack size. It follows that ΔK_{th} can also be related to $\sqrt{area}$, defined as the projected area of a defect onto the plane perpendicular to the tensile stress. Figure 3.14 demonstrates this relationship for various metallic alloys. For all materials evaluated in this study by Murakami, the relationship in a log scale is linear with a slope of 1/3. The following proportional relationship was therefore established:

$$\Delta K_{th} \propto \sqrt{area}^{1/3} \tag{3.4}$$

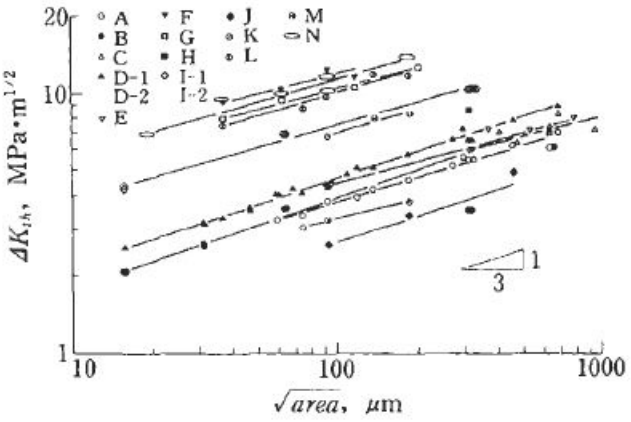

Figure 3.14: Relationship between ΔK_{th} and $\sqrt{area}$ for different materials [24]

ΔK_{th} is typically determined for a given material; therefore, its prediction must include something of the material property. Various material properties have been found to correspond with ΔK_{th}, but hardness HV is used primarily due to the simplicity of measurement. Murakami used the least squares method to fit a line to the data in Figure 3.14, resulting in the following relationship between threshold stress intensity and defect $\sqrt{area}$ that can be broadly applied to many alloys [24].

$$\Delta K_{th} = 3.3 * 10^{-3} * (HV + 120) * (\sqrt{area})^{1/3} \tag{3.5}$$

An equation for calculating fatigue limit stress as it relates to defects can then be determined using the above equation and the relationship in equation 3.3. This yields the following, valid for a loading ration of R=-1.

$$\sigma_{wl} = 1.43(H_v + 120)/(\sqrt{area_{max}})^{1/6} \tag{3.6}$$

The units for H_v material hardness are kgf/mm^2, $\sqrt{area}$ is in µm and σ_w. The equation creates a prediction of fatigue life related to material properties and defects in the material. It is valid for a variety of defects, including geometrical surface defects such as notches or large microstructural features such as inclusions. The equation is described by Murakami and Endo as semi-theoretical and semi-empirical.

Murakami et al. proposed equation 3.6 as the lower bound of a prediction of the fatigue limit of a material. This lower bound is defect dependent. The upper limit of this range is material-specific and represents the fatigue limit if defects or inclusions do not have an influence. It is based on an empirical relationship between hardness and fatigue life, valid from hardness values < 400HV [57].

$$\sigma_{wu} = 1.6 * H_v \pm 0.1HV \tag{3.7}$$

The upper bound of fatigue prediction is represented by equation 3.6 and is obtained through characterization of defects present in the material.

4

Results and Discussion - Characterization

4.1. Microstructure

4.1.1. Powder Analysis

Morphology

Figure 4.1 shows the distribution of size and shape of the Inconel 718 feedstock powder used for the production of samples in this study. Feedstock powders for SLM processing are typically produced through an atomization process in either gas or water. The size and shape of the resulting powder depends on the process used. The ideal powder contains spherical particles of varying sizes to facilitate better packing density and reduce porosity in the resulting part.

In this case, the powder particles are observed to be largely spherical, with some particles that are irregular in shape. Figure 4.2 shows a cross-sectional view of one of these particles. A number of satellites (smaller particles attached to larger spheres) are present on many of the particles. These satellites form during the atomization process. Apparent necking was also observed in some powder particles, creating elongated oblong shapes.

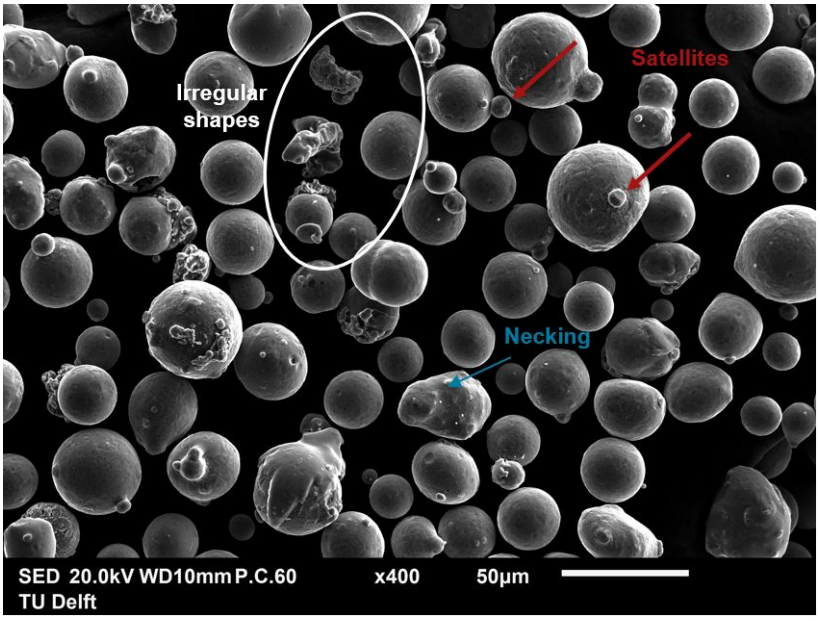

Figure 4.1: Optical micrograph of Inconel 718 powder cross-section

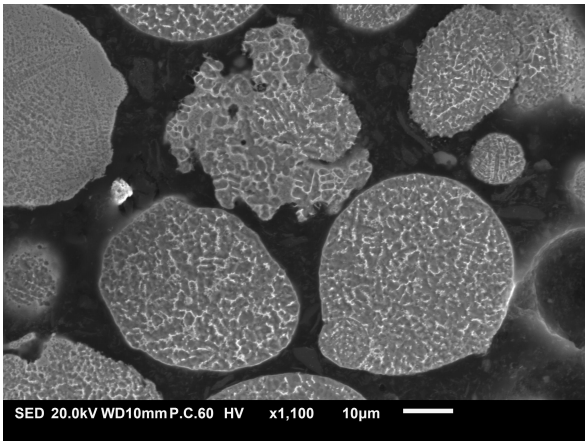

Figure 4.2: Secondary electron image of powder cross-section

The morphology of the powder can have an effect on the resulting SLM microstructure produced. One key quality of the powder is flowability, which affects how well the powder can form a good quality layer leading to a dense part. Flowability can be limited by friction or interlocking between the powder particles, the severity of which is a direct result of the powder morphology. A sphere is the ideal particle shape, as it does not allow for interlocking and minimizes friction by way of minimized surface area [58].

The observed irregularly shaped and elongated particles may pose a concern in terms of flowability. The process used for creating this powder is unknown and therefore only speculation is possible as to the cause of this irregular morphology. The powder morphology does bear close resemblance to recycled Inconel 718 powder studied by Nguyen et al. and recycling could be an explanation for the morphology [59]. That study found that recycled powder contained more satellites and irregularities as compared to virgin IN718 powder and that recycled particles tend to stick together. In turn, the recycled powder exhibited lower packing density and decrease flowability. These are powder characteristics that may be measured in a further study.

Microstructure

A cross section of the powder revealed a dendritic microstructure (Figure 4.3) typical of SLM powder. There were also small titanium nitride particles identified (Figure 4.4), ranging in size from less that 1 µm to approximately 5 µm. The composition of these inclusions was confirmed with SEM/EDS analysis (Figure 4.5).

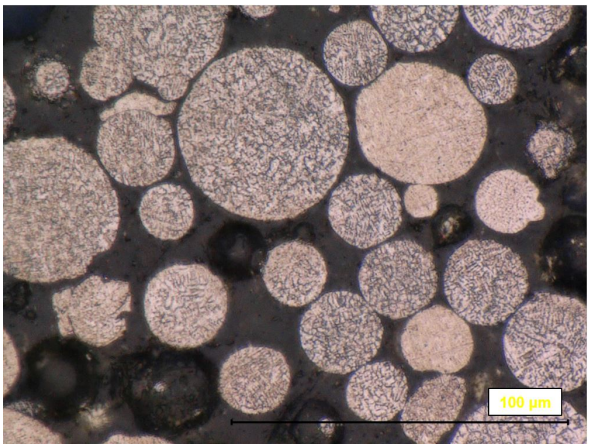

Figure 4.3: Optical micrograph of Inconel 718 powder cross-section

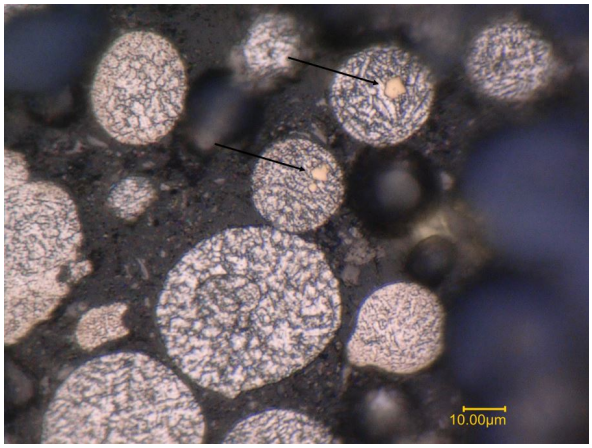

Figure 4.4: Optical micrograph of Inconel 718 powder cross-section with titanium nitrides

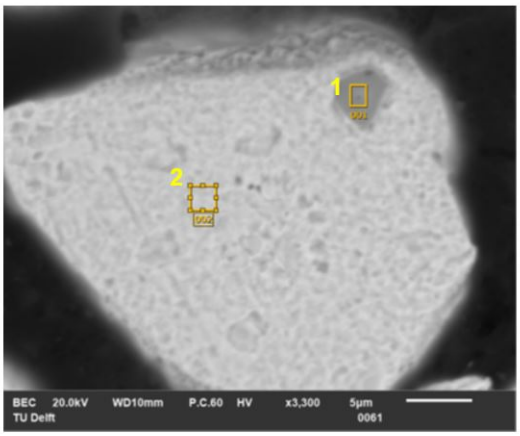

		Fe	O	C	N	Al	Ti	Cr	Mn	Ni	Nb	Mo
1	wt %	1.13	3.33	2.67	24.57	0.58	54.99	1.34		2.76	8.62	-
2	wt %	18.38	0.34	3.71	-	0.38	1.26	18.48		47.01	6.40	4.03

Figure 4.5: Backscattered electron image of 718 powder cross-section with titanium nitrides (top) and EDS quantification (bottom)

The source of this contamination is not clear without knowing the process by which the powder was created. If the powder is indeed recycled, that could be a source of the nitride.

4.1.2. Microscopy Results

Between the different sample groups, the microstructure was not dramatically different from a qualitative inspection. The general appearance of the microstructure was of fairly large grains, with secondary phases within grains and decorating grain boundaries. Distinct grain boundaries are not easily discernible, but phases or precipitates along the boundaries indicate grains are fairly uniform in size and equiaxed (Figure 4.6). Beads of layer deposition, characteristic of selective laser melted structures, could not be seen in the polished samples, nor could a fine cellular structure. The HIP treatment was therefore successful in inducing recrystallization in the microstructure and removing any significant anisotropy. Smaller grains were observed at the edge of as-built samples, such as in Figure 4.7. This was not visible in electropolished or mechanically polished samples, due to the removal of material from the edge during these processes.

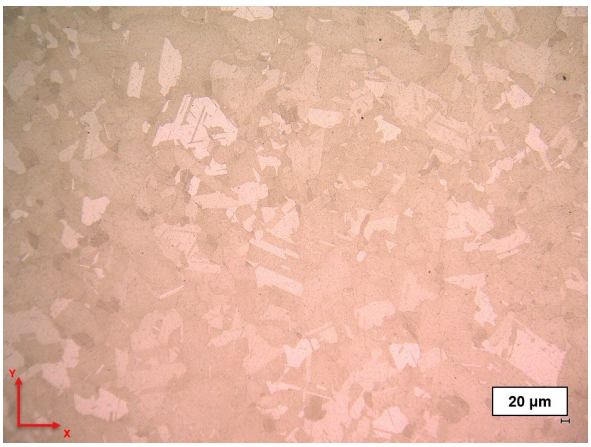

Figure 4.6: Optical micrograph of center of the sample (XY plane, 40/AB/V)

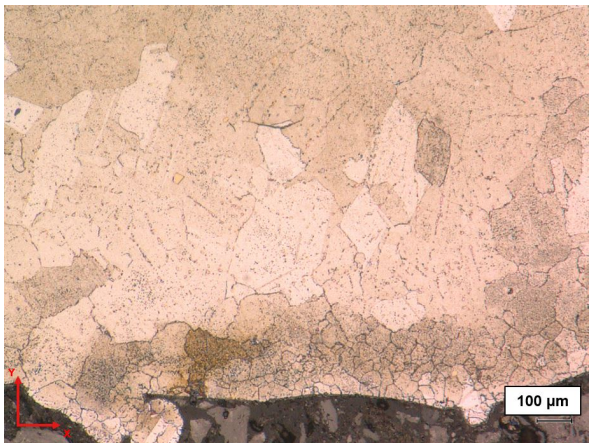

Figure 4.7: Optical micrograph of center of the sample (XY plane, 40/AB/V)

Phases

Carbides were identified widely in the microstructure of all sample groups. They were typically larger (1-2 µm) than other secondary phases identified and were globular in morphology. Figure 4.8 shows these carbides occurring both at the grain boundaries and within the grain and Figure 4.9 shows the EDS elemental point quantification, confirming high C and Nb. Carbides were identified throughout, at both the near surface and the bulk. In terms of fatigue behavior, carbides can be detrimental to fatigue performance. Larger carbides are a hard, stressed phase which can serve as an initiation point for fatigue cracking, particularly if located on the surface.

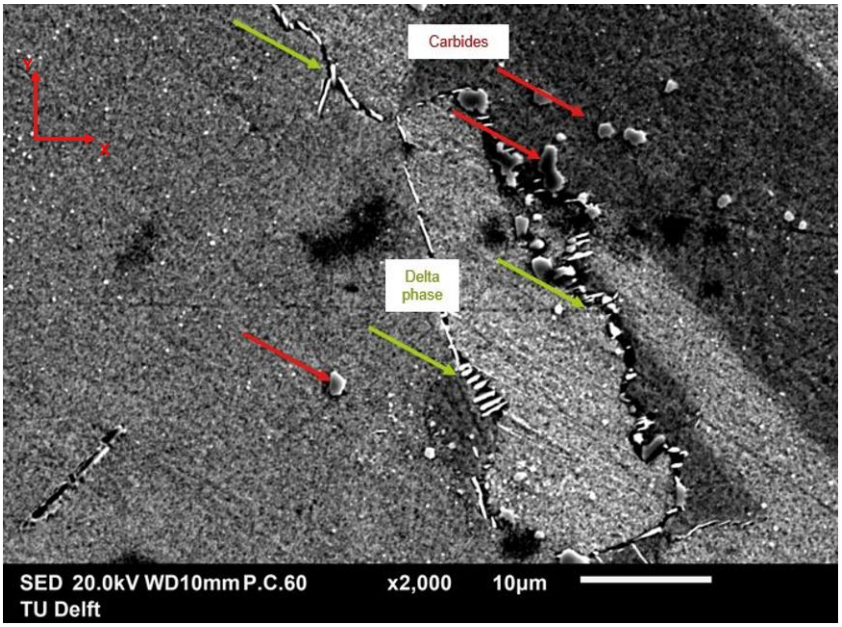

Figure 4.8: Backscattered electron image and EDS elemental quantification of δ phase

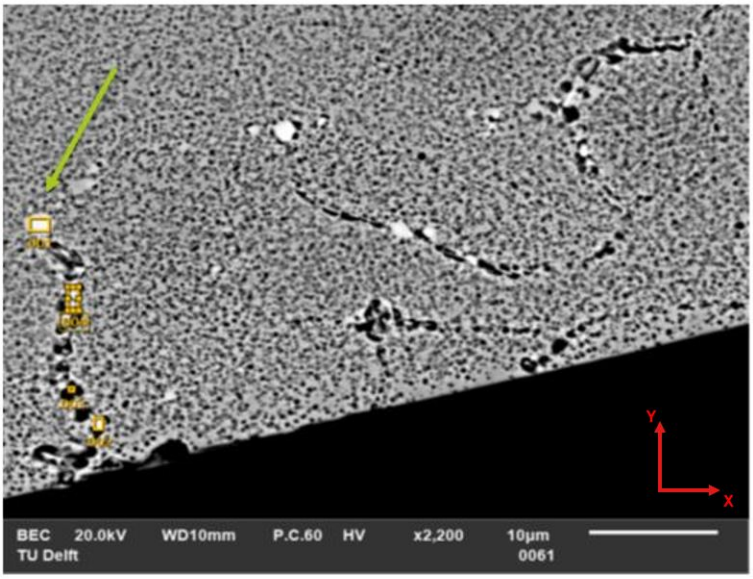

	Fe	O	Al	Ti	Cr	Mn	Ni	Nb	Mo
wt %	3.71	1.06	0.03	8.16	4.22	0.49	8.78	68.85	nd

Figure 4.9: Secondary electron image of carbides and of delta phase originating at the grain boundary

The carbides are concentrated at the grain boundaries. This is commonly observed in literature and is attributed to segregation of Nb (also Mo and Ti) during solidification. When carbides are formed due to the eutectic reaction of liquid to γ + NbC, carbides will nucleate preferentially at the grain boundaries as the free energy required for formation is lower than in the matrix [42]. During subsequent heat treatment, these grain boundary carbides serve to pin the grain boundaries and reduce grain boundary growth during nucleation. Nanoscale particles in the matrix are assumed to be γ' phases, but this is unconfirmed by SEM analysis due to their small size.

Evaluation of the XZ plane reveals some remnants of the columnar grain structure produced by SLM. Carbides in this plane were aligned in the build direction in the prior columnar grain boundary (Figure 4.10).

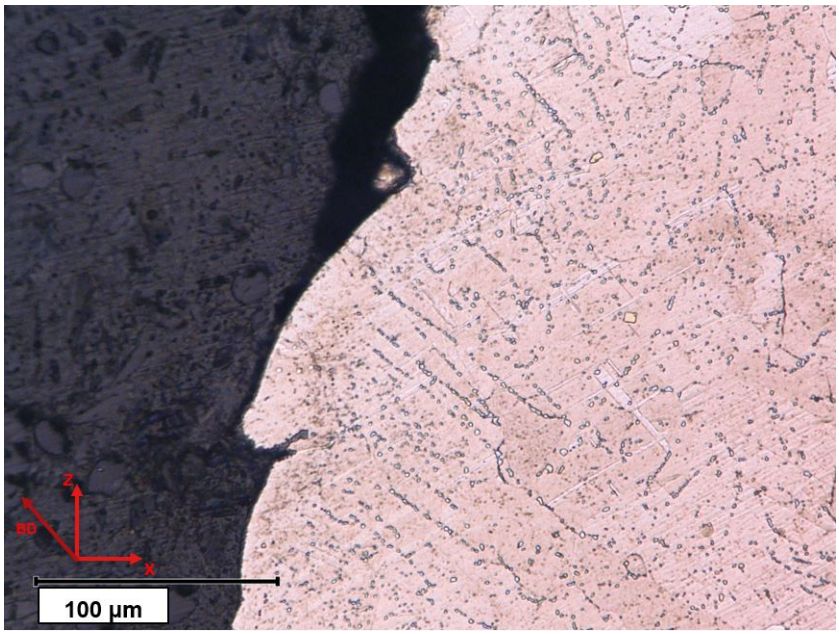

Figure 4.10: Micrograph of the XZ plane of 40 µm inclined sample, showing carbides aligned in build direction

Delta (δ) phases were identified primarily in the grain boundaries. They were characterized by parallel platelet-like precipitates and are known to have the composition Ni_3Nb. The δ phase along the grain boundary is seen in Figures 4.8 and 4.11. As with grain boundary carbides, δ phase decoration of the grain boundary restrains grain boundary migration during recrystallization. Gao et al. reports that this decoration of the grain boundaries embrittles the boundary, leaving it vulnerable to intergranular fracture during tensile loading [60]. In cyclic loading conditions, brittle phases at the grain boundaries provide more energetically favorable path for the crack to propagate along.

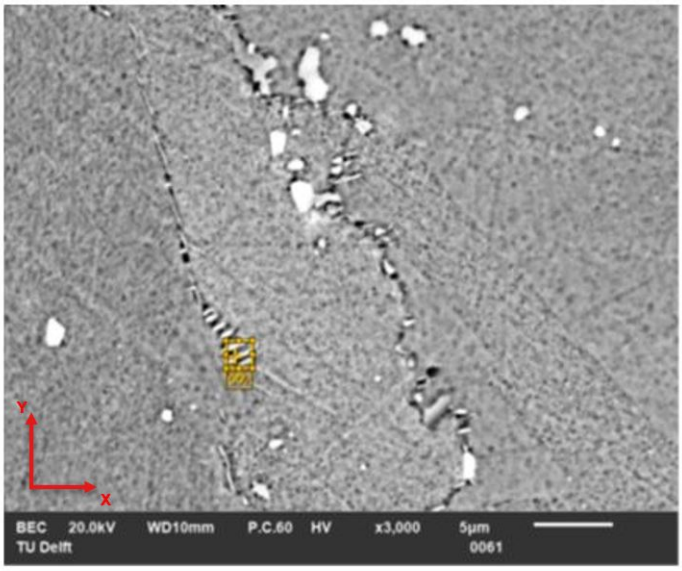

	Fe	Ti	Cr	Mn	Ni	Nb	Mo
wt %	18.03	1.15	17.8	0.25	56.1	5.22	2.13

Figure 4.11: Backscattered electron image and EDS elemental quantification of δ phase

The titanium nitride inclusions found in the feedstock powder were also present throughout the microstructure in all samples. These nitrides are not commonly observed in SLM Inconel 718. The TiN inclusions in the powder were as small as 1 µm and as large as 5 µm. However, inclusions in the printed material were for the most part large than 5 µm and could be as large as 18 µm in length, see Figure 4.12. They seemed to often agglomerate together, such as in Figure 4.13, and were cuboidal in shape. The increased size and agglomeration suggests that smaller TiN inclusions present in the powder clump together during the SLM process, resulting in larger TiN inclusions or concentrated areas of many TiN particles. Electron images of these precipitates and their EDS elemental composition are shown in Figure 4.14. In addition to Ti and N, the inclusions also contain elevated Nb, which could be detrimental in terms of depletion of Nb and preventing the formation of strengthening γ' and γ" phases.

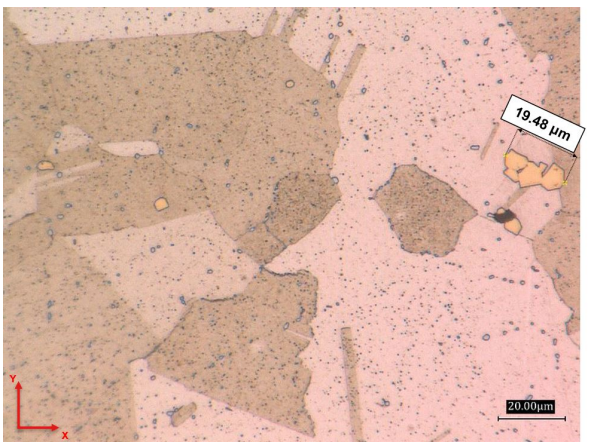

Figure 4.12: Large TiN agglomeration

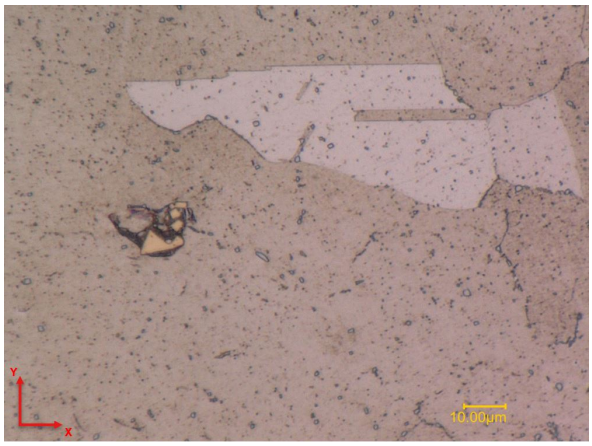

Figure 4.13: Agglomeration of TiN inclusions

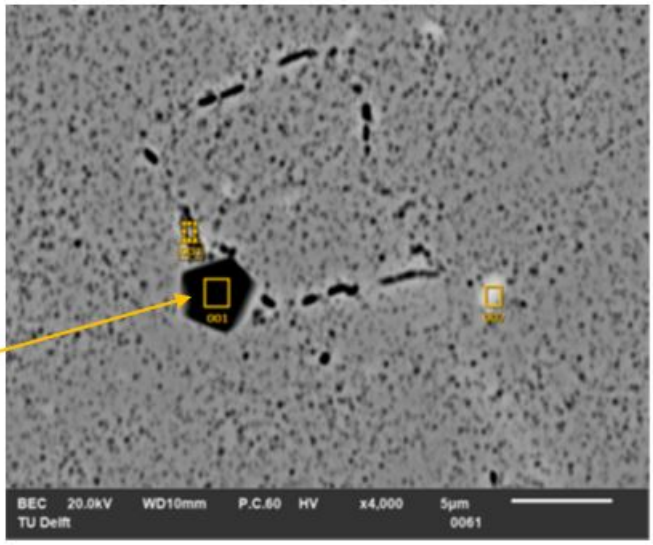

	Fe	O	C	N	Al	Ti	Cr	Mn	Ni	Nb	Mo
wt%	9.14	nd	nd	16.62	0.14	35.44	8.59	1.03	20.90	7.14	1.01

Figure 4.14: Backscatter electron image of TiN particle with EDS spectral quantification

The nitrides were often observed near pores or voiding - either lack of fusion or gas entrapment pores (Figure 4.15). These particles in the powder are not likely to melt in response to the laser (melting point of 2930 °C). Their presence may prevent flow of the molten material and could be a cause of lack of fusion voiding, as they would prevent fusion with the previous layer. In the case of gas entrapment porosity, these small pores might coalesce to form the larger circular shaped pores during the HIP process. This hypothesis is supported by the presence of TiN presence at large and small voids or pores. This phenomena could be attributed to nitrides, in a high enough concentration, preventing complete pore closure. Figures 4.15 and 4.16 show instances of a large concentration of TiN inclusions associated with cracks or incomplete closure of voids. Non-metallic inclusions such as TiN have very different elastic properties than the surrounding fcc metal matrix [61], causing localized strain. The apparent agglomeration of TiN inclusions can be attributed to drive toward the reduction of this strain by reducing TiN/matrix interfaces.

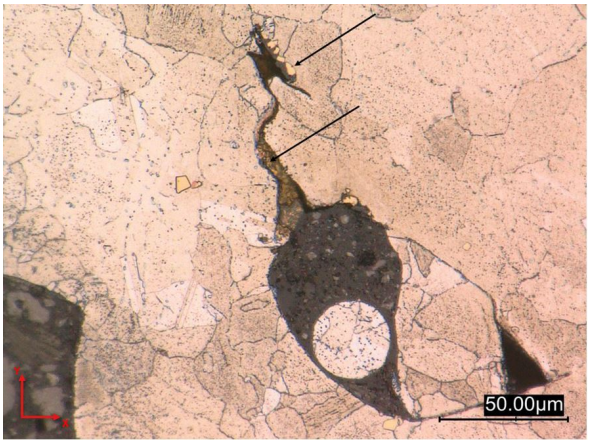

Figure 4.15: Optical micrograph showing concentration of titanium nitrides near lack of fusion pore

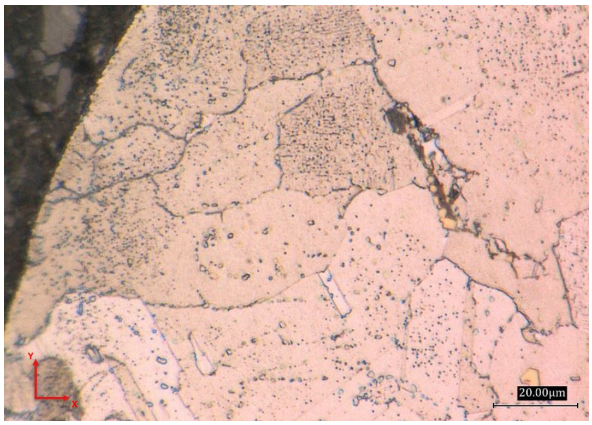

Figure 4.16: Optical micrograph of titanium nitrides in near-surface crack

The presence of these non-metallic inclusions presents multiple issues in response to cyclic loading. Texier et al. found TiN inclusions to be favorable sites for crack initiation under high cycle fatigue [61]. Titanium nitride is brittle, ceramic phase and therefore an additional source of stress in the microstructure. In addition, TiN is observed near lack of fusion pores located at the near surface (<100 µm deep), which serve as stress concentrators due to the notch effect. The formation of titanium nitride pulls Ti (and some Nb) from the surrounding matrix and reduces the formation of other strengthening phases (γ' and γ"). This locally has a negative impact on mechanical properties. In terms of corrosion resistance, reduced titanium in the matrix may impact the formation of titanium oxide passivating films at the surface.

Twins

Twins are widely observed in the microstructure of all sample groups. Generally speaking, twins are defined by two crystals in a grain mirrored around one plane. They can be easily identified by parallel lines within an apparent single grain, such as in Figure 4.17. Twins are formed commonly formed during the annealing process of fcc metal alloys. Qualitatively, no difference in the frequency of twins was observed between the sample groups.

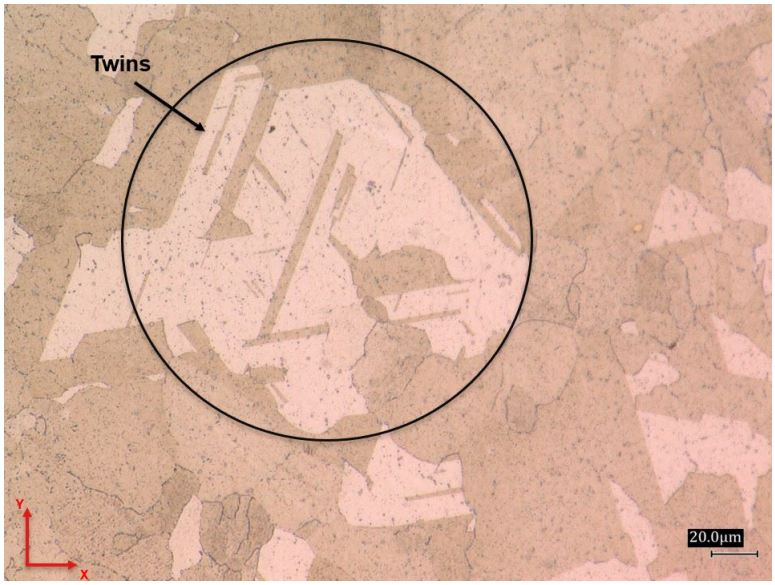

Figure 4.17: Optical micrograph of twins in a 40 µm layer thickness, electropolished, vertical sample

Twins appear as grain boundaries in a micrograph, but there are key differences between the two. Twin boundaries are two-dimensional defects and ordered, as they are a mirror plane between two ordered crystals. The stored energy of a grain boundary is much greater. Twin boundaries therefore are less susceptible to corrosion or preferential fracture than a typical high energy grain boundary [62].

The presence of twins in a microstructure can however have an impact on fatigue performance. Yeratapally et al. simulated fatigue crack initiation behavior in a nickel based superalloy populated with annealing twins. They found that fatigue crack preferentially initiated on the twin boundaries, conforming with literature observations [61, 63]. It must be noted that these simulations assume an ideal microstructure, relatively free of the defects common to SLM processing. A large lack of fusion void is certain to be a much greater concentrator of stress and a more likely location for crack initiation as compared to a twin boundary. However, these effects could be superimposed. The presence of twins near a large edge defect could increase stress at that location and increase the likelihood of crack initiation.

Surface

Following heat treatment, the materials gains a black appearance, which is seen in the as-built samples. SEM analysis of this layer reveals an oxide layer high in Al, Ti, Cr, and Nb that is approximately 1.6 µm thick (Figure 4.18).

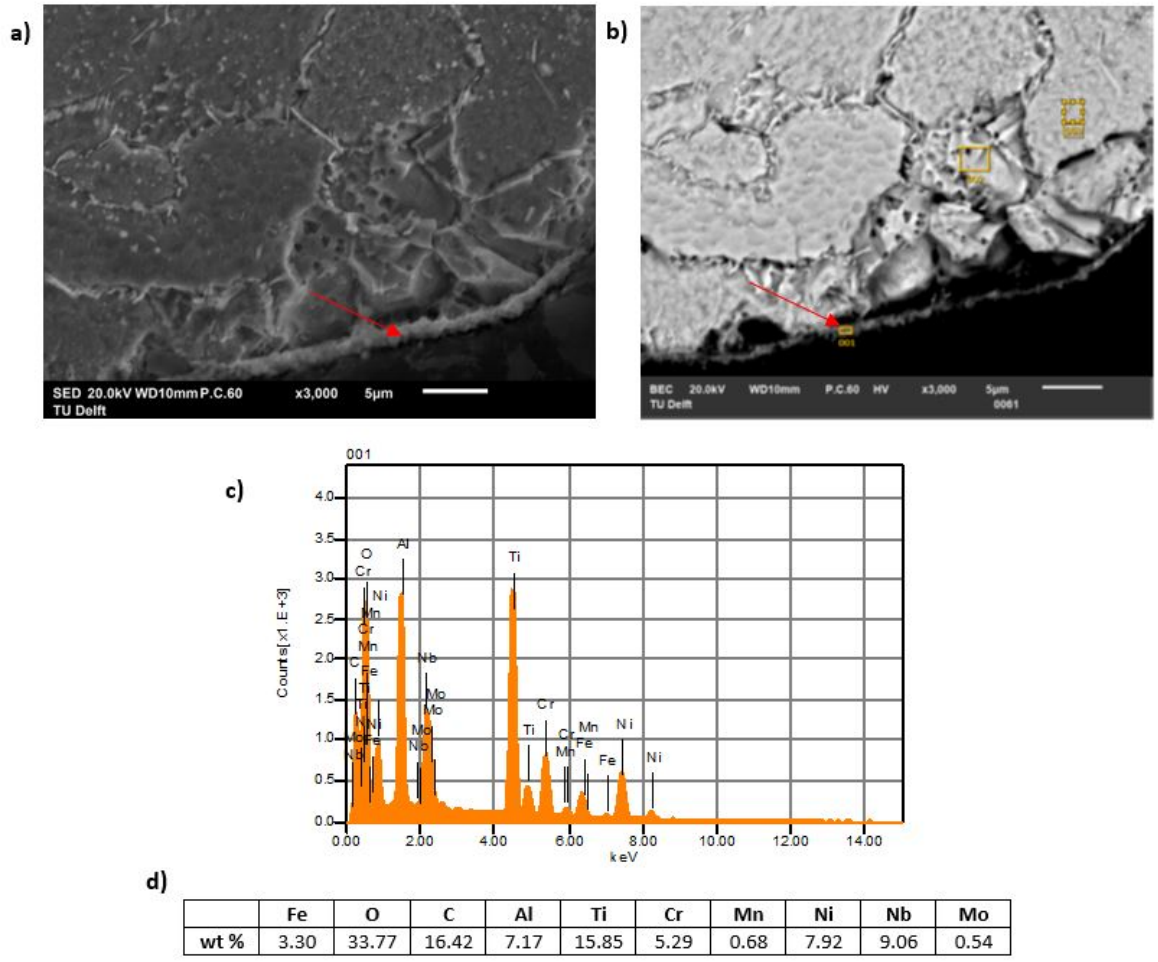

	Fe	O	C	Al	Ti	Cr	Mn	Ni	Nb	Mo
wt %	3.30	33.77	16.42	7.17	15.85	5.29	0.68	7.92	9.06	0.54

Figure 4.18: a) Secondary electron and b) backscattered electron images of surface oxide film, c) EDS spectra and d) elemental quantification

A number of the alloying elements of Inconel 718 may form oxides, including Cr, Ti, Al, Ni, and Fe. Ellingham diagrams are typically used to predict which oxides will form during a process. These diagrams show the Gibbs free energy of the oxide formation reactions at various temperatures. Oxidation reactions with lower energies of formation are more likely to occur [25]. The Ellingham diagram in Figure 4.19 shows this information for many of the possible oxides that could form when Inconel 718 is exposed to elevated temperatures. This prediction is idealized and does not account for the concentration of elements. An oxide can only form if there is sufficient supply of the element at the surface to interact with the O^{2-} anion. Therefore less energetically favorable oxides may form.

An extensive investigation of the oxidation layer was not performed as part of this study; however, the observed elements in the oxide layer are consistent with literature findings. Sadeghi et al. studied [64] the oxide layer formed on AM Inconel 718 following HIP and heat treatment at 850 °. The results indicated that growth of this oxide scale was diffusion controlled based on parabolic growth behavior. The resulting oxide layer was a protective Cr_2O_3 layer, with additional Fe_2O_3, $NiCr_2O_4$ and $FeTiO_3$ oxides. The process is diffusion controlled, so the formation of the chromia oxide is limited by the supply of Cr at the surface. The high titanium observed in Figure 4.18 can be attributed to the relatively high diffusion coefficient of Ti in comparison to other alloying elements.

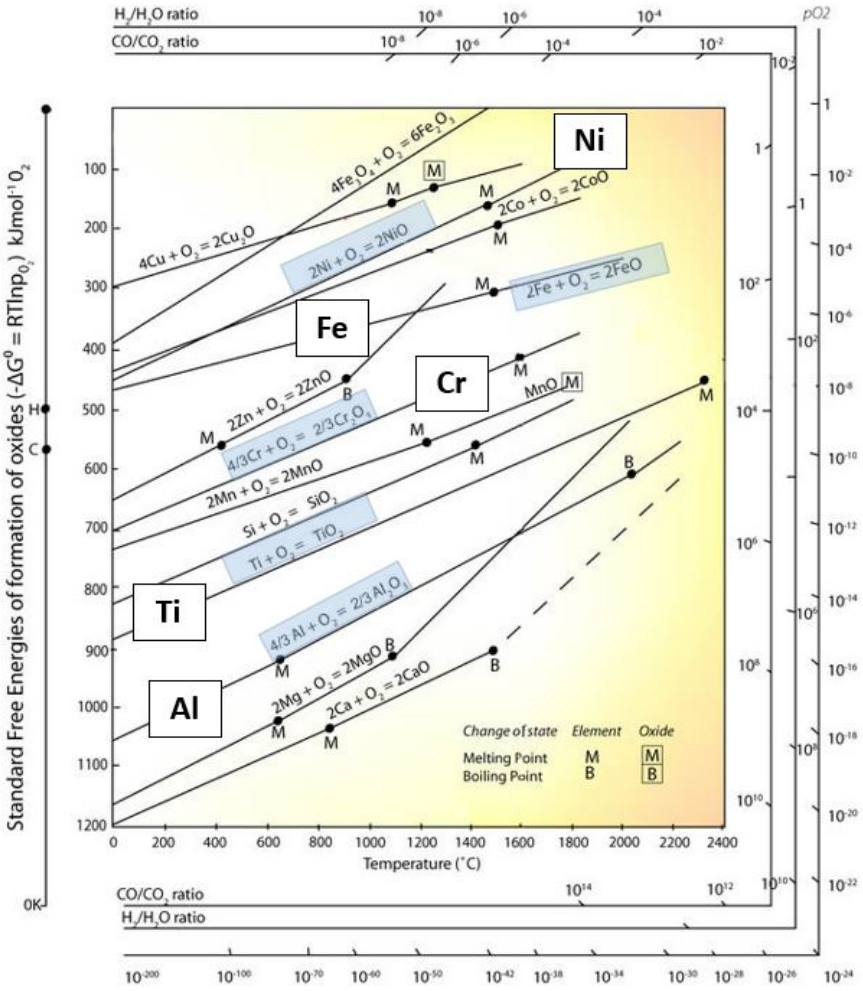

Figure 4.19: Ellingham diagram depicting the standard Gibbs energies of formation of oxides [25]

In this case, the oxide layer was most likely formed during the solution annealing and age hardening treatments detailed in Section 3.1, which take place between 620 and 980 degrees Celsius. At this temperature range the oxidation of Ti and Al has the lowest energy of formation and therefore the relative stability of Ti and Al oxide is higher than the oxides of Fe, Ni, and Cr. This does not mean that it is impossible for Fe, Ni, or Cr oxides to form, but that their formation is less likely compared to Al or Ti oxide.

4.1.3. XRD Phase Identification

Printed Material

XRD analysis was performed on 40 µm, electropolished, inclined built samples. The resulting spectra was consistent with an fcc matrix. Additional phases identified were NbC and $NbNi_3$.

Peaks corresponding to TiN were not identified. As the presence of TiN was confirmed through optical and SEM microscopy, it can be concluded that the TiN presence in the material is not high enough for peaks to register on the XRD spectra.

Powder

Analysis of the feedstock powder found an fcc matrix. Other phases present in a lower concentration include $MoFe_2$ (or the similar crystal structure $Nb_{0.8}Co_2Al_{0.2}$) and $Cr_{0.27}Fe_{0.47}Ni_{0.26}$.

NbC or $NbNi_3$ phases were not identified, confirming that these phases form during the SLM and subsequent heat treatment processes. TiN was also not identified, but was confirmed to be present via optical and SEM microscopy. Again, the concentration of TiN is likely too low to be detected with this analysis. XRD spectra of the powder and printed material can be found in Appendix C.

4.1.4. Hardness

Core Hardness

Bulk hardness of each sample group was measured in the center of XY and XZ planes. The results are shown in Table 4.1 and in box and whisker plots in Figures 4.20 and 4.21. The difference in hardness between XY and XZ planes was not statistically significant. It can therefore be concluded that the HIP procedure greatly reduced or eliminated the anisotropy typical of an as-processed additively manufactured microstructure. The results also do not show a clear relationship between hardness and build direction or layer thickness or significant differences between these groups. Build direction does not appear to affect the microstructure or the phases precipitated at a significant level to have an effect on the core hardness. This can be expected, as the thermal history of the core is not very different between inclined and vertical samples, as in both cases the layers are built on top of pre-existing (heated) layers and therefore experience comparable subsequent thermal cycling.

Table 4.1: Core hardness (HV1)

	80 µm/Vertical	**80 µm/Inclined**	**40 µm/Vertical**	**40 µm/Inclined**
XY	387.6 ± 7.6	388.6 ± 8.3	381.8 ± 5.6	391.2 ± 5.6
XZ	390.7 ± 7.2	386.1 ± 6.6	388.2 ± 6.9	388.2 ± 8.1

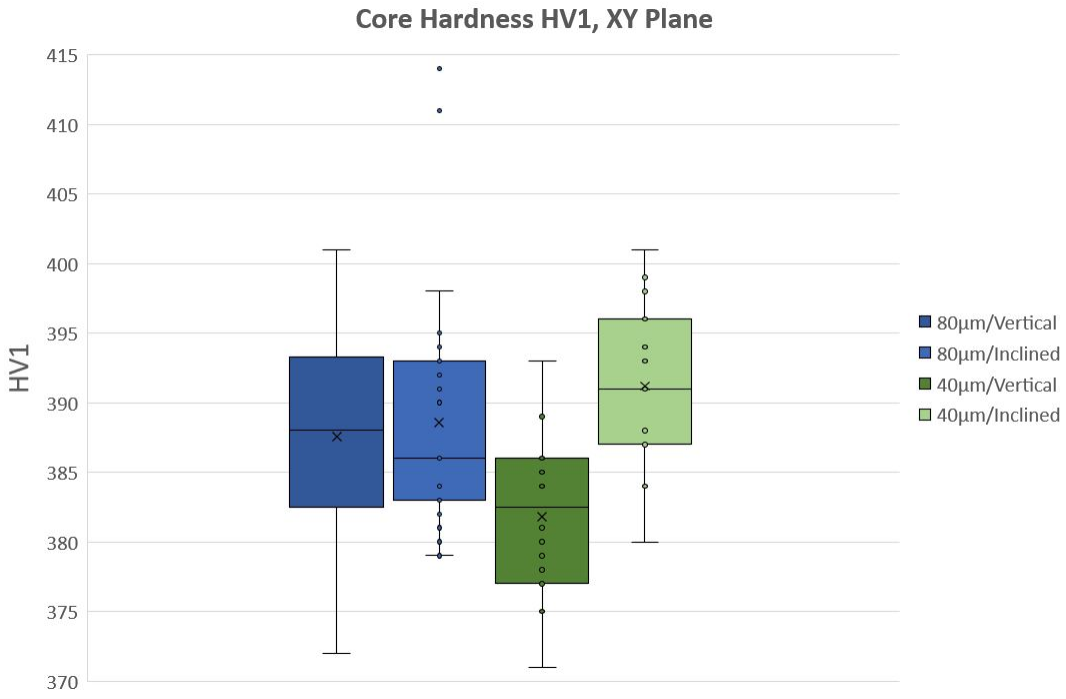

Figure 4.20: Box and whisker plot of core hardness in the XY plane

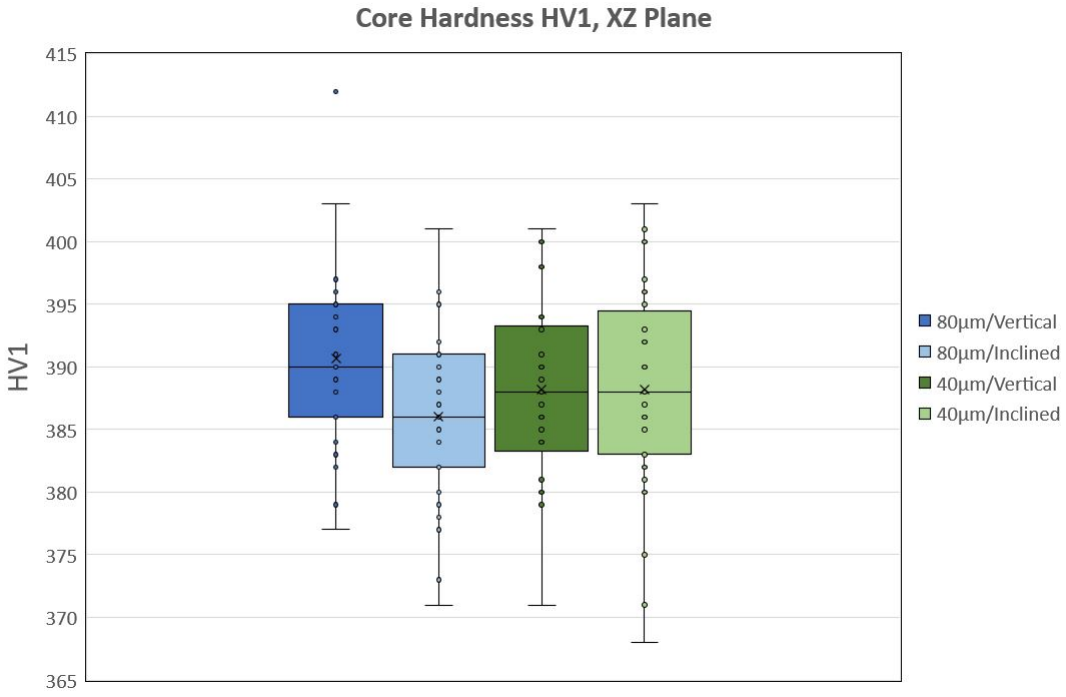

Figure 4.21: Box and whisker plot of core hardness in the XZ plane

These results correspond with what was observed in the microstructural investigation. Minimal aniosotropy was observed between XY and XZ planes, barring the alignment of carbides along the previous columnar grain boundaries. While the formation of carbides has the effect of pulling Nb, Ti and other strengthening elements from the matrix leading to a lesser amount of strengthening γ' and γ" phases, the distribution of these carbides does not appear to have a significant impact on hardness. It is possible that locally hardness decreases, but this is not detected when evaluating HV1 hardness with 1 kgf.

Near-Surface Hardness

As the results of core hardness measurements showed no significant difference in hardness between XY and XZ planes, near-surface hardness was measured on the XY plane only. The results of this investigation are shown in Table 4.2.

Table 4.2: Near surface hardness (HV1)

80/AB/V	**80/AB/I**		**80/EP/V**	**80/EP/I**		**80/P/V**	**80/P/I**
	Upskin	*Downskin*		*Upskin*	*Downskin*		
378 ± 11.2	386 ± 5.96	440 ± 39.7	386 ± 7.15	381 ± 7.76	425 ± 15.1	390 ± 5.16	379 ± 8.12
40/AB/V	**40/AB/I**		**40/EP/V**	**40/EP/I**		**40/P/V**	**40/P/I**
	Upskin	*Downskin*		*Upskin*	*Downskin*		
388 ± 3.67	389 ± 7.76	380 ± 7.39	382 ± 7.99	376 ± 3.12	389 ± 9.88	376 ± 13.0	387 ± 6.45

The near-surface hardness of vertical samples was comparable to bulk hardness. A hardness difference between the upskin and downskin sides of the inclined 80 µm samples is evident and is confirmed through statistical analysis found in Table 4.3. The table shows the results of ANOVA variance analysis and subsequent Fisher individual tests for least significant difference, which determines if the difference between two sample groups is statistically significant or not (see Section 3.2). If the null hypothesis is rejected then the two compared groups can be said to be statistically distinct in the 95% confidence interval.

Table 4.3: Fisher individual test comparing near surface hardness, p = 0.95

Compared groups	**LSD**		**Difference in means (abs)**	**Null hypothesis?**
80/AB us vs. 80/AB ds	15.3809	<	53.87	Reject
80/EP us vs. 80/EP ds	16.0648	<	43.80	Reject
40/AB us vs. 40/AB ds	15.3809	>	9.73	Accept
40/EP us vs. 40/EP ds	15.3809	>	12.47	Accept
80/AB/V vs. 80/P/V	13.5206	>	11.85	Accept

It can be concluded that the downskin side of inclined, 80 µm layer thickness samples is statistically harder than the upskin side. This is not the case with 40 µm layer thickness samples, which exhibit no statistical difference. As discussed in Chapter 2, increasing the layer thickness results in lower transferred energy density (assuming all other inputs remain constant). The increased thickness also reduces the subsequent thermal cycling experienced due to additional layers printed on top. Similarly, the upskin side of a sample built at an incline does not benefit from subsequent cycles, while the downskin side does. All this contributes to a different thermal history between upskin and downskin near-surface, and therefore a possibility of variance in phases formed. This was explored further with microstructural investigation. Hardness differences in SLM material can also be due to differences in porosity. The HIP treatment however makes this possibility unlikely.

Figure 4.22 shows near surface microstructure of both upskin and downskin sides. There is an apparent increase in carbides on the upskin side. As previously discussed, the formation of carbides removes Nb from the surrounding matrix and limits the formation of hardening γ' and γ" phases. A likely explanation for the observed difference in hardness is a difference in carbide formation.

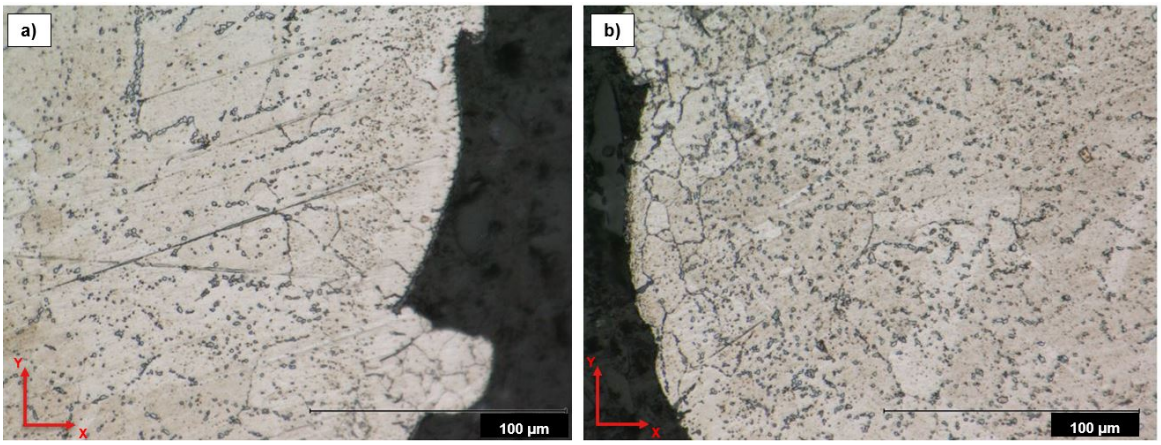

Figure 4.22: Micrographs of (left) downskin and (right) upskin near surface (40 µm, as-built)

4.1.5. Density

The density relative to a wrought reference specimen for each sample group is displayed in Figure 4.23 and Table 4.4. The average apparent density of all samples groups is 99.6%. It can therefore be concluded that the standard process - SLM, followed by heat treatment and HIP - produces a dense, relatively defect-free product comparable to literature results.

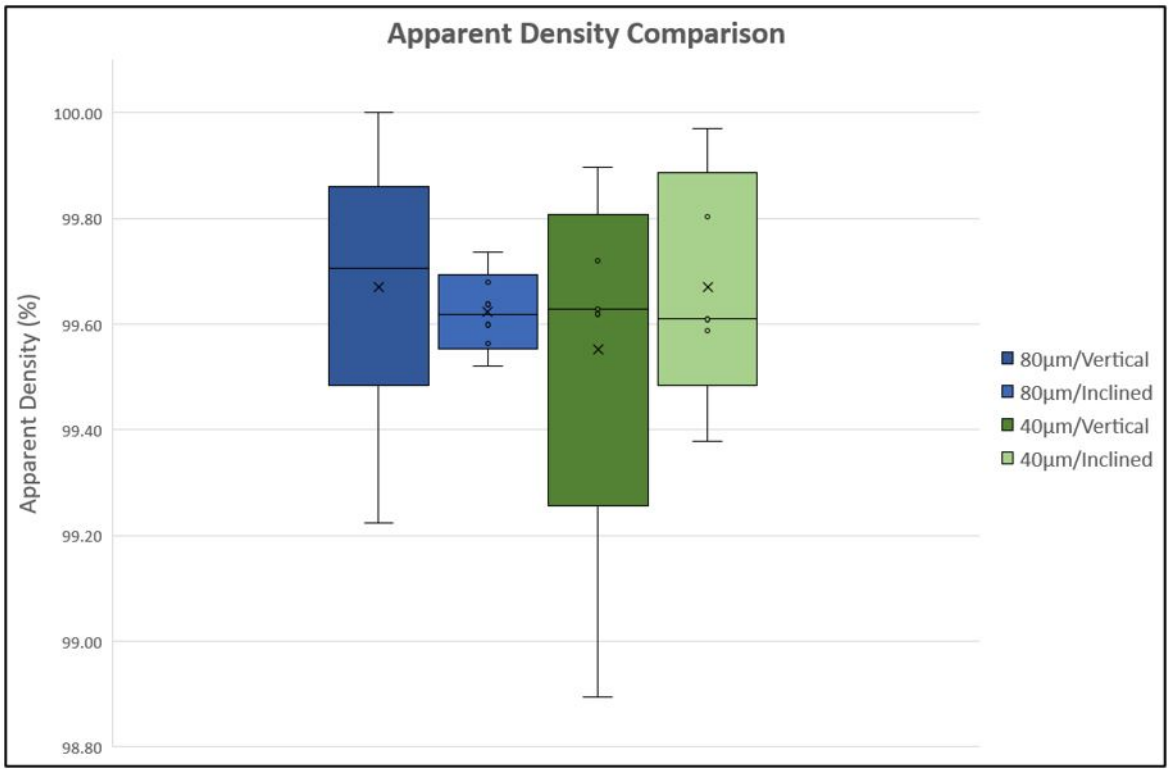

Figure 4.23: Box and whisker plot representation of apparent density

Table 4.4: Apparent density (%) of SLM Inconel 718

80 µm/Vertical	80 µm/Inclined	40 µm/Vertical	40 µm/Inclined
99.67 ±0.238	99.62 ±0.072	99.55 ±0.344	99.67 ±0.202

The results show no significant difference in density between 80 and 40 µm layer thickness or between vertical and inclined build directions. There is a relatively large spread in density values within the most sample groups. As this spread is fairly consistent in all sample groups (although less so in 80 µm inclined samples), it is a likely result of inherent variability in the SLM process producing inconsistent voids and porosity and not the result of a specific process difference.

It is important to note that density was measured only on sample groups mechanically polished in post-processing, which, as stated previously, removes a significant amount of material from the near surface. The process would be enough to remove lack of fusion porosity found at the near surface in other sample groups. Therefore, the measured density is reflective of the bulk density. The density of as-built and electropolished sample groups would very likely be lower due to lack of fusion porosity.

4.2. Process Induced Defects

4.2.1. Porosity

Different types of porosity were found in the microstructure, including lack of fusion porosity and gas entrapment porosity. As discussed in Chapter 2, lack of fusion porosity is characterized by large (>50 µm) voids and are formed as a result of energy input at an insufficient level to fully melt the powder particles or from spattering of the molten metal at high energy densities. Lack of fusion pores were identified in as-built and electropolished sample groups of both layer thicknesses and were found as far as 150 µm from the surface, see Figure 4.24.

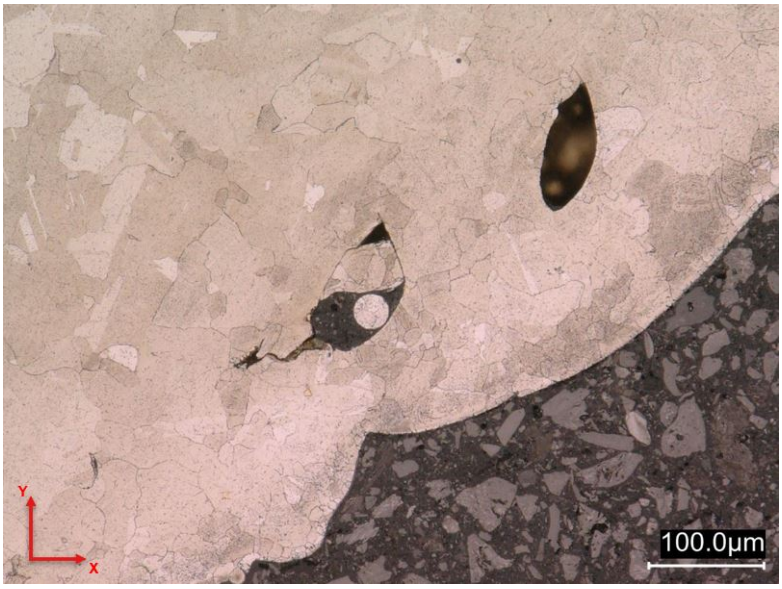

Figure 4.24: Lack of fusion porosity at the near surface of an 80 µm, vertical, as-built surface condition sample

Lack of fusion pores were not found in the samples which underwent mechanical polishing surface treatment. This can be attributed to the material removed during the polishing process, as the pores are isolated to the near-surface. HIP post-processing treatment is a typical method to reduce porosity in SLM components, but in this case was not successful in removing these pores. The reason for this is likely the large size of the pores, as well as their proximity to the edge. The HIP process uses high pressure to close the pores, which requires surrounding material to press on the pore in order to reduce its size. As these pores are located at the near surface, there is less surrounding material to apply pressure. Additionally, these pores are more likely to occur at the edge, as the material at the edge experiences lower energy input and fewer thermal cycles than the bulk. This may lead to incomplete fusion at the edge. There is however evidence that these pores were not limited to the near-surface in the as-processed condition. Figure 4.25 shows long, thin voids in the center of a sample that could potentially have began as large lack of fusion voids that were subsequently closed by HIP.

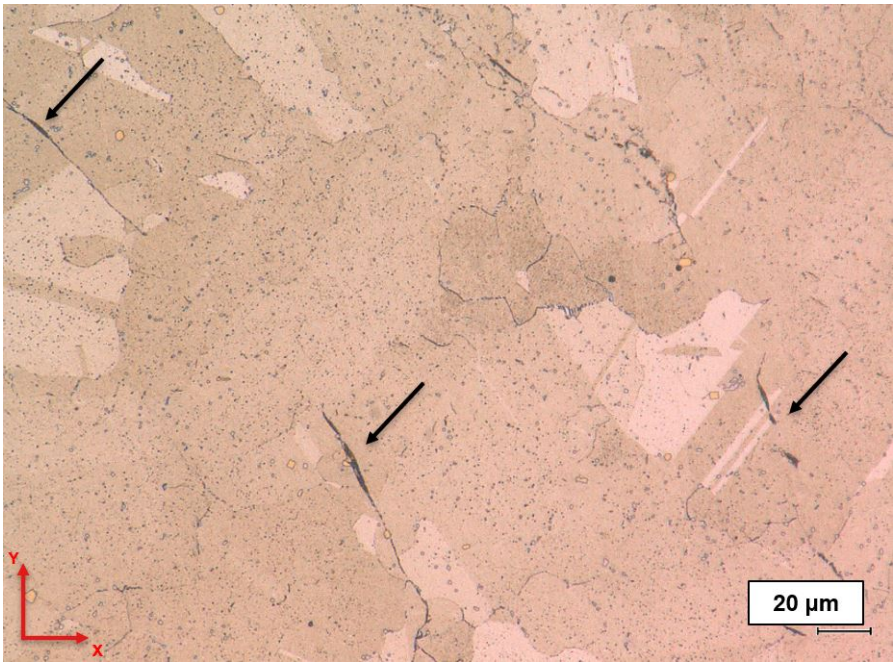

Figure 4.25: Possible prior lack of fusion pores closed by HIP in the center of a 40 µm, vertical, as-built surface condition sample

Smaller, cylindrical pores were identified in the microstructure of both layer thicknesses. In contrast to lack of fusion pores, these smaller pores were located in the bulk as well. The density of these pores in the bulk can be observed in Figure 4.26, which shows pores that are fairly sporadic and small in size. Typical dimensions of one of these pores is shown in Figure 4.27, measuring 6.5 µm in diameter. These pores as identified as gas entrapment porosity, a typically occurring phenomena in the SLM process. The size and morphology of these entrapment pores are very similar to those found by Moussaoui et al. following a similar heat treatment protocol [44].

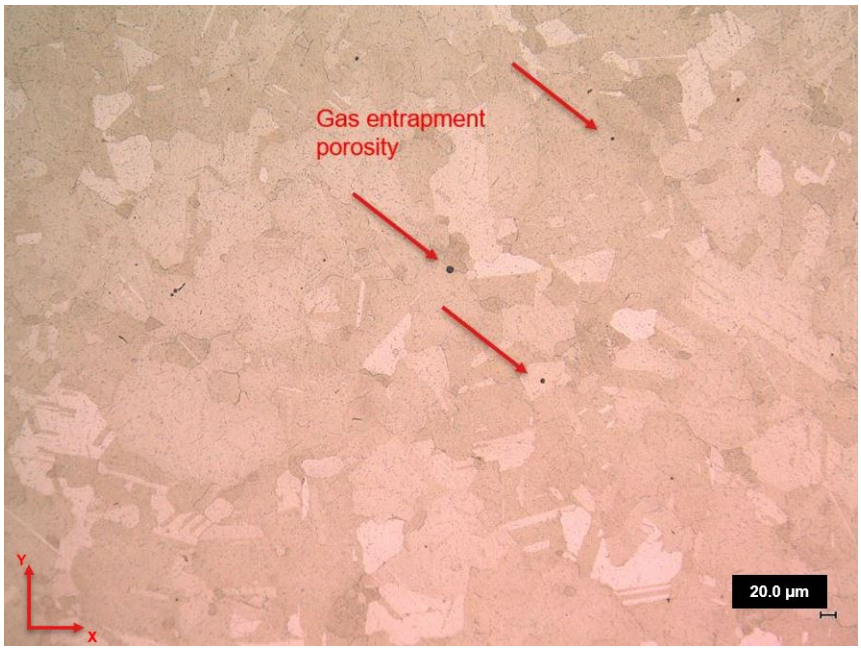

Figure 4.26: Micrograph showing the distribution of pores in 40 µm, vertically built sample

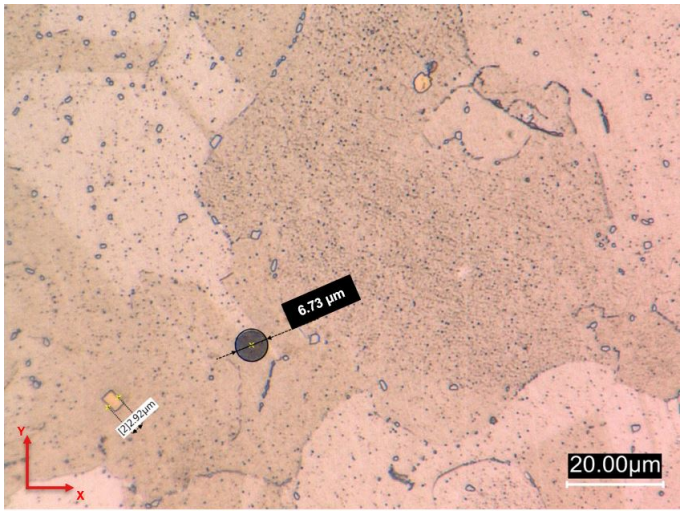

Figure 4.27: Typical size of entrapment porosity

These pores are not significant enough in number or size to play much of a role in the fatigue behavior of SLM Inconel 718. The identified lack of fusion pores are both much larger than these and located at the near surface, making them likely spots for fatigue crack initiation.

4.2.2. Surface Roughness

Laser Interferometer Results

Table 4.5 displays the results of surface roughness as measured by the Brucker interferometer. See Appendix A for representative 3D topographical images of each sample group.

Table 4.5: Surface roughness R_a as determined by laser interferometry

80/AB/V	**80/AB/I**		**80/EP/V**	**80/EP/I**		**80/P/V**	**80/P/I**
	Upskin	*Downskin*		*Upskin*	*Downskin*		
14.5 ± 1.1 µm	18.4 ± 6.0 µm	39.1 ± 4.3 µm	13.7 ± 2.7 µm	12.3 ± 4.0 µm	10.2 ± 2.4 µm	0.33 ± 0.06 µm	0.33 ± 0.15 µm
40/AB/V	**40/AB/I**		**40/EP/V**	**40/EP/I**		**40/P/V**	**40/P/I**
	Upskin	*Downskin*		*Upskin*	*Downskin*		
11.7 ± 1.0 µm	18.7 ± 2.1 µm	19.5 ± 4.8 µm	6.2 ± 1.5 µm	28.2 ± 7.8 µm	20.4 ± 6.8 µm	0.40 ± 0.03 µm	0.38 ± 0.01 µm

Larger layer thickness results in higher surface roughness for both as-built and electropolished sample groups and this difference is statistically significant for the electropolished, vertically built condition, as shown in Table 4.6. As before, the results show a dramatic improvement in surface roughness following mechanical polishing. The effect of electropolishing on roughness is much less dramatic, in particular for 80 µm layer thickness. In the case of both thicknesses there is a reduction in roughness, but the reduction is only statistically significant for the 40 µm layer thickness groups. This difference could be owing to the different contributions to roughness. These are larger ridges, about the width of one layer thickness, and smaller spattering or partially melted particles. These features are visible in the topographical surface in Figure 4.28. These smaller spatter or particles potentially have a lesser contribution to surface roughness compared to the larger surface features; therefore, removal of the spatter by electropolishing would have a marginal reduction in roughness. It is apparent visually that electropolishing removes these spatter particles but retains the larger features, as can be seen in Figure 3.3. The larger peaks and valleys would be smaller in the case of 40 µm layer thickness samples and could contribute comparatively less to overall surface roughness, leading to a more significant roughness reduction following electropolishing and the removal of spatter.

The results indicate that the level of electropolishing performed (meaning the amount of material removed) does not sufficiently reduce surface roughness. The method is therefore less likely to improve fatigue performance as compared to the as-built surface condition.

Table 4.6: Fischer individual test comparing surface roughness of vertical sample groups

Compared groups	LSD		Difference in means (abs)	
80/AB/V vs. 40/AB/V	5.137169	>	2.8352	Accept
80/EP/V vs. 40/EP/V	4.918464	<	7.537133	Reject
80/AB/V vs. 80/EP/V	5.137169	>	0.7962	Accept
40/AB/V vs. 40/EP/V	4.918464	<	5.498133	Reject

The results for inclined samples are also consistent with that of the white light interferometry. Samples with the as-built surface condition exhibit higher roughness on the downskin side, as expected; however, the difference is statistically significant only in the case of 80 µm inclined samples (Table 4.7. Electropolished samples of either layer thickness did not show the same trend toward increased downskin side roughness.

Table 4.7: Fischer individual tests for upskin vs. downskin surface roughness

Compared groups	LSD		Difference in means (abs)	
80/AB/I us vs. 80/AB/I ds	5.44879	<	20.6641	Reject
40/AB/I us vs. 40/AB/I ds	4.689572	>	0.7875	Accept
80/EP/I us vs. 80/EP/I ds	5.743529	>	2.1085	Accept
40/EP/I us vs. 40/EP/I ds	5.137169	>	2.2752	Accept

The results of the laser interferometer compared to the Keyence light interferometer method are quite similar. Some differences can be attributed to the method used, as the light interferometer measured roughness of a relatively small number of lines ($\tilde{1}2$) that were then averaged, while the laser method measures a whole surface. It is apparent from the 3D image of the surface and the X and Y line profile that roughness is greater in the X direction (along the length of the sample) than in the Y, owing to the peaks and valleys formed as the layers build up. The Keyence method only measured roughness along the X direction and the Brucker method uses both direction in its R_a calculation, therefore some differences in R_a are to be expected.

Optical Interferometry Results

The results of surface roughness measurements using the Keyence microscope (white light interferometery) approach are shown in Table 4.8. There is clear improvement in surface roughness following mechanical polishing and not much distinction between R_a between the polished sample groups. The improvement in surface roughness provided by electropolishing is apparently minimal, with 40 µm layer thickness electropolished samples exhibiting higher roughness than their as-built counterparts. The inclined built samples in all cases exhibit increased surface roughness as compared to vertical built samples.

There is some indication that increased layer thickness results in increased surface roughness, based on comparison of the as-built and electropolished vertical samples of both thicknesses. However, the difference is not distinct enough to make this assertion. Overall this measurement technique results in high standard deviation, which limits interpretation.

Table 4.8: Surface roughness R_a as determined by light interferometry

80/AB/V	**80/AB/I**		**80/EP/V**	**80/EP/I**		**80/P/V**	**80/P/I**
	Upskin	*Downskin*		*Upskin*	*Downskin*		
14.3 ± 6.7 µm	20.6 ± 4.9 µm	30.6 ± 10.8 µm	11.4 ± 5.3 µm	14.7 ± 6.4 µm	21.01 ± 4.2 µm	2.6 ± 0.8 µm	2.3 ± 0.7 µm
40/AB/V	**40/AB/I**		**40/EP/V**	**40/EP/I**		**40/P/V**	**40/P/I**
	Upskin	*Downskin*		*Upskin*	*Downskin*		
11.2 ± 3.4 µm	15.7 ± 5.7 µm	13.6 ± 3.5 µm	8.8 ± 3.4 µm	27.3 ± 15.8 µm	21.4 ± 12.0 µm	2.3 ± 0.8 µm	4.7 ± 1.0 µm

Upon inspection of the 3D surface profile generated by the microscope (from Figure 3.7), it was clear that this method is not capable of capturing roughness caused by partially melted particles at the surface. It appears to be capable of capturing general roughness as a result of the melt pattern.

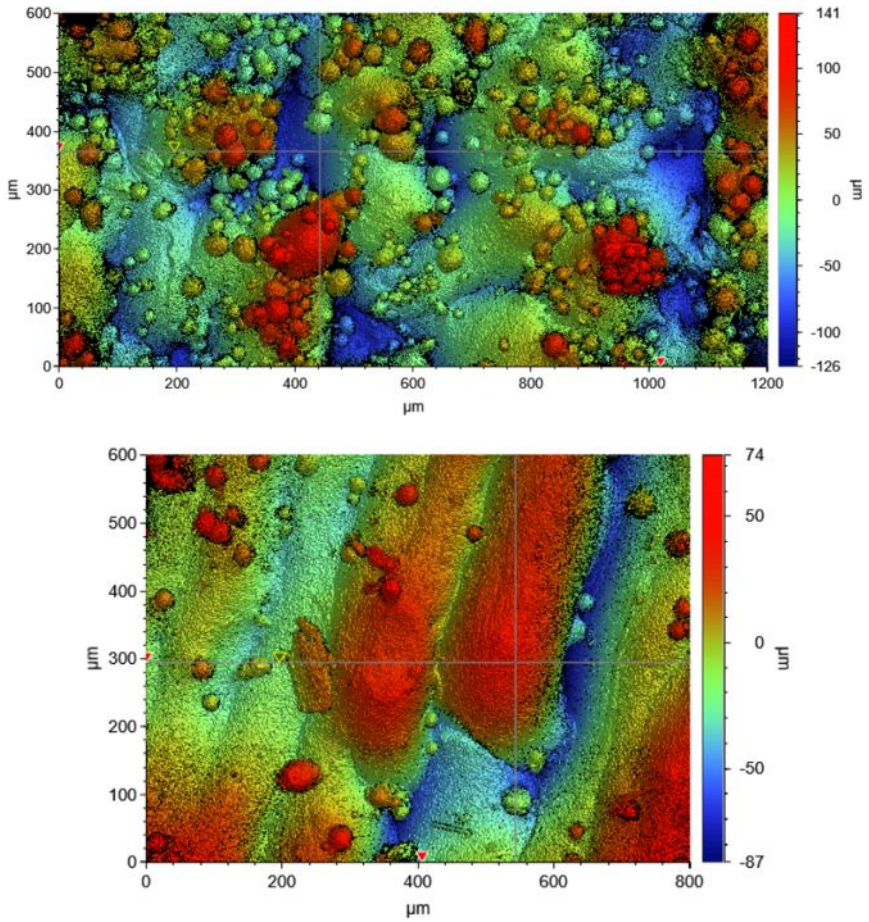

Figure 4.28: 3D views of the upskin (top) and downskin (bottom) surfaces of an 80 µm as-built sample, showing greater incidence of partially melted particles on the downskin side

However, the analysis of the fracture surfaces indicates that fatigue cracks initiate at larger notches at the surface and therefore these partially melted particles may not be of significant size to contributed to crack initiation. In this case, the relatively simple technique of light interferometry could be sufficient in recognizing large notches which may cause fatigue failure. This is a non-destructive method which could be used during quality evaluations.

Incline Built Side Comparison

Figure 4.29 and 4.30 show an optical comparison of the upskin and downskin side of a 80 µm layer thickness specimen. A greater amount of partially melted powder particles can be seen on the downskin side, consistent with literature.

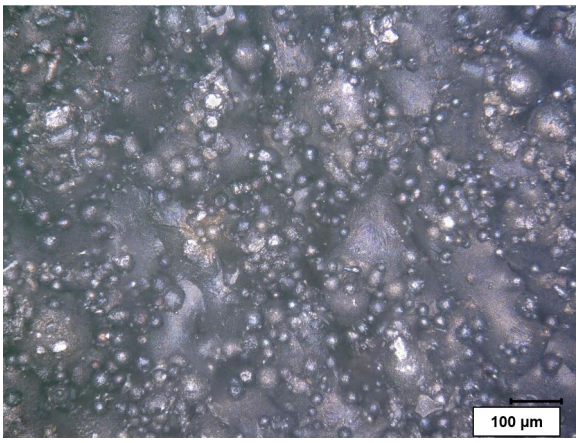

Figure 4.29: Optical images 80 µm downskin as-built surface

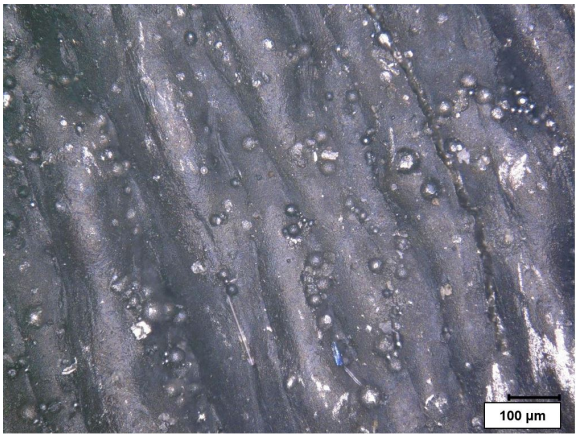

Figure 4.30: Optical images 80 µm upskin as-built surface

In the case of Inconel 718 built on an incline, it is clear that upskin vs. downskin sides plays a significant role in the resulting properties. There is an apparent distinction in hardness and surface roughness between sides for 80 µm layer thickness sample groups. This difference is not however seen to same degree in 40 µm layer thickness samples. In the case of surface roughness this can be attributed to the much greater occurrence (from a visual perspective) or particles during the process due to spattering or insufficient heat input to fully melt them. Examination of the roughness data for electropolished samples of the same layer thickness provides additional evidence. After electropolishing and the removal of these particles, the roughness is not significantly different between upskin and downskin.

The proclivity for partially melted particles to attach on the downskin side has been reported previously in literature [65]. The difference is attributed to the different thermal history of each side. The downskin side of an inclined surface is printed directly onto the powder bed, which dissipates heat at a slower rate than previously printed layer. This causes the melt pool formed to be large and to extend into the powder bed below, due to both gravity and capillary action. This larger melt pool attaches more partially melted particles, causing the increase in roughness. This edge phenomena could be more controlled through use of different laser process parameters for overhangs and inclined surfaces.

The difference in hardness is driven by a difference in microstructure. The microstructure of an SLM processed alloy is highly dependent on the thermal history, which would differ between upskin and downskin sides. In a normal vertical build each layer is built directly on top of the previous and the energy transferred by the laser will provide some heat to the layers beneath. As mentioned in Chapter 2, this can serve to partially relieve residual stress caused by the rapid cooling.

5

Results and Discussion - Fatigue

5.1. Fatigue Experimental Results

The limited number of samples per sample group and the lack of repetitions at a given stress level limit the analysis of the fatigue data. The results can however be analyzed for general trends between the surface finishes and the two different layer thicknesses. It is known in literature that defects expected as a result of the SLM process have a significant impact on the fatigue behavior and these defects and their locations often do not follow a regular pattern. For this reason high scatter in the results is expected.

Some clear trends with regards to post processing can be observed by the 80 µm layer thickness samples, the data of which can be seen in Figure 5.1. Mechanical polishing results in a clear improvement in fatigue performance. The improvement is less clear between as-built and electropolished sample groups. The limited number of samples makes it difficult to draw strong conclusions from the results. In the case of as-built and electropolished sample groups there is a slight trend towards higher cycles for vertical samples compared to inclined. This trend is the reverse in the case of polished samples, with inclined sample groups trending toward higher cycles to failure.

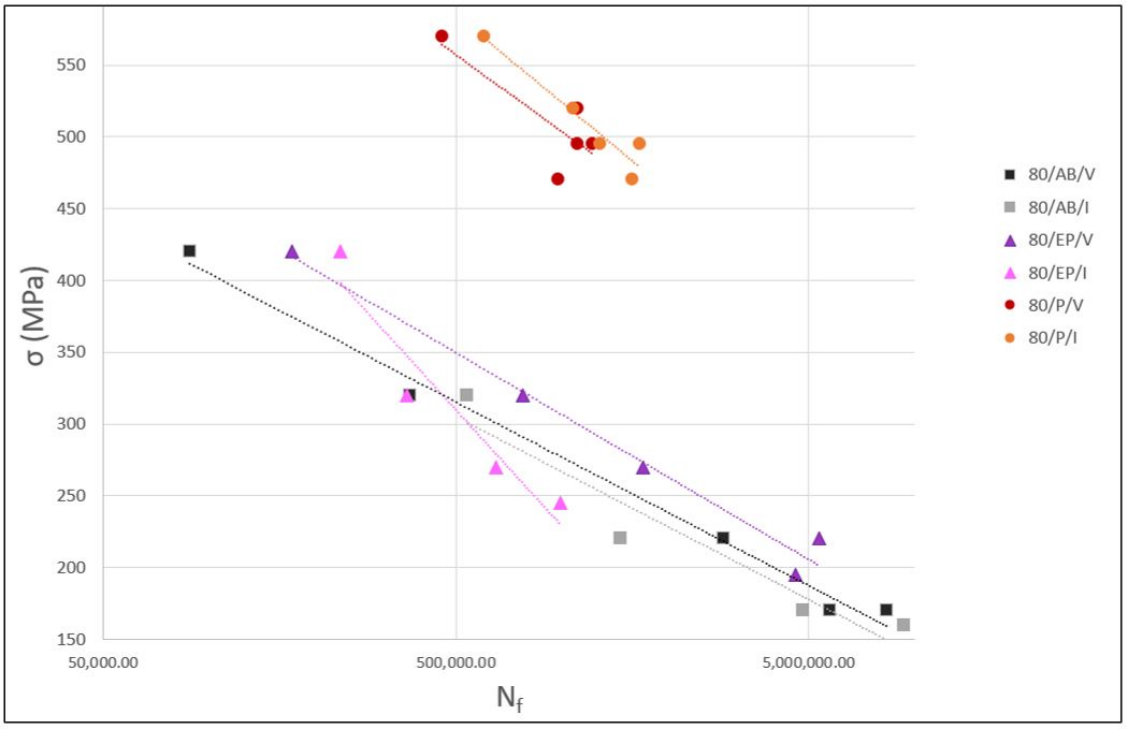

Figure 5.1: Rotating bending fatigue experimental data - 80 µm sample groups

Figure 5.2 shows the results of 40 µm layer thickness sample groups. Note that sample size is limited to 2-3 each for the as-built and electropolished groups. Generally the same trends as 80 µm samples can be observed, with mechanical polished samples able to withstand significantly higher stresses. Again, the difference between as-built and electropolished samples is not very distinct. There again appears to be a trend in favor of vertical samples in withstanding higher cycles before failure.

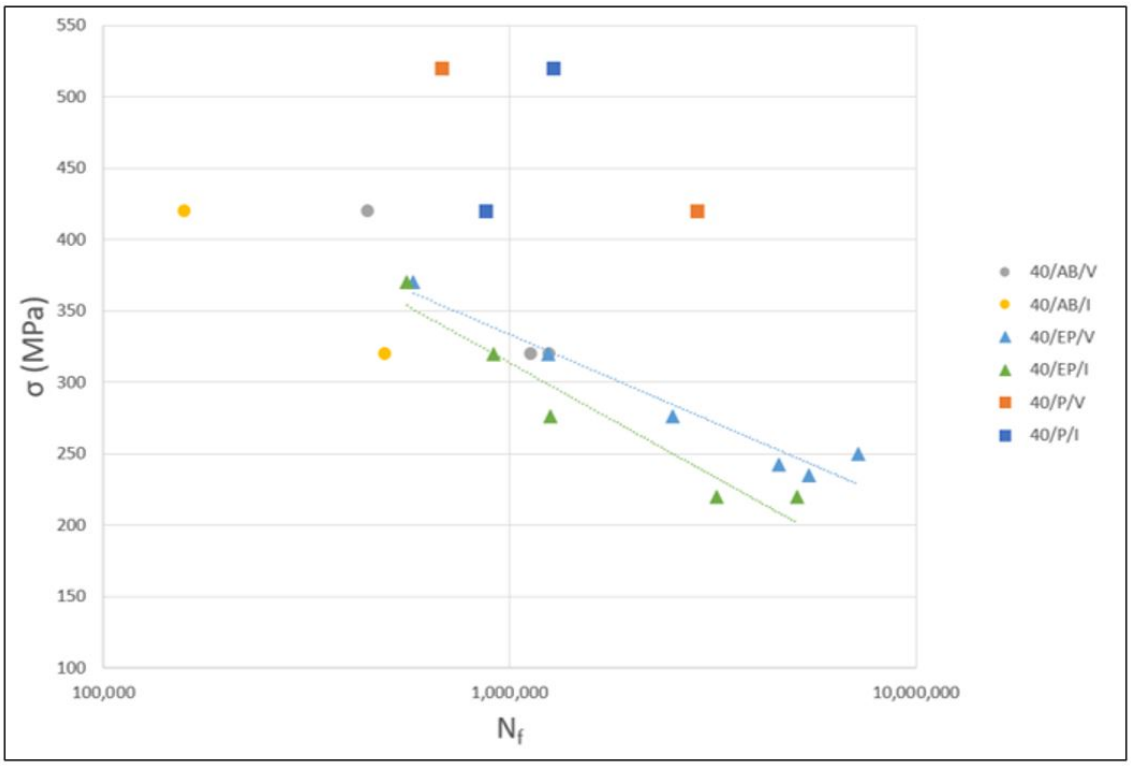

Figure 5.2: Rotating bending fatigue experimental data - 40 µm sample groups

Figure 5.3 shows a comparison of just the electropolished sample groups, showing a trend toward higher cycles to failure with decreased layer thickness. This can be attributed to a lower incidence of lack of fusion porosity, or smaller lack of fusion pores, due to the increase heat input density.

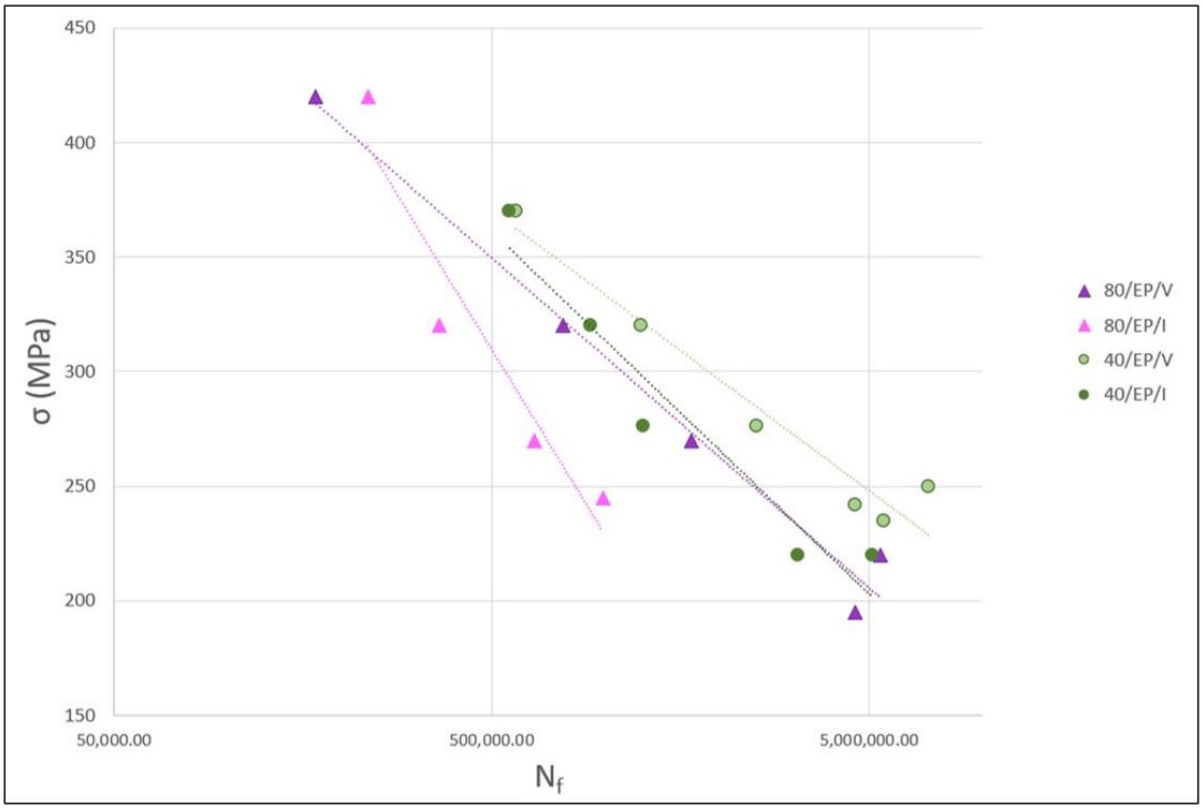

Figure 5.3: Rotating bending fatigue experimental data - electropolished surface condition

5.2. Fractography

The fracture surface of as-built and electropolished samples was generally characterized by multiple crack initiation points, such as in Figure 5.4, while the surfaces of mechanically polished samples were more likely to contain one primary initiation point. It is clear from surface roughness measurements that both as-built and electropolished surfaces are rough and contain notches at the surface, while mechanically polished samples were smoother and more uniform. It is therefore expected for multiple cracks to initiate from multiple locations of stress concentration.

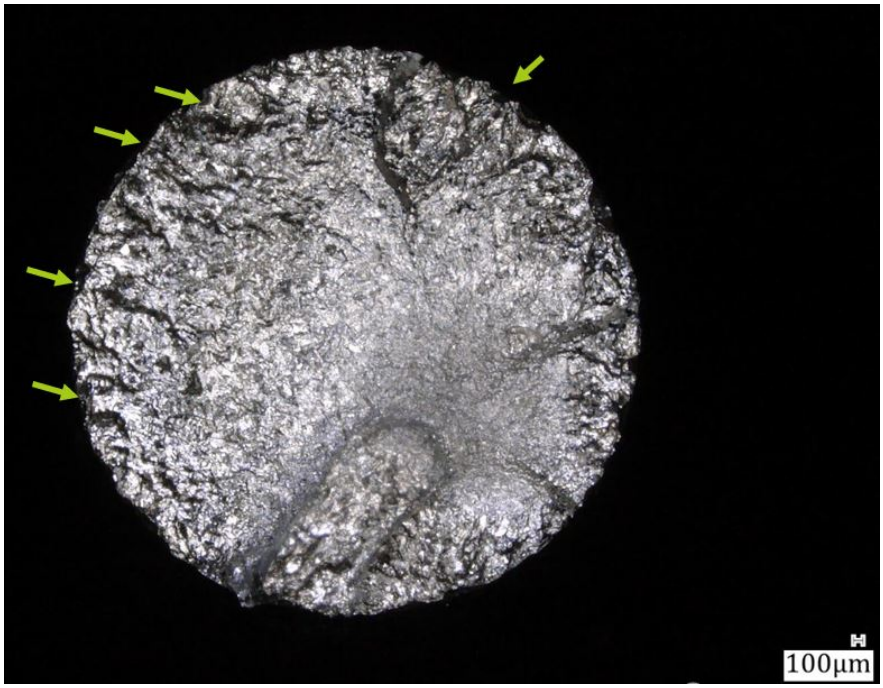

Figure 5.4: Fracture surface of electropolished sample showing multiple crack initiation sites

Almost all fatigue cracks initiated at the surface. This is expected both due to the stress concentration at the surface due to geometrical features and due to the nature of rotating bending fatigue testing, during which the highest stress is at the surface. The large lack of fusion pores observed at the near surface would certainly be points of high stress from which cracks could initiate. Evidence of lack of fusion porosity was identified on the fracture surface of some samples at or near the crack initiation point. One such pore is visible in Figure 5.5. Small spherical particles are apparent, which again could be powder particles that were not successfully melted by the laser or could be spatter from the melt pool.

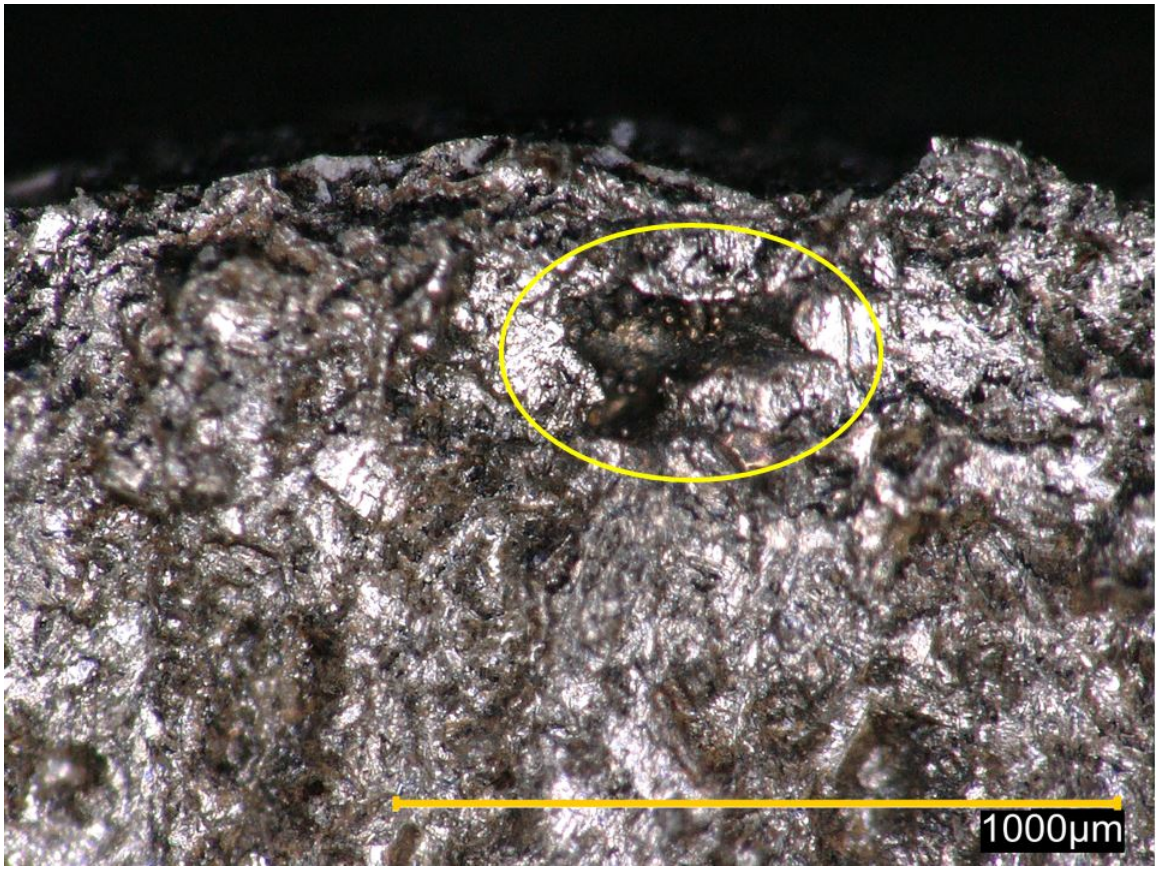

Figure 5.5: Lack of fusion near the crack initiation point for an 80 µm, electropolished, vertical built sample

In rare cases a discoloration was observed on the fracture surface (Figure 5.6). Investigation with SEM-EDS found this discoloration to be an oxide layer on the fracture surface (Figure 5.7). There are a few possible origins for this oxide film, whether it be during the SLM processing, during heat treatment, or from exposure to the environment after heat treatment. If formed during either the SLM processing or the heat-treatment, it could potentially have weakened layer boundaries and caused early failure. In the case of an 80 µm inclined as-built sample that was discontinued during testing, this oxide was noticed on the surface immediately after being separated in a tensile direction in a force tester. The crack was not visible prior to separation, which would have limited the surfaces exposure to oxygen.

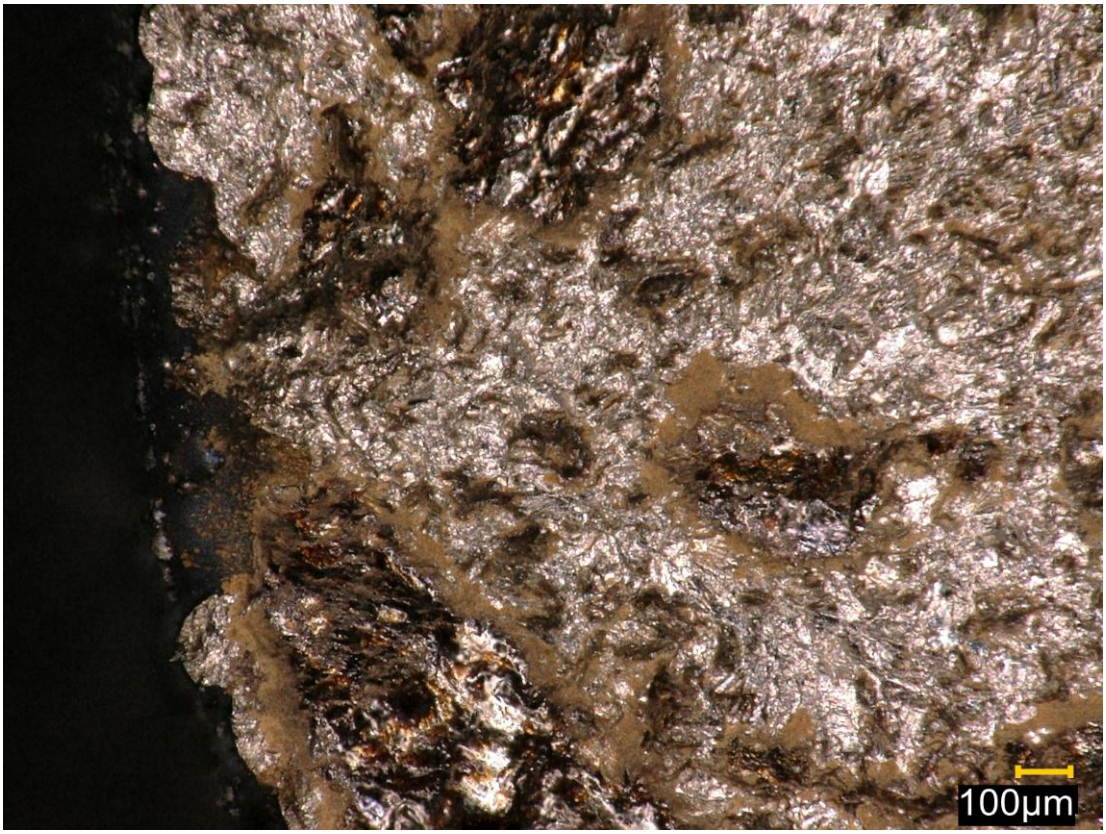

Figure 5.6: Oxide on fracture surface near initiation point

The presence of oxygen on the fracture surface indicates that the oxide was not formed during production, as this occurred in an inert argon environment. This leaves the possibility that it formed during testing. The sample in question is one that was cycled to an extreme level. The fracture surface shows small particles, similar to debris. These particles are smaller than that of the original powder, so they must be formed. The most likely cause of this oxide formation is fretting corrosion caused by repeated rubbing of the fracture surfaces against one another. Material becomes oxidized in the air, aided by the heat generated by the cyclic loading. Subsequent cycling moves this oxide around, exposing a new area that is subsequently oxidized.

EDS spectral analysis of the oxide (Figure 5.7) shows what appears to be a largely Cr, Fe, and Ni oxide. Refer to Section 4.1.2 for discussion of the oxidation of Inconel 718 at elevated temperature. In this case the temperatures generated by friction would not approach those of heat treatment. The volume of oxide formed is not likely to be related to extreme temperature, but rather to high surface area available. As more debris is generated and removed by fretting, additional surface area is exposed for oxidation. The formation of this oxide has the potential accelerate crack propagation.

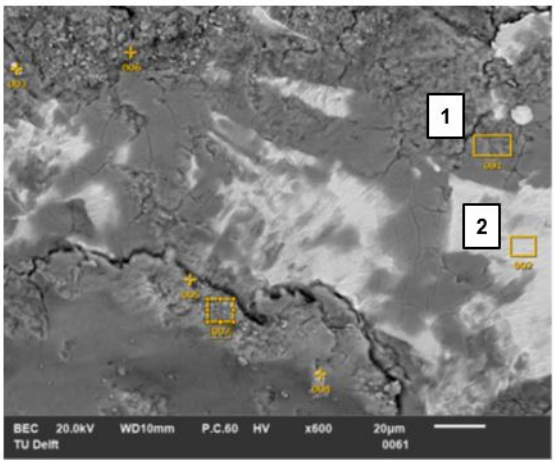

		Fe	O	C	N	Al	Ti	Cr	Mn	Ni	Nb	Mo
1	wt %	12.07	33.34	3.01	-	0.32	0.48	11.97	0.08	33.53	3.51	1.70
2	wt %	18.65	1.04	1.51	-	0.48	1.00	18.27	0.04	52.72	4.18	1.97

Figure 5.7: Backscattered electron image (top) and EDS quantification of oxide on fracture surface (bottom)

Examination of the surfaces of failure samples found evidence that the fatigue cracks may be more likely to initiate at a layer boundaries. Figure 5.8 shows deep notches or small cracks visible at the surface level of an 80 µm sample. The peaks and valleys corresponding to the sample thickness are apparent. The crack appears to be travelling along the layer boundary. This does not necessarily suggest that the layer boundaries are weaker than the bulk. A more likely explanation is that the crack originates preferentially at the layer boundary due to stress concentration from the geometry. This is supported by the fact that almost all fatigue cracks originated at the surface and not in the bulk. The exact scan pattern used is unknown, but from visual examination it appears to be a checkerboard pattern. This leads to greater peaks and valleys at the sample surface which may serve as points of crack initiation.

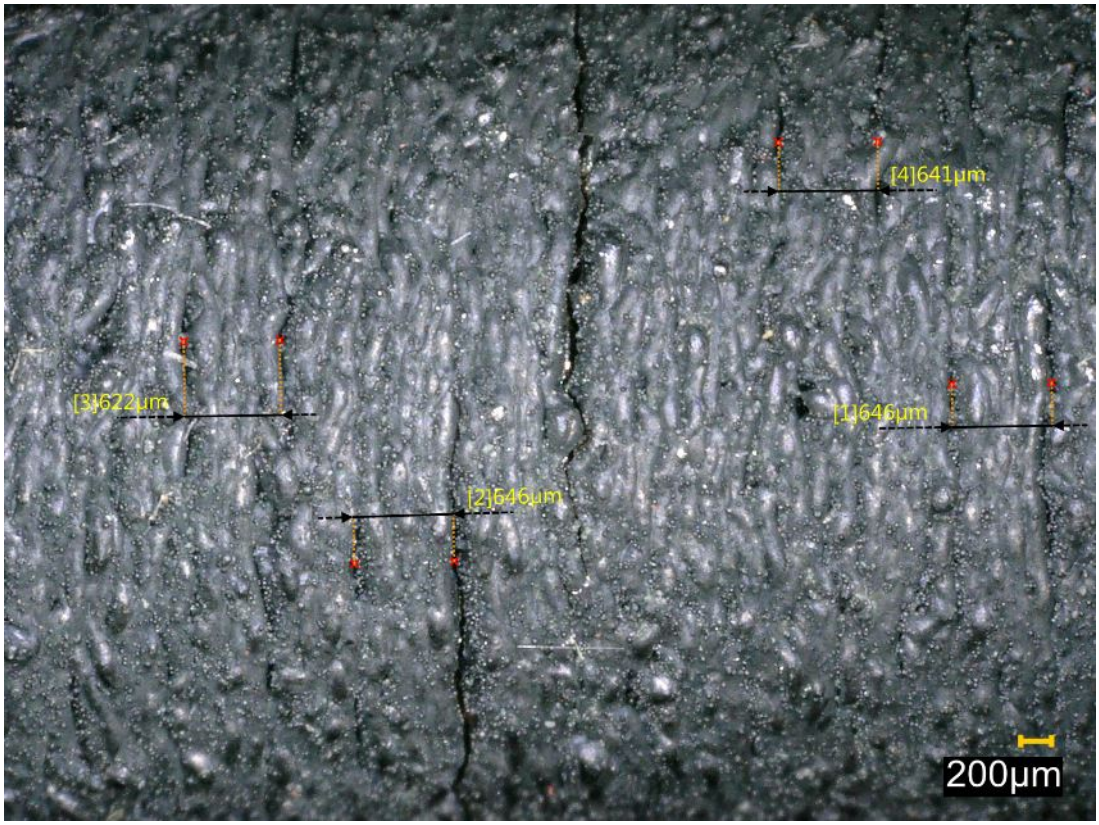

Figure 5.8: Optical image of the outside surface of an 80 µm, inclined, as-built sample

A cross sectional view of the XZ plane shows these crevices (Figures 5.9 and 5.10). They do not appear to be cracks, but rather features formed by the SLM scan process potentially due to incomplete fusion of the layers. This is evident by the smaller grain size near the crevice. The features appear to be between two layer boundaries. Their geometry would lead to a high concentration of stress at that boundary, potentially causing the apparent interlayer cracking seen in Figure 5.8.

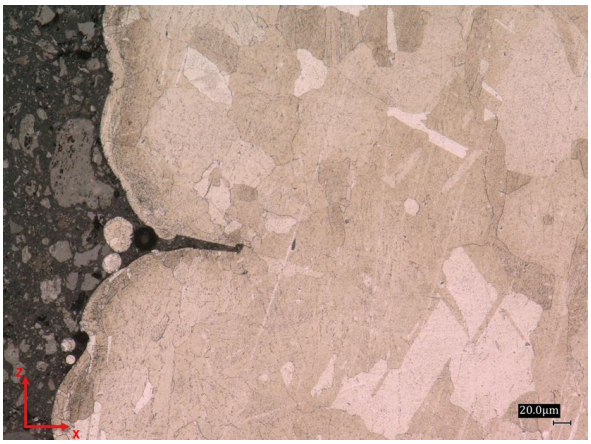

Figure 5.9: Deep ridges in optical micrograph of 80 µm layer thickness, vertical, as-built sample

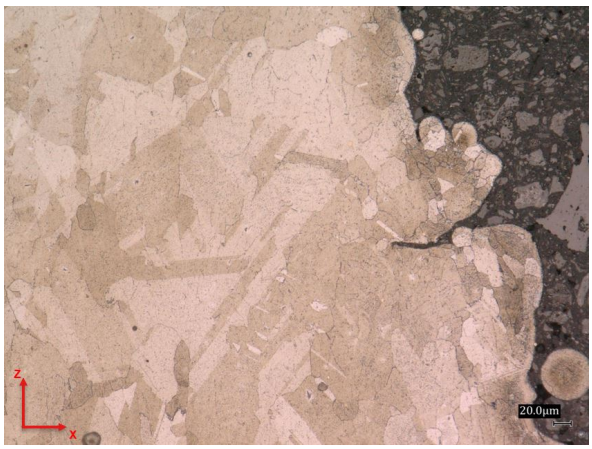

Figure 5.10: Deep ridges in optical micrograph of 80 µm layer thickness, vertical, as-built sample

5.2.1. SEM Analysis

5.2.2. Effect of Inclined Build Direction

The previous chapter outlined variation in the surface appearance and surface roughness of upskin and downskin sides of inclined built samples. From fractography of the failed samples, it is clear that surface defects serve as initiation points for fatigue cracks in this case. It is therefore of interest to understand if the differences in upskin and downskin surface quality leads to a difference in fatigue performance. This information could be used by designers to optimize designs involving incline builds for improved fatigue performance. Figure 5.11 shows the results of this investigation. It is clear that failure overwhelmingly initiates on the downskin side of the sample. An example of this determination is found in Figure 5.12, showing the division of up- and downskin sides with determination of crack initiation point. The samples in Figure 5.11 include as-built and electropolished surface conditions. It was not possible to identify upskin or downskin sides of mechanically built samples, as neither the surface nor microstructure exhibiting identifying characteristics.

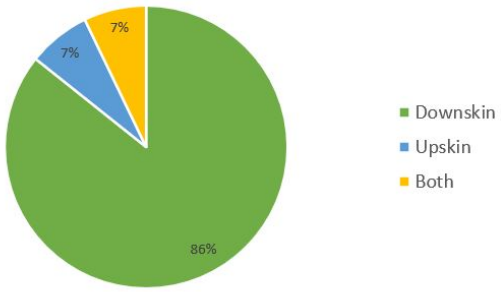

Figure 5.11: Proportion of fatigue cracks which initiated on the upskin, downskin, or on both sides of an inclined sample

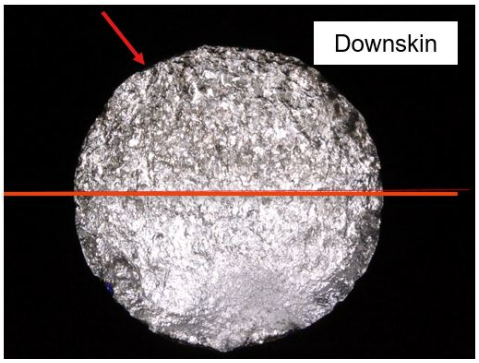

Figure 5.12: Fracture surface of inclined sample, with horizontal line denoting upskin and downskin sides and red arrow pointing to crack initiation point.

There are several factors which may contribute to this difference. For one, the surface roughness has been shown to be greater on the downskin side, as also reported in literature. This difference is apparent in the 80 µm samples, but less so in the 40 µm sample group. Even so, fracture initiates at the downskin for the 40 µm group.

Vickers hardness measurements identified the downskin side to be harder than the upskin. This is a surprising result, as higher hardness is associated with an increase in fatigue limit in the case of small defects, as illustrated in Figure 5.13.

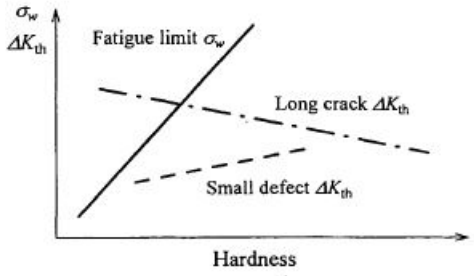

Figure 5.13: Relationship between hardness and fatigue limit [26]

Following the Murakami-Endo equation, which predicts fatigue limit based on hardness and defect size, an increase in hardness should result in an increase in fatigue limit. There must therefore be another factor differentiating upskin and downskin sides of inclined samples which would lead to preferential crack initiation at the downskin down. It seems that differences in the surface condition may be enough to overcome the positive effect of hardness on the downskin side. Additionally, study of the types of defects at which cracks initiate shows that the defects are often large semi-circular notches, extending into the bulk at depths greater than 100 µm. These types of crevices are not easily detected by surface roughness measurement with a light or a laser. This suggests that surface roughness alone may not responsible for this trend, but that larger crevices or greater near surface voiding result in a greater likelihood for crack initiation.

5.3. Fatigue Life Prediction by Murakami-Endo Method

The measured hardness values and area measurements were input into the Murakami-Endo equation to generate a prediction of fatigue limit (lower bound). As outlined in Chapter 3, the upper bound of fatigue limit was calculated based on hardness and represents a limit without influence of defects. It was decided to use the near-surface hardness as the hardness value input, again as the fatigue crack initiates at the surface or near-surface. The focus of this prediction is primarily on the four electropolished sample groups, as these had the adequate sample size and could therefore the prediction could be compared to experimental data.

5.3.1. Results

The following charts show, for each sample group, the predicted upper and lower bound of fatigue limit overlaid with experimental data. The y axis is the applied stress normalized to the predicted lower bound.

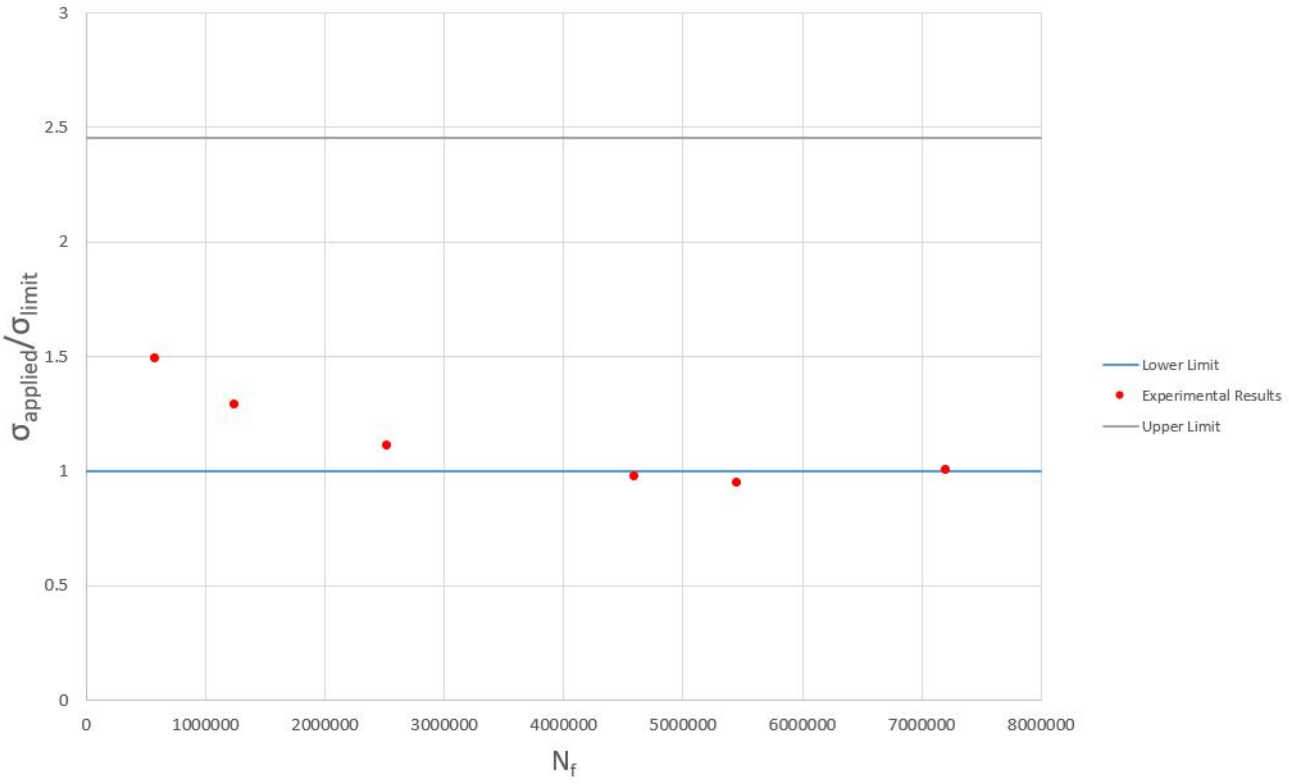

Figure 5.14: Predicted upper and lower bound of fatigue limit for 40 µm, vertical, electropolished sample group, overlaid with experimental fatigue data

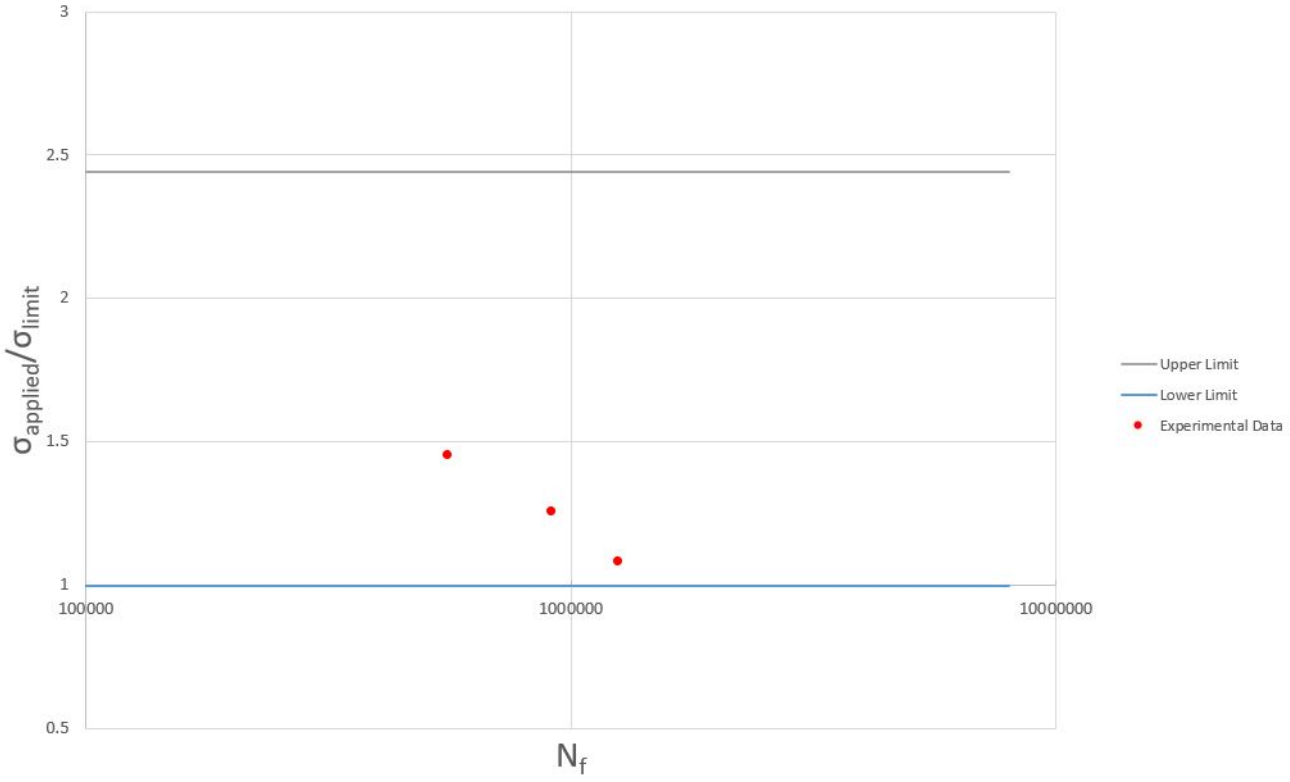

Figure 5.15: Predicted upper and lower bound of fatigue limit for 40 µm, inclined, electropolished sample group, overlaid with experimental fatigue data

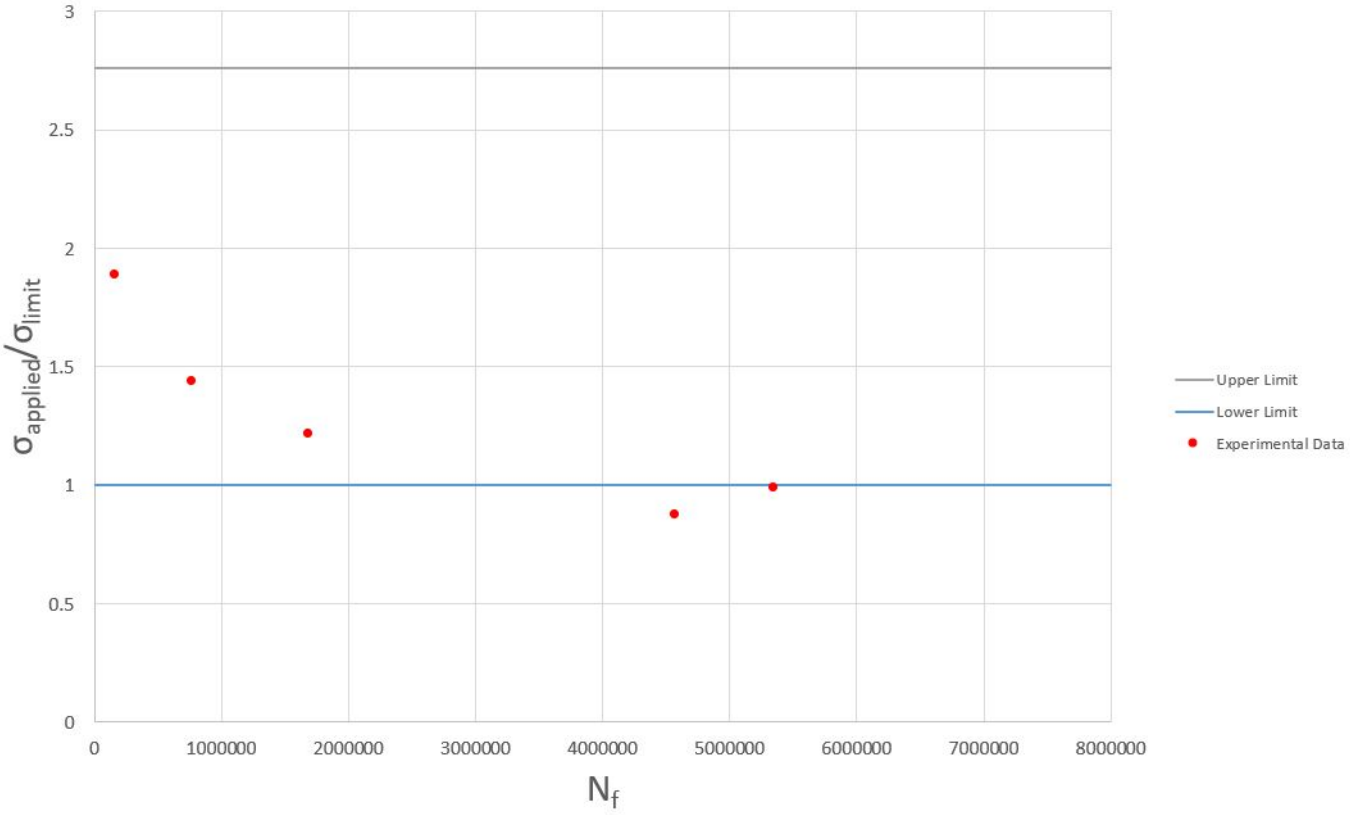

Figure 5.16: Predicted upper and lower bound of fatigue limit for 80 µm, vertical, electropolished sample group, overlaid with experimental fatigue data

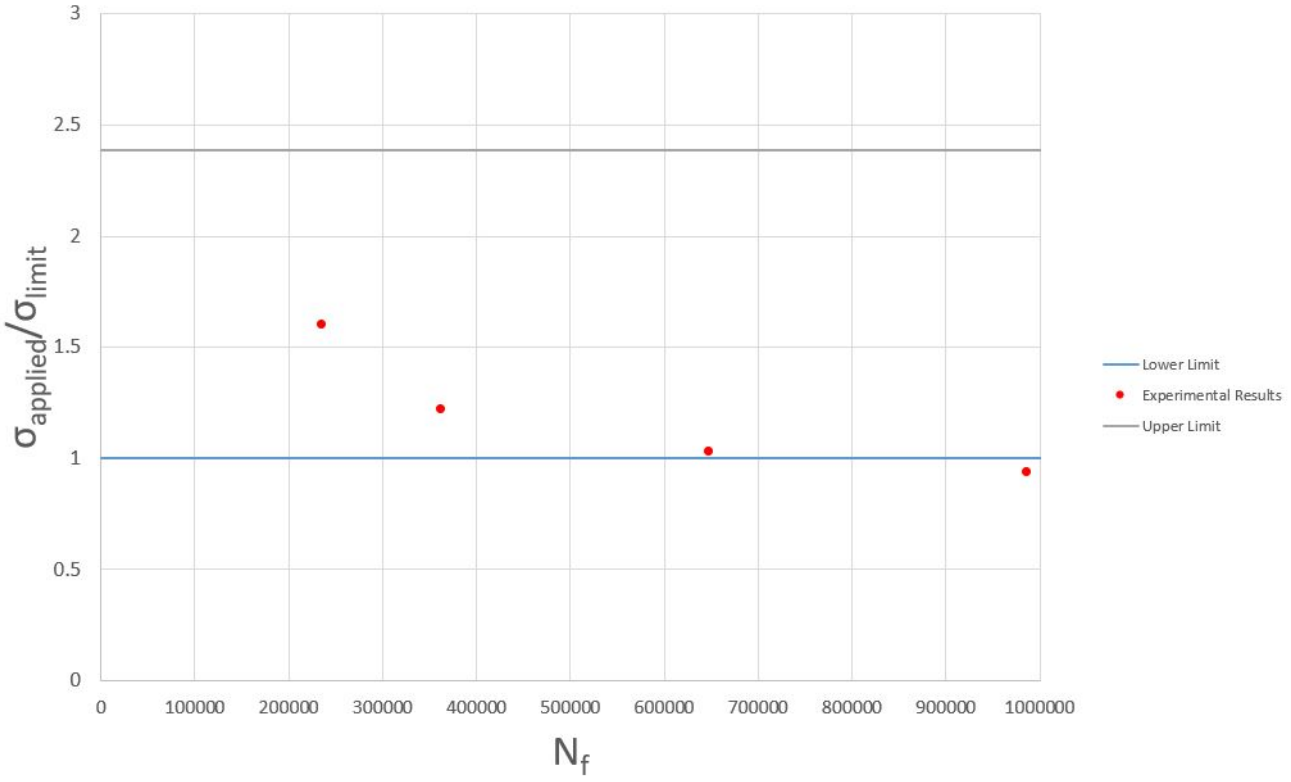

Figure 5.17: Predicted upper and lower bound of fatigue limit for 80 µm, inclined, electropolished sample group, overlaid with experimental fatigue data

Some conclusions can be drawn from the plots themselves. In each sample group the experimental fatigue limit is very close to the lower bound of the prediction. This confirms that the fatigue behavior of these samples is highly defect dependent. Results closer to the upper bound prediction would indicate that defects do not play much of a role in fatigue of that sample group. For comparison, Figure 5.18 shows the prediction for the mechanically polished sample group. The experimental results are must closer to the upper bound of the predicted fatigue life, indicating that fatigue performance for this sample group is less defect dependent than the electropolished samples. This confirms with microstructural observations, which found in the mechanically polished samples none of the surface notches common with the electropolished samples.

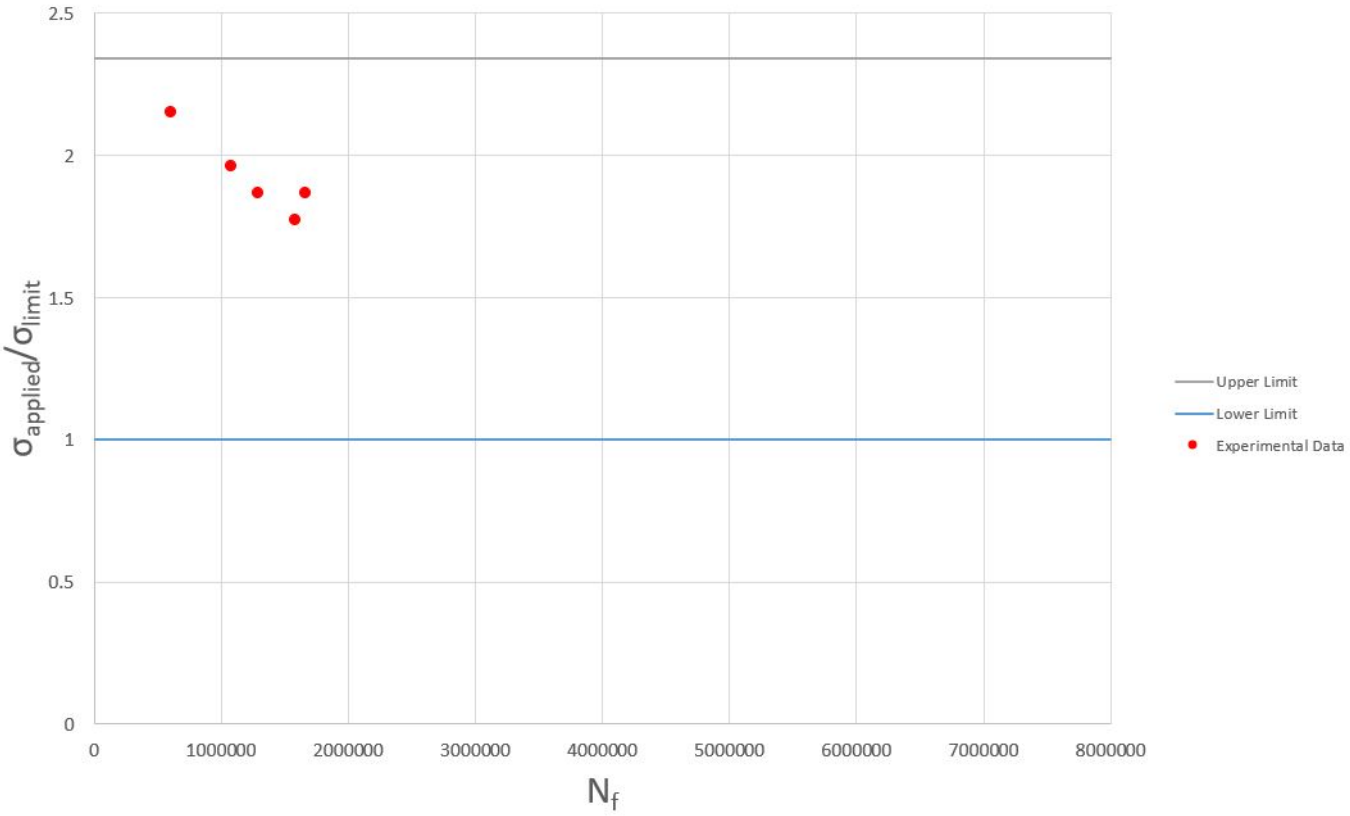

Figure 5.18: Predicted upper and lower bound of fatigue limit for 80 µm, inclined, mechanically sample group, overlaid with experimental fatigue data

A summary of the results and their coordination to experimental data is displayed in Table 5.1. Overall, for the electropolished sample groups this prediction method shows good agreement with experimental results. Other examples in the literature indicate that a σ/σ_{wu} greater than 0.9 is an indicator of good agreement [66]. There are a few potential sources of error in this method. For one, the limited experimental sample size creates difficultly in determining a fatigue limit with multiple data points and replications near the limit stress. This could affect the agreement with the prediction. Additionally, as the model is defect sensitive, the prediction is based only the defects identified in the 4-6 samples within a sample group. This limits the confidence with which the model can be applied to all samples generated with the processing of that sample group. The results are promising however, and provide a good indication that fatigue limit can be predicted within a certain margin of error based on analysis of defects. With greater confidence based on greater sample size, fatigue limit could be determined with minimal fatigue testing - based on defects identified with non-destructive testing means such as laser interferometry or Micro-CT. Subsequent fatigue testing could then focus in more narrowly on the expected fatigue limit, saving time and testing cost.

Table 5.1: Summary of fatigue life predicted by Murakami-Endo relationship (lower bound) and relationship to experimental results

	80/EP/V	**80/EP/I**	**40/EP/V**	**40/EP/I**
Prediction fatigue life (MPa)	222	263	249	255
Experimental σ/σ_{wu}	0.88	0.93	0.97	0.86

In this case, the Murakami-Endo method seems to overestimate the fatigue limit in comparison to experimental data. This trend was also noted in literature [67]. Manatsu et al. found that experimental fatigue limit corresponded to a defect size greater than what was possible as a result SLM processing. Therefore the Murakami-Endo method itself may be too simplistic to provide an exact prediction of fatigue limit. Some error would alway then be expected. It is possible that this error is consistent across many sample groups and could be corrected with a factor, but this requires extensive study to determine.

5.3.2. Defect Identification and Analysis

As stated, the model outlined above is specific to the identified defect population in the sample group. However, this sample size is fairly low and yields a maximum of only 6 $\sqrt{area}$ measurements per sample group, with the prediction based on the largest defect identified. For the purposes of an accurate fatigue life prediction, it is desirable to understand the range of defects possible in a given population of SLM Inconel 718, manufactured with the same processing and post-processing conditions. An identified population of defects can used to understand trends between sample groups.

Micro-CT was used to identify defects within an 80 µm, vertical, electropolished sample. These defects (located solely at the surface) were measured and plotted on a cumulative frequency chart (Figure 5.19), with measured $\sqrt{area}$ on the x axis and y, the reduced variate, on the y axis. Y is a function of F, the empirical cumulative probability, and is determined by the following equation [18]:

$$Y = -ln(-lnF) \tag{5.1}$$

By plotting the cumulative frequency chart in this way, trends can be identified in the pore sizes of various sample groups. This method, a type of extreme statistics analysis, can give an indication of the distribution of defects in the current population. A line was fit to the defects using the least square method. The slope of this line can give an indication of the probability of larger defects, as the next largest defect identified would fall on this line. A steep slope would indicate, based on the trend of identified defects, that the next largest defect is not likely to be much larger than the previous.

In this case, blue dots indicate defects found by Micro-CT, while the red dots are the defects measured on the fracture surface of tested samples. The defects on the fracture surface are among the largest, as can be expected. The largest defect in a sample is the most likely to have the highest stress concentration and serve as the primary crack initiation point. Interestingly, some of the red dots are comparable in size to large defects identified by CT. This demonstrates the capability of Micro-CT to identify and measure the largest defect in a non-destructive manner, which can be fed in the Murakami-Endo prediction. The defects do not however closely follow the linear regression line as expected and seen in literature [18, 67]. The reasons for this could be limitations in sample size and defects identified, as well as the method for measuring size. Defects were located and measured manually using CT data or fractography methods. Some amount of human error is expected, as well as a skew towards the largest defects in the sample. Automatic measurement of defect size via CT software would likely result in a more even distribution of sizes along the linear regression line.

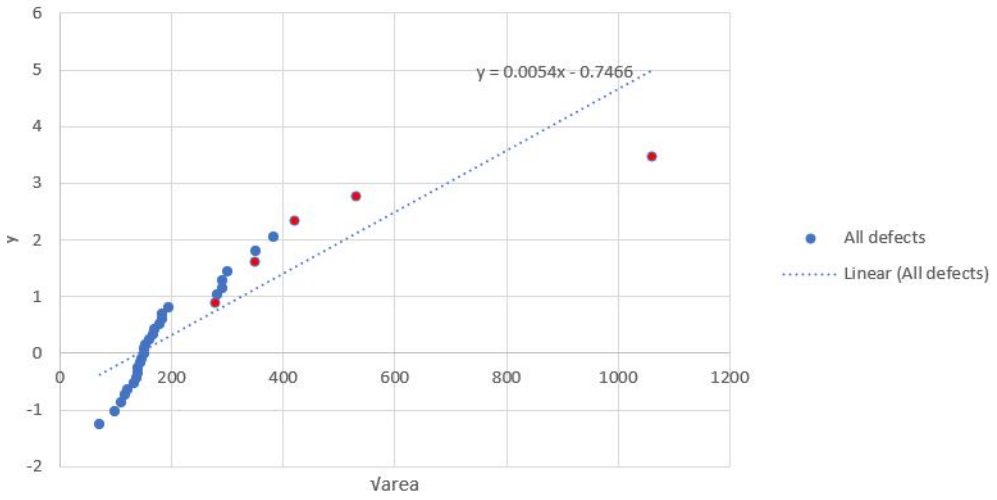

Figure 5.19: Cumulative frequency of identified defect sizes in 80 µm, vertical, electropolished. Measured with CT

Plotting the identified defects in such a frequency chart can also provide information about defect size trends in different sample populations. Figure 5.20 shows a comparison of the defect size distribution for each layer thickness in the as-built surface condition. Figure 5.21 is the same but for the elctropolished surface. Both show a trend towards larger defect size with larger layer thickness. This comparison is made based on a very limited sample size and would require further investigation.

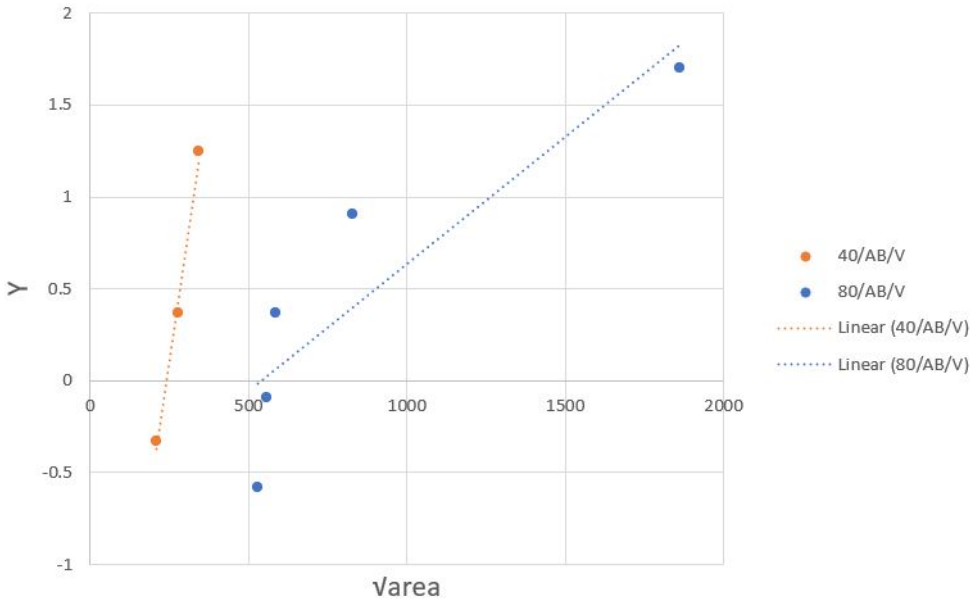

Figure 5.20: Cumulative frequency of identified defect sizes vertical, as-built sample groups

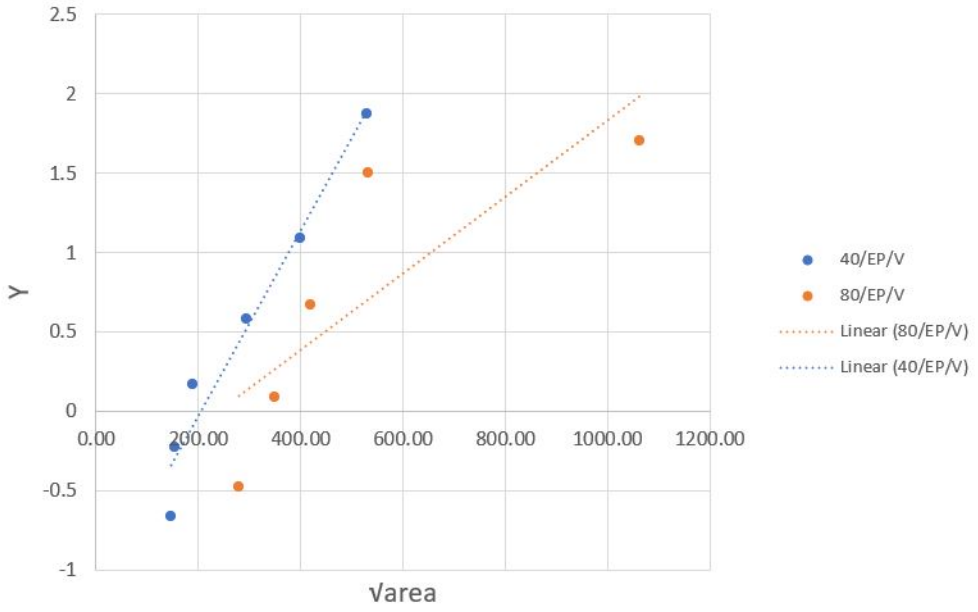

Figure 5.21: Cumulative frequency of identified defect sizes vertical, electropolished sample groups

The cumulative frequency chart of 80 µm layer thickness and electropolished surface condition shows a trend toward larger defects in the vertical build direction. Again, this trend is based on a limited sample size.

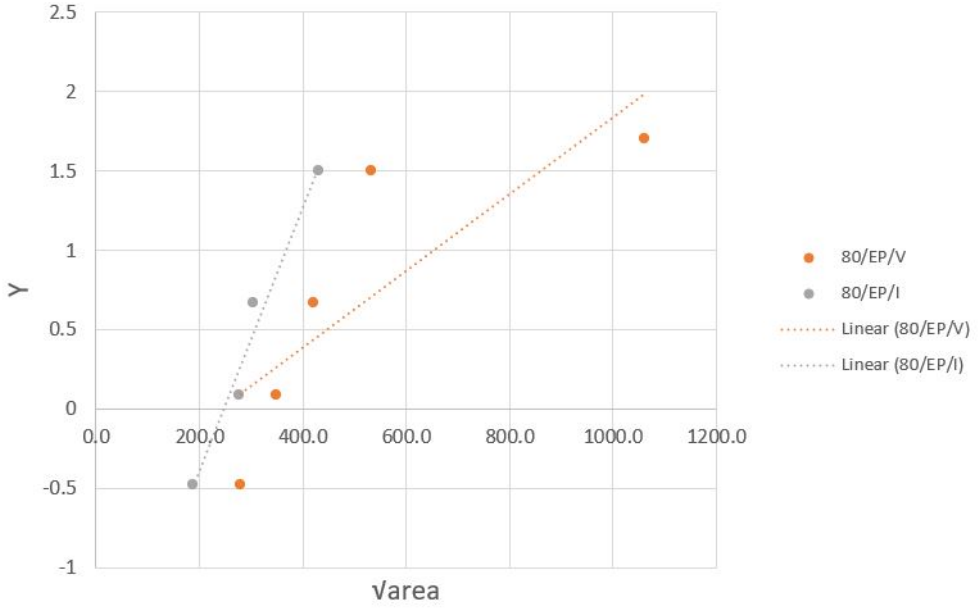

Figure 5.22: Cumulative frequency of identified defect sizes in 80 µm, vertical, electropolished.

Sensitivity to Measurement

The Murakami-Endo equation is dependent on two measured inputs, hardness and largest defect. As has been previously demonstrated, hardness of SLM alloys can often be variable even after HIP post-treatment, due to precipitate and secondary phase formation, as well as the difference in microstructure due to differences in thermal history. The measurement of $\sqrt{area}$ is also open to human error, as defect boundaries are not always distinct. The measurement of hardness, being directly proportional to predicted fatigue limit, has the greater impact on the prediction than $\sqrt{area}$.

6

Conclusions and Recommendations

6.1. Conclusions

1. Characterization of the effect of differing SLM layer thicknesses and build direction on microstructure, defects and surface condition

    - The two different layer thicknesses, 40 µm and 80 µm, did not lead to significant differences in microstructure or material properties in the core. Density and hardness were comparable between the two layer thicknesses. A difference in surface roughness was discernible, with 80 µm layer thickness producing a rougher surface.
    - The inclined build direction at approximately 63° produced noticeable differences in properties within the same sample. The downskin side of the sample is significantly harder than that of the opposite upskin side in the case of 80 µm samples. This phenomenon could be contributed to a higher degree of niobium carbide formation at the upskin side, which would pull strengthening niobium from the matrix.

2. Characterization of how two different post-processing surface treatments (electropolishing and mechanical polishing) affect the surface condition, near-surface porosity, and resulting fatigue performance.

    - There is an observable trend towards improved fatigue performance in 40 µm sample compared to 80 µm samples, which may be attributed to higher surface roughness of the 80 µm group.
    - Electropolishing does not have a significant impact on the surface quality in terms of roughness or in near surface porosity. The level of material removed by electropolishing (approximately 10-20 µm radially) removes partially melted particles at the surface, but does not sufficiently reduce the severity of large ridges or notches. The process also does not remove lack of fusion porosity present around 50 µm from the surface. Consequently, electropolishing at the level performed on these samples did not significantly improve the fatigue performance of the SLM Inconel 718.
    - Defects are the surface or near surface are indeed the source of fatigue failures. No such pores were observed in mechanically polished samples due to material removal via the polishing process. The improvement in fatigue performance of polished samples compared to other sample groups is significant. The reduction or removal of these pores is therefore vital in the improvement of fatigue life.

3. Development of a predictive model for the fatigue limit of SLM Inconel 718 based on defect size and location.

    - The Murakami-Endo method of fatigue life prediction was successful in producing a prediction with good agreement to experimental data. More testing and replications are needed to improve the confidence of the model, but it appears to provide a viable method of fatigue limit prediction based solely on defects and material properties. If defects can be measured with non-destructive means, fatigue limit could be predicted without the need for extensive experimental testing.

General Observations

- Titanium nitride particles were observed in the feedstock powder. Without knowledge of the powder atomization process, the source of these inclusions is unknown. The TiN inclusions agglomerate together via the SLM process, particularly concentrating at near-surface voids. The strain associated with these inclusions would increase the stress concentration at these voids.
- The feedstock powder particles were not perfectly spherical, but often irregular or elongated in shape. This may be a result of recycling. This morphology can negatively impact flowability or powder bed density, which in turn could negatively effect the density of the resulting part. As these samples underwent HIP, it is not clear if low density was an issue in the as-processed state.

6.2. Recommendations for Future Work

- The limited sample size in each sample group reduces the confidence in the predicted fatigue life results, both because the prediction is a defect-based approach determined by the population of found defects and because the accuracy of the prediction cannot be confirmed without a full SN curve construction requiring more samples. This requires multiple replications of stress levels, particularly in the high cycle regime, for the determination of fatigue life.
- This work focused on the crack initiation behavior of SLM Inconel 718. Further study is necessary to understand the crack propagation behavior of this material. In particular, investigation into whether the TiN non-metallic inclusions or observed fracture surface oxide provides energetically favorable paths for crack propagation.
- Observed irregularties in feedstock powder shape require further characterization to determine if factors such as flowability or bed packing density are negatively affected. Also, as-processed SLM material before HIP or subsequent heat treatments should be studied to confirm if lack of fusion porosity is present throughout the sample or is isolated at the surface.
- SLM components using this process will be utilized in a corrosive environment in practice. Therefore, the corrosion and/or hydrogen embrittlement behavior of this material must be studied to understand differences in corrosion and hydrogen embrittlement resistance between and SLM component and a traditionally wrought one. In particular, the effect of process defects on the fatigue behavior and potential for stress corrosion cracking. The rough surface of as-built and electropolished samples provide notches for potential autocatalytic corrosion and localized highly corrosive environment. The large titanium nitrides identified will pull titanium from the matrix and could prevent the localized formation of a titanium oxide passivating layer. All of these aspects require a complete study.
- Surface and near-surface lack of fusion defects are shown to serve as initiation points for fatigue failure. Processing and post-processing techniques should focus on the reduction or elimination of such defects. Mechanical polishing removes enough material to remove these defects; however, this process is not feasible for complex geometries. Remelting of the edges during SLM processing is a possible method to eliminate these voids or reduce their size. The process provides additional energy to the layer, allowing the powder to fully melt and fuse. As only the edge of the component is remelting, the impact on processing time is not as significant as remelting of the whole layer. Investigation should be performed on samples with this processing technique, both on the microstructure to see if indeed the process results in a reduction in near-surface porosity and fatigue testing to see if the process improves fatigue life. Potentially, the fatigue life could reach the level seen by mechanically polished samples in this study.

Bibliography

[1] William E. Frazier. Metal additive manufacturing: A review. *Journal of Materials Engineering and Performance*, 23(6):1917–1928, 2014.

[2] Nesma T. Aboulkhair, Nicola M. Everitt, Ian Ashcroft, and Chris Tuck. Reducing porosity in alsi10mg parts processed by selective laser melting. *Additive Manufacturing*, 1-4:77 – 86, 2014. Inaugural Issue.

[3] Chor Yen Yap, C. Chua, Z. Dong, Z. Liu, D. Zhang, L.E. Loh, and Swee Leong Sing. Review of selective laser melting: Materials and applications. *Applied Physics Reviews*, 2:041101, 12 2015.

[4] Jean-Pierre Kruth. Selective laser melting of iron-based powder. *Journal of Materials Processing Technology*, 149(1):616 – 622, 2004. 14th Interntaional Symposium on Electromachining (ISEM XIV).

[5] K.N. Amato, S.M. Gaytan, L.E. Murr, E. Martinez, P.W. Shindo, J. Hernandez, S. Collins, and F. Medina. Microstructures and mechanical behavior of inconel 718 fabricated by selective laser melting. *Acta Materialia*, 60(5):2229 – 2239, 2012.

[6] Imade Koutiri, Etienne Pessard, Patrice Peyre, Ouafae Amlou, and Thibaut De Terris. Influence of slm process parameters on the surface finish, porosity rate and fatigue behavior of as-built inconel 625 parts. *Journal of Materials Processing Technology*, 255:536 – 546, 2018.

[7] E. Yasa and J. Kruth. Application of laser re-melting on selective laser melting parts. *Advances in Production Engineering and Management*, 6:259–270, 2011.

[8] R. Casati, J. Lemke, and M. Vedani. Microstructure and fracture behavior of 316l austenitic stainless steel produced by selective laser melting. *Journal of Materials Science and Technology*, 32(8):738 – 744, 2016.

[9] Ming Tang, P. Chris Pistorius, and Jack L. Beuth. Prediction of lack-of-fusion porosity for powder bed fusion. *Additive Manufacturing*, 14:39 – 48, 2017.

[10] Ruidi Li, Jinhui Liu, Yusheng Shi, Li Wang, and Wei Jiang. Balling behavior of stainless steel and nickel powder during selective laser melting process. *International Journal of Advanced Manufacturing Technology - INT J ADV MANUF TECHNOL*, 59, 04 2012.

[11] Yang Liu, Yongqiang Yang, and Di Wang. A study on the residual stress during selective laser melting (slm) of metallic powder. *The International Journal of Advanced Manufacturing Technology*, 87:647–656, 2016.

[12] E. Yasa and J-P. Kruth. Microstructural investigation of selective laser melting 316l stainless steel parts exposed to laser re-melting. *Procedia Engineering*, 19:389 – 395, 2011. 1st CIRP Conference on Surface Integrity (CSI).

[13] Brecht [Van Hooreweder], Yanni Apers, Karel Lietaert, and Jean-Pierre Kruth. Improving the fatigue performance of porous metallic biomaterials produced by selective laser melting. *Acta Biomaterialia*, 47:193 – 202, 2017.

[14] S.G.K. Manikandan, D. Sivakumar, and M. Kamaraj. 1 - physical metallurgy of alloy 718. In S.G.K. Manikandan, D. Sivakumar, and M. Kamaraj, editors, *Welding the Inconel 718 Superalloy*, pages 1 – 19. Elsevier, 2019.

[15] Dongyun Zhang, Zhe Feng, Chengjie Wang, Weidong Wang, Zhen Liu, and Wen Niu. Comparison of microstructures and mechanical properties of inconel 718 alloy processed by selective laser melting and casting. *Materials Science and Engineering: A*, 724:357 – 367, 2018.

[16] F.C. Campbell. *Fatigue and Fracture - Understanding the Basics*. ASM International, 2012.

[17] A. Riemer, S. Leuders, M. Thöne, H.A. Richard, T. Tröster, and T. Niendorf. On the fatigue crack growth behavior in 316l stainless steel manufactured by selective laser melting. *Engineering Fracture Mechanics*, 120:15 – 25, 2014.

[18] Viet-Duc Le, Etienne Pessard, Franck Morel, and François Edy. Interpretation of the fatigue anisotropy of additively manufactured ta6v alloys via a fracture mechanics approach. *Engineering Fracture Mechanics*, 214:410 – 426, 2019.

[19] A. Gupta, W. Sun, and C.J. Bennett. Simulation of fatigue small crack growth in additive manufactured ti–6al–4v material. *Continuum Mechanics and Thermodynamics*, 2020.

[20] Peter Grohs. Estimation of the fatigue life of additively manufactured metallic components using modified strain life parameters based on surface roughness. *Master's Thesis*, 2019.

[21] Patricio Carrion and Nima Shamsaei. Strain-based fatigue data for ti–6al–4v eli under fully-reversed and mean strain loads. *Data in Brief*, 7, 02 2016.

[22] Keyence. Surface roughness parameters.

[23] Klas Solberg, Di Wan, and Filippo Berto. Fatigue assessment of as□built and heat□treated inconel 718 specimens produced by additive manufacturing including notch effects. *Fatigue and Fracture of Engineering Materials and Structures*, 07 2020.

[24] Y. Murakami and M. Endo. Effects of defects, inclusions and inhomogeneities on fatigue strength. *International Journal of Fatigue*, 16(3):163 – 182, 1994.

[25] University of Cambridge. Ellingham diagrams, 2020.

[26] Yoshiyuki KONDO, Chu SAKAE, Masanobu KUBOTA, and Takao KUDOU. The effect of mean stress and hardness on the fatigue limit of material with small defect. *Transactions of the Japan Society of Mechanical Engineers Series A*, 68(672):1185–1191, 2002.

[27] Jing Zhang and Yeon-Gil Jung. *Additive Manufacturing - Materials, Processes, Quantifications and Applications*. Elsevier, 2018.

[28] Jean-Pierre Kruth, M. Badrossamay, Evren Yasa, Jan Deckers, Lore Thijs, and Jan Humbeeck. Part and material properties in selective laser melting of metals. *16th International Symposium on Electromachining, ISEM 2010*, 01 2010.

[29] F. Bartolomeu, M. Buciumeanu, E. Pinto, N. Alves, O. Carvalho, F.S. Silva, and G. Miranda. 316l stainless steel mechanical and tribological behavior—a comparison between selective laser melting, hot pressing and conventional casting. *Additive Manufacturing*, 16:81 – 89, 2017.

[30] Oleg D. Neikov. Chapter 13 - powders for additive manufacturing processing. In Oleg D. Neikov, Stanislav S. Naboychenko, and Nikolay A. Yefimov, editors, *Handbook of Non-Ferrous Metal Powders (Second Edition)*, pages 373 – 399. Elsevier, Oxford, second edition edition, 2019.

[31] Yong Sun, Adam Moroz, and K. Alrbaey. Sliding wear characteristics and corrosion behaviour of selective laser melted 316l stainless steel. *Journal of Materials Engineering and Performance*, 23, 02 2014.

[32] Jitka Metelkova, Yannis Kinds, Karolien Kempen, Charlotte de Formanoir, Ann Witvrouw, and Brecht Van Hooreweder. On the influence of laser defocusing in selective laser melting of 316l. *Additive Manufacturing*, 23:161 – 169, 2018.

[33] I. Yadroitsev and I. Smurov. Surface morphology in selective laser melting of metal powders. *Physics Procedia*, 12:264 – 270, 2011. Lasers in Manufacturing 2011 - Proceedings of the Sixth International WLT Conference on Lasers in Manufacturing.

[34] S.D. Jadhav, S. Dadbakhsh, L. Goossens, J-P Kruth, J. Van Humbeeck, and K. Vanmeensel. Influence of selective laser melting process parameters on texture evolution in pure copper. *Journal of Materials Processing Technology*, 270:47 – 58, 2019.

[35] K. G. Prashanth, S. Scudino, T. Maity, J. Das, and J. Eckert. Is the energy density a reliable parameter for materials synthesis by selective laser melting? *Materials Research Letters*, 5(6):386–390, 2017.

[36] Yusuf Kaynak and Ozhan Kitay. The effect of post-processing operations on surface characteristics of 316l stainless steel produced by selective laser melting. *Additive Manufacturing*, 26:84 – 93, 2019.

[37] Jiajun Xu, Youmin Rong, Yu Huang, Pingjiang Wang, and Chunming Wang. Keyhole-induced porosity formation during laser welding. *Journal of Materials Processing Technology*, 252:720 – 727, 2018.

[38] Hot isostatic pressing (hip).

[39] American Metals Co. 316l stainless steel technical data sheet.

[40] Naor Elad Uzan, Shlomo Ramati, Roni Shneck, Nachum Frage, and Ori Yeheskel. On the effect of shot-peening on fatigue resistance of alsi10mg specimens fabricated by additive manufacturing using selective laser melting (am-slm). *Additive Manufacturing*, 21:458 – 464, 2018.

[41] K. Alrbaey, D. I. Wimpenny, A. A. Al-Barzinjy, and A. Moroz. Electropolishing of Re-melted SLM Stainless Steel 316L Parts Using Deep Eutectic Solvents: 3 × 3 Full Factorial Design. *Journal of Materials Engineering and Performance*, 25(7):2836–2846, July 2016.

[42] Wakshum M. Tucho, Priscille Cuvillier, Atle Sjolyst-Kverneland, and Vidar Hansen. Microstructure and hardness studies of inconel 718 manufactured by selective laser melting before and after solution heat treatment. *Materials Science and Engineering: A*, 689:220 – 232, 2017.

[43] Jiangwei Liu, Yanan Song, Chaoyue Chen, Xiebin Wang, Hu Li, Chang'an Zhou, Jiang Wang, Kai Guo, and Jie Sun. Effect of scanning speed on the microstructure and mechanical behavior of 316l stainless steel fabricated by selective laser melting. *Materials and Design*, 186:108355, 2020.

[44] K. Moussaoui, W. Rubio, M. Mousseigne, T. Sultan, and F. Rezai. Effects of selective laser melting additive manufacturing parameters of inconel 718 on porosity, microstructure and mechanical properties. *Materials Science and Engineering: A*, 735:182 – 190, 2018.

[45] Adriaan Spierings, Thomas Starr, and Konrad Wegener. Fatigue performance of additive manufactured metallic parts. *Rapid Prototyping Journal*, 19, 03 2013.

[46] E. Chlebus, K. Gruber, B. Kuźnicka, J. Kurzac, and T. Kurzynowski. Effect of heat treatment on the microstructure and mechanical properties of inconel 718 processed by selective laser melting. *Materials Science and Engineering: A*, 639:647 – 655, 2015.

[47] Muhammad Moiz. Influence of grain size on the mechanical properties of inconel 718. *Dissertation*, 2013.

[48] M. Janssen, J. Zuidema, and R. Wanhill. *Fracture Mechanics, Second Edition*. Taylor and Francis, 2004.

[49] Yung-Li Lee, Jwo Pan, Richard B. Hathaway, and Mark E. Barkey. *Fatigue Testing and Analysis - Theory and Practice*. Elsevier, 2005.

[50] J. J. Schirra, R. H. Caless, and R. Hatala. The effect of laves phase on the mechanical properties of wrought and cast + hip inconel 718. *Superalloys*, pages 375–388, 1991.

[51] Kwai S. Chan, Marie Koike, Robert L. Mason, and Toru Okabe. Fatigue life of titanium alloys fabricated by additive layer manufacturing techniques for dental implants. *Metallurgical and Materials Transactions A*, 44(2):1010–1022, oct 2012.

[52] Julius N. [Domfang Ngnekou], Yves Nadot, Gilbert Henaff, Julien Nicolai, and Lionel Ridosz. Influence of defect size on the fatigue resistance of alsi10mg alloy elaborated by selective laser melting (slm). *Procedia Structural Integrity*, 7:75 – 83, 2017. 3rd International Symposium on Fatigue Design and Material Defects, FDMD 2017.

[53] Xiaoyuan Lou, Michelle A. Othon, and Raul B. Rebak. Corrosion fatigue crack growth of laser additively-manufactured 316l stainless steel in high temperature water. *Corrosion Science*, 127:120 – 130, 2017.

[54] Zhixin Zhan, Hua Li, and K.Y. Lam. Development of a novel fatigue damage model with am effects for life prediction of commonly-used alloys in aerospace. *International Journal of Mechanical Sciences*, 155:110 – 124, 2019.

[55] Stephanie Glen. Box plot (box and whiskers): How to read one and how to make one in excel, ti-83, spss, 2020.

[56] Stephanie Glen. How to calculate the least significant difference (lsd), 2020.

[57] Yukitaka Murakami, Toshihiko Kanezaki, Yoji Mine, and Saburo Matsuoka. Hydrogen embrittlement mechanism in fatigue of austenitic stainless steels. *Metallurgical and Materials Transactions A*, 39:1327–1339, 06 2008.

[58] Christopher Pleass and Sathiskumar Jothi. Influence of powder characteristics and additive manufacturing process parameters on the microstructure and mechanical behaviour of inconel 625 fabricated by selective laser melting. *Additive Manufacturing*, 24:419 – 431, 2018.

[59] Bau Nguyen, Mui Ling Sharon Nai, Zhiguang Zhu, Chen-Nan Sun, J. Wei, and Wei Zhou. Characteristics of inconel powders for powder-bed additive manufacturing. *Engineering*, 3:695–700, 10 2017.

[60] Yang Gao, Dongyun Zhang, Ming Cao, Runping Chen, Zhe Feng, Reinhart Poprawe, Johannes Henrich Schleifenbaum, and Stephan Ziegler. Effect of δ phase on high temperature mechanical performances of inconel 718 fabricated with slm process. *Materials Science and Engineering: A*, 767:138327, 2019.

[61] D. Texier, Damien Texier, J. Cormier, P. Villechaise, J. Stinville, Chris J. Torbet, S. Pierret, and T. Pollock. Crack initiation sensitivity of wrought direct aged alloy 718 in the very high cycle fatigue regime: the role of non-metallic inclusions. *Materials Science and Engineering A-structural Materials Properties Microstructure and Processing*, 678:122–136, 2016.

[62] Arthur C. Reardon. *Metallurgy for the Non-Metallurgist*. ASM International, 2011.

[63] Saikumar R. Yeratapally, Michael G. Glavicic, Mark Hardy, and Michael D. Sangid. Microstructure based fatigue life prediction framework for polycrystalline nickel-base superalloys with emphasis on the role played by twin boundaries in crack initiation. *Acta Materialia*, 107:152 – 167, 2016.

[64] Influence of thermal post treatments on microstructure and oxidation behavior of eb-pbf manufactured alloy 718. *Materials Characterization*, 150:236 – 251, 2019.

[65] Zhuoer Chen, Xinhua Wu, Dacian Tomus, and Chris H.J. Davies. Surface roughness of selective laser melted ti-6al-4v alloy components. *Additive Manufacturing*, 21:91 – 103, 2018.

[66] Yoichi Yamashita, Takao Murakami, Rei Mihara, Masami Okada, and Yukitaka Murakami. Defect analysis and fatigue design basis for ni-based superalloy 718 manufactured by additive manufacturing. *Procedia Structural Integrity*, 7:11 – 18, 2017. 3rd International Symposium on Fatigue Design and Material Defects, FDMD 2017.

[67] Manatsu OGAWAHARA and Shinya SASAKI. Relationship between internal defect size and fatigue limit in selective laser melted inconel 718. *Mechanical Engineering Journal*, advpub, 2020.

Appendix A

The following images are representative of the surface roughness of each sample group, as measured by laser interferometry.

80 µm, As-built Surface Condition

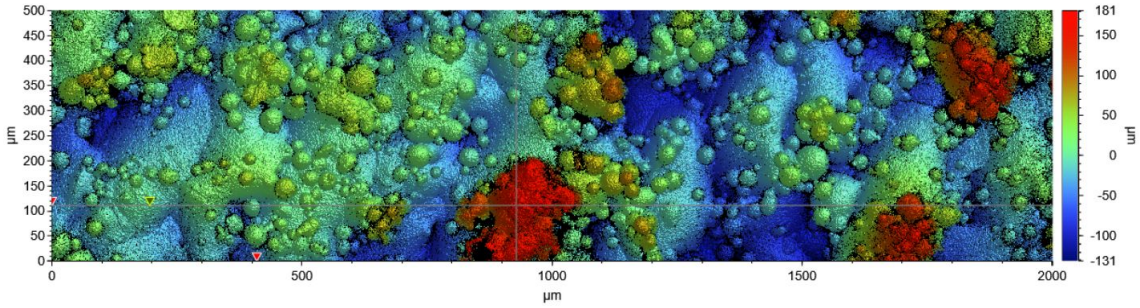

Figure A.1: Inclined build - downskin side, 80 µm layer thickness, as-built surface condition [R_a = 37.9 µm]

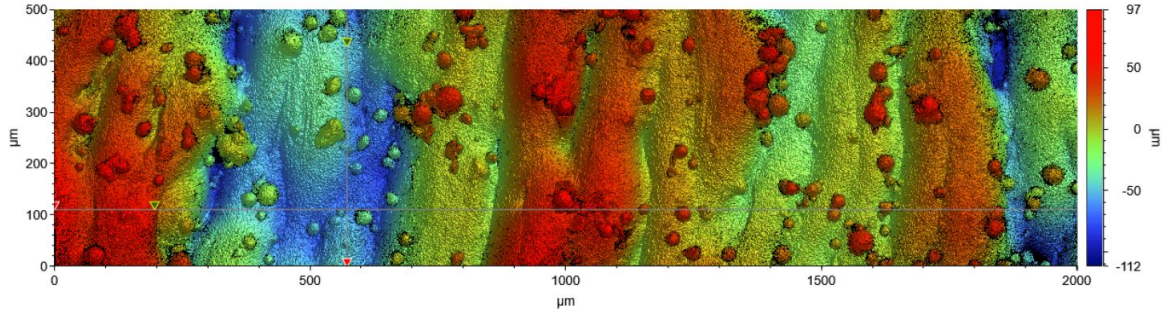

Figure A.2: Inclined build - upskin side, 80 µm layer thickness, as-built surface condition [R_a = 26.7 µm]

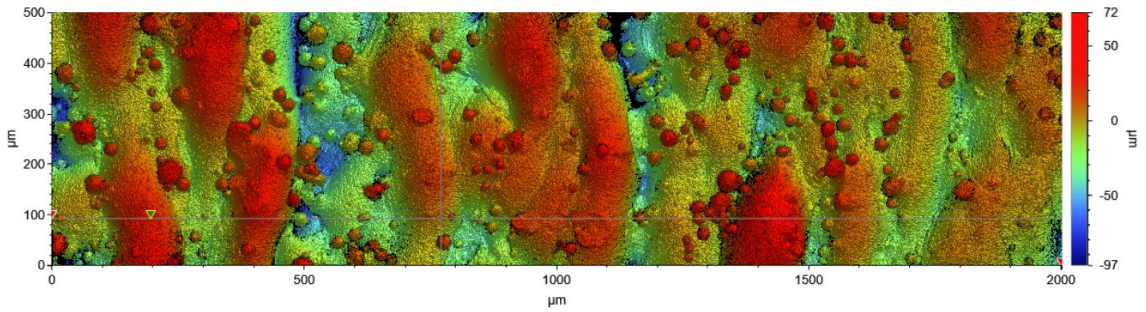

Figure A.3: Vertical build, 80 µm layer thickness, as-built surface condition [R_a = 14.2 µm]

80 µm, Electropolished Surface Condition

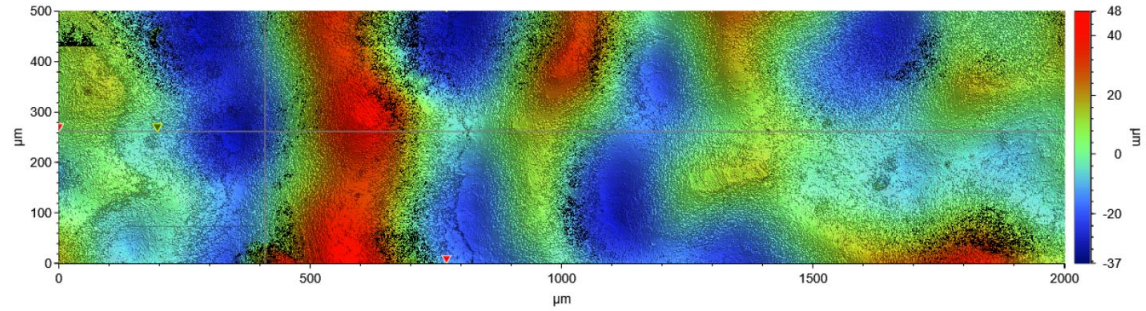

Figure A.4: Inclined build - downskin side, 80 µm layer thickness, electropolished surface condition [R_a = 12.5 µm]

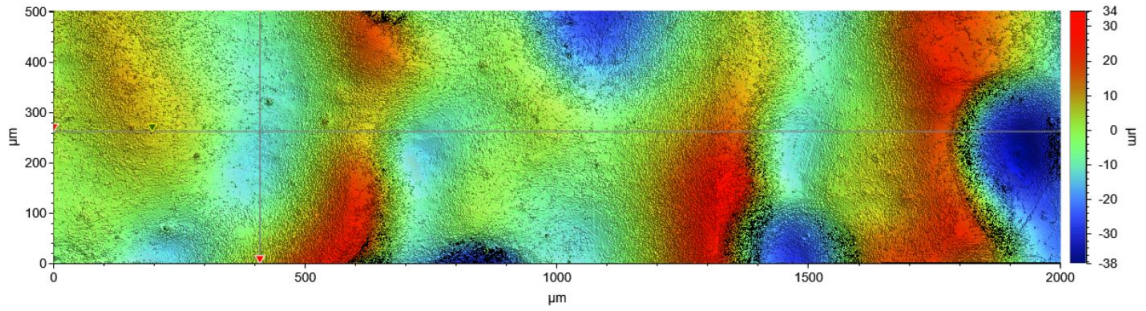

Figure A.5: Inclined build - upskin side, 80 µm layer thickness, electropolished surface condition [R_a = 9.1 µm]

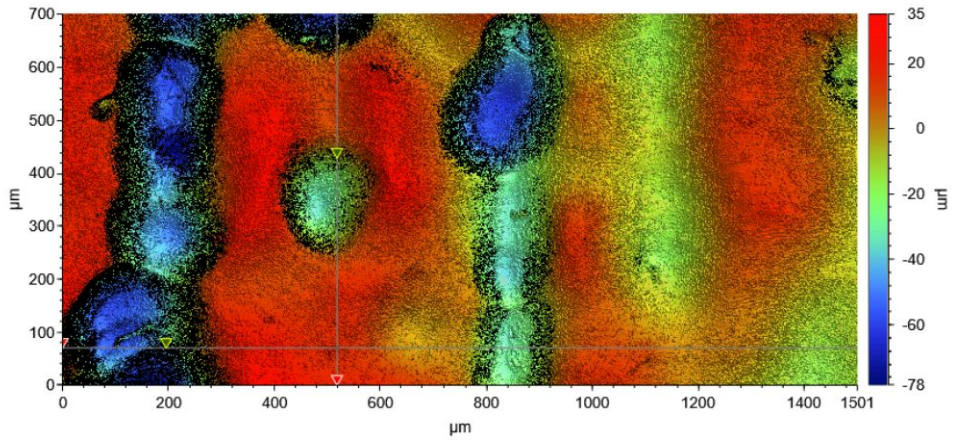

Figure A.6: Vertical build, 80 µm layer thickness, electropolished surface condition [R_a = 15.0 µm]

80 µm, Mechanically Polished Surface Condition

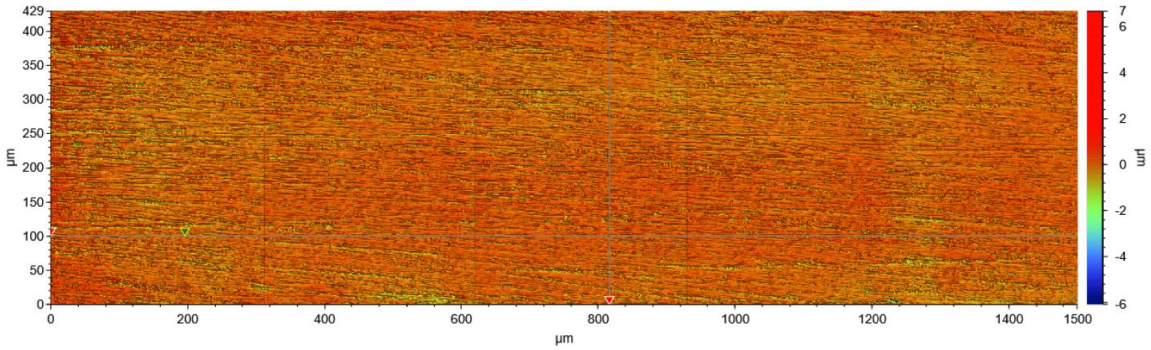

Figure A.7: Inclined build, 80 µm layer thickness, mechanically polished surface condition [R_a = 0.23 µm]

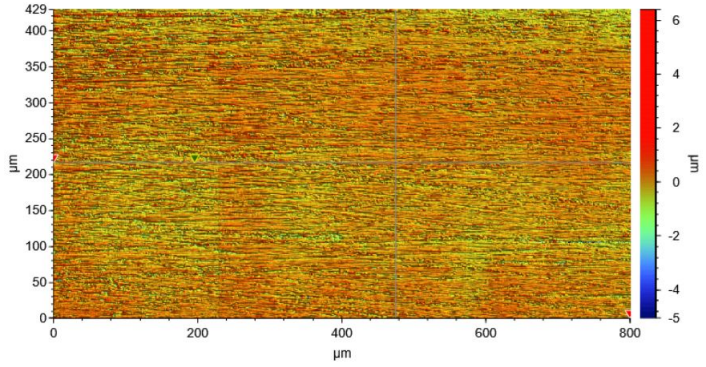

Figure A.8: Vertical build, 80 µm layer thickness, mechanically polished surface condition [R_a = 0.26 µm]

40 µm, As-built Surface Condition

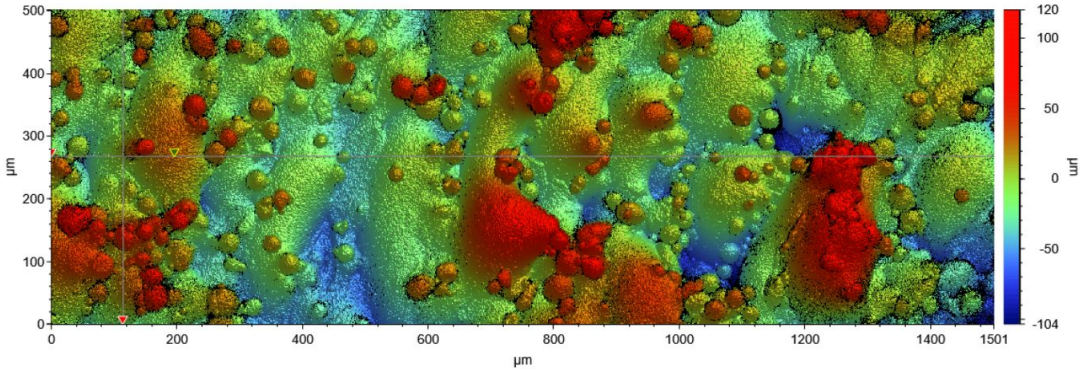

Figure A.9: Inclined build - downskin side, 40 µm layer thickness, as-built surface condition [R_a = 21.8 µm]

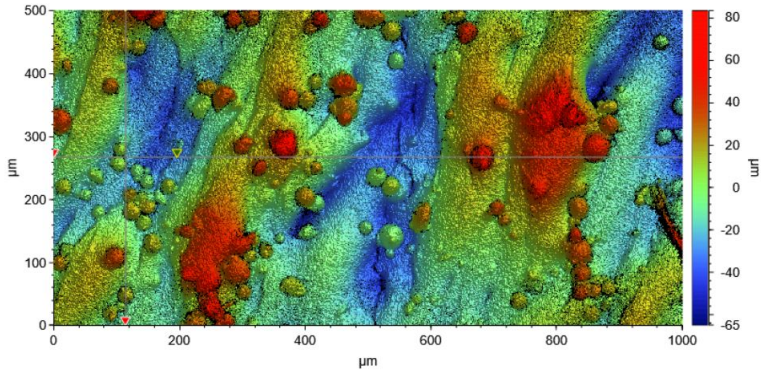

Figure A.10: Inclined build - upskin side, 40 µm layer thickness, as-built surface condition [R_a = 18.1 µm]

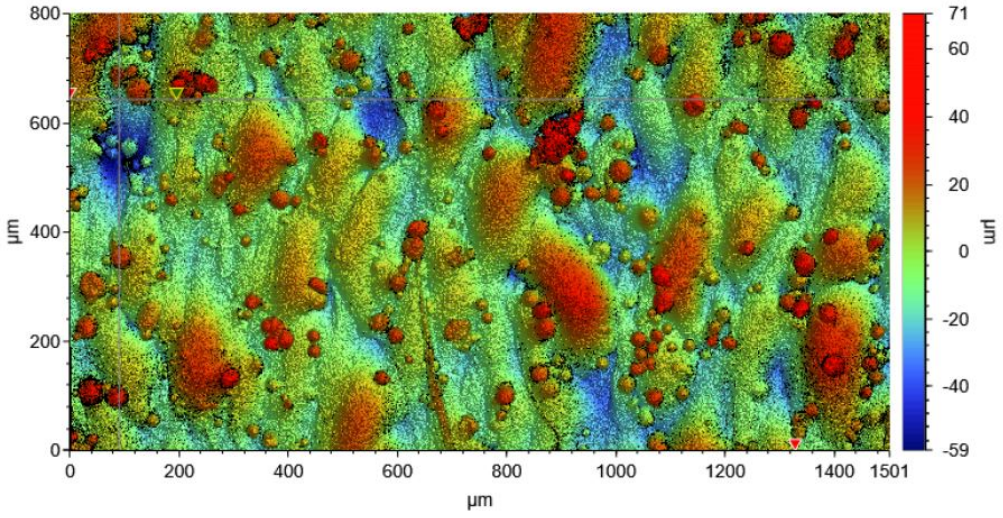

Figure A.11: Vertical build, 40 µm layer thickness, as-built surface condition [R_a = 11.4 µm]

40 µm, Electropolished Surface Condition

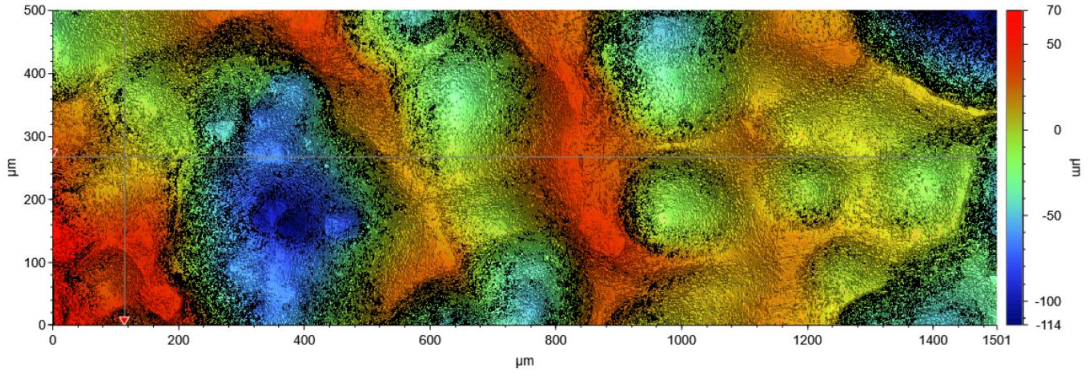

Figure A.12: Inclined build - downskin side, 40 µm layer thickness, electropolished surface condition [R_a = 23.3 µm]

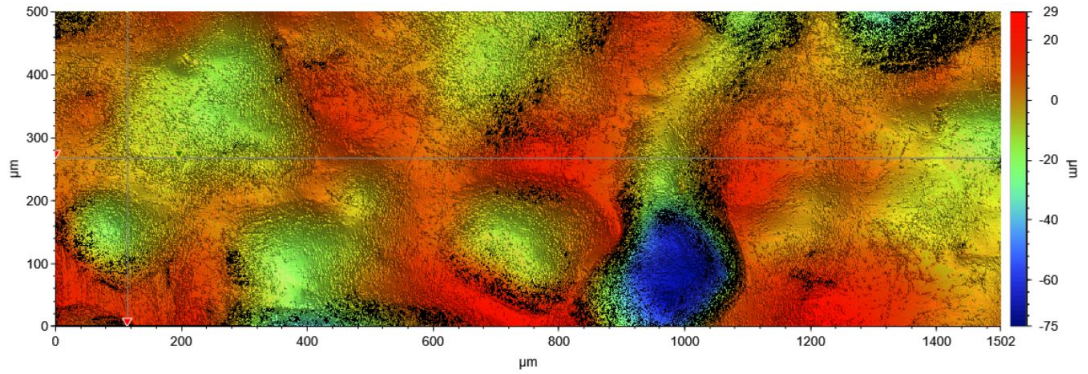

Figure A.13: Inclined build - upskin side, 40 µm layer thickness, electropolished surface condition [R_a = 9.0 µm]

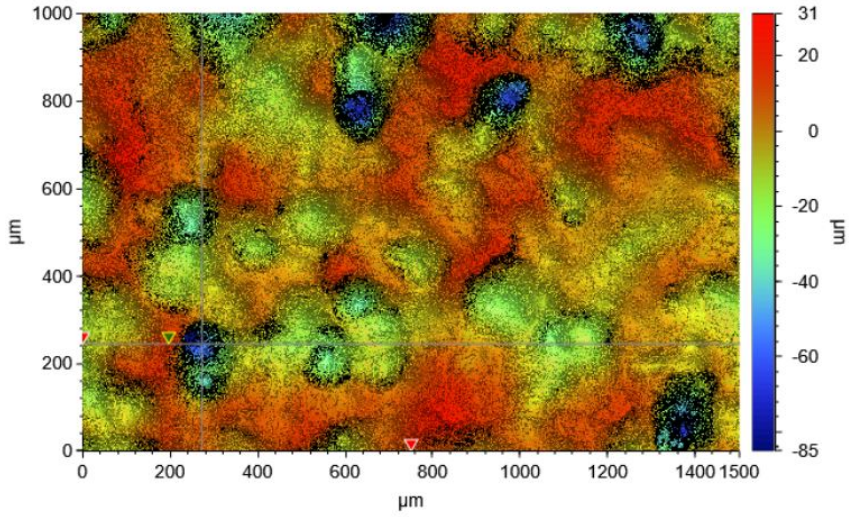

Figure A.14: Vertical build, 40 µm layer thickness, electropolished surface condition [R_a = 8.4 µm]

40 µm, Mechanically Polished Surface Condition

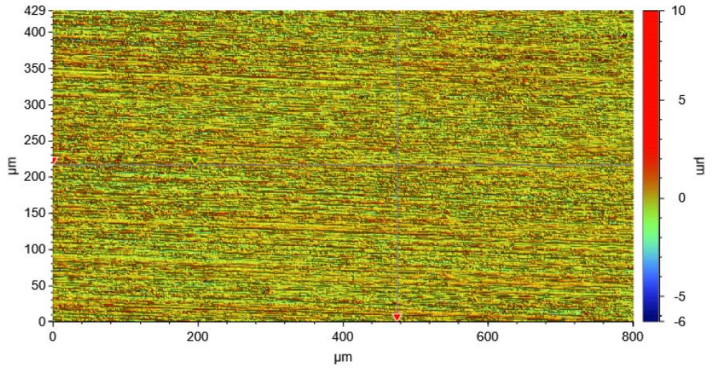

Figure A.15: Inclined build, 40 µm layer thickness, mechanically polished surface condition [R_a = 0.36 µm]

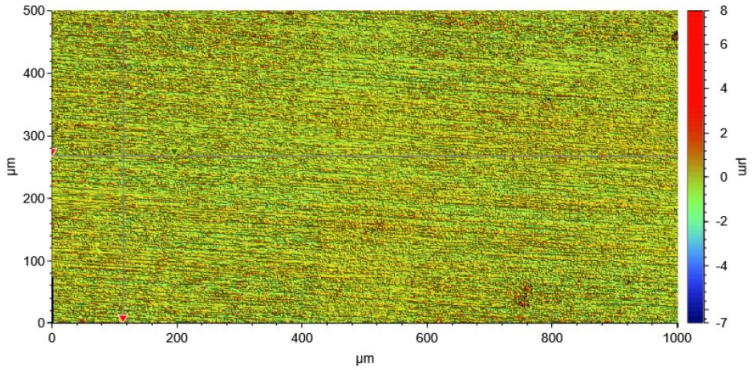

Figure A.16: Vertical build, 40 µm layer thickness, mechanically polished surface condition [R_a = 0.39 µm]

B

Appendix B

```
% K. Heyson
%
% Determination of surface roughness Ra
% Input:
%       .csv line data
% Output:
%       Ra value
%       Plot of line profile and average


function[Ra,U,avg] = roughness_a_abs()
T = readtable('H2V_200x_2.csv');        % input line data
U = table2array(T);
n = length(U(:,1));
avg = mean(U(:,1));             % find average
y = zeros(n,1);
normal = zeros(n,1);
for j = 1:n
    normal(j) = U(j,1) - avg;       % adjust line y values in relation to average
    y(j) = abs(normal(j));
end
sum = 0;
for i = 1:n
    sum = y(i,1) + sum;
end
Ra = sum/n;
hold on
plot(U)
hline = refline([0 avg]);
hline.Color = 'r';
hold off
end
```

C

Appendix C

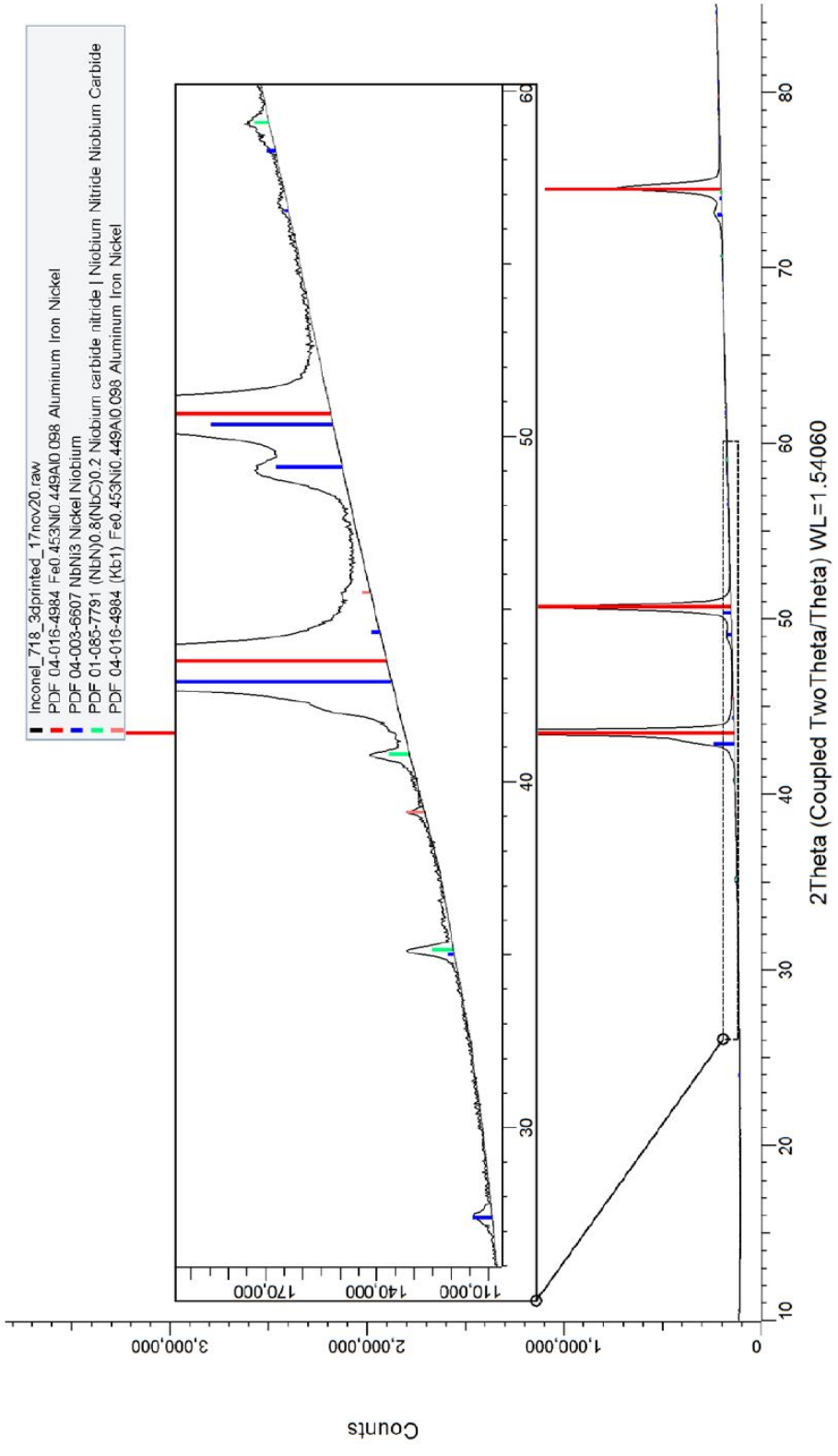

Figure C.1: XRD pattern of the printed (40 µm, inclined, electropolished) sample with matching phases

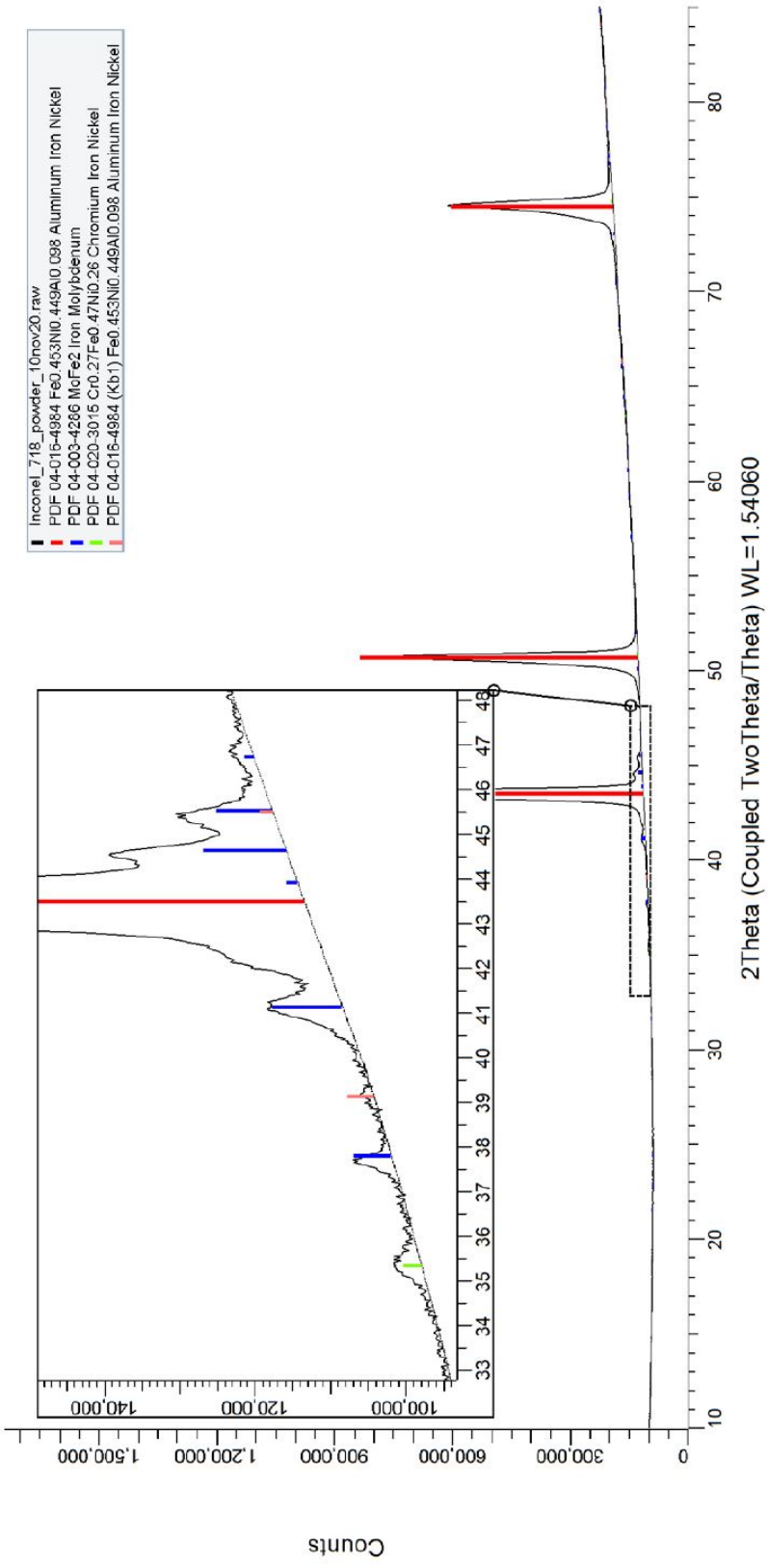

Figure C.2: XRD pattern of the feedstock powder with matching phases